

ESD-TR-66-446
ESTI FILE COPY

ESD-TR-66-446

ESD RECORD COPY

RETURN TO
SCIENTIFIC & TECHNICAL INFORMATION DIVISION
(ESTI), BUILDING 1211

ESD ACCESSION LIST

ESTI Call No. AL 54435

Copy No. 1 of 3 cys.

1

Radio Physics
and
Astronomy

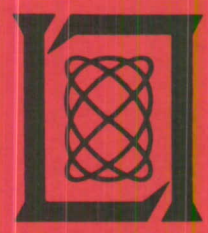
1966

Prepared under Electronic Systems Division Contract AF 19 (628)-5167 by

Lincoln Laboratory

MASSACHUSETTS INSTITUTE OF TECHNOLOGY

Lexington, Massachusetts



ESV2

AD0645324

The work reported in this document was performed at Lincoln Laboratory, a center for research operated by Massachusetts Institute of Technology, with the support of the U.S. Air Force under Contract AF 19(628)-5167.

This report may be reproduced to satisfy needs of U.S. Government agencies.

Distribution of this document is unlimited.

Non-Lincoln Recipients

PLEASE DO NOT RETURN

Permission is given to destroy this document
when it is no longer needed.

1

Radio Physics
and
Astronomy

1966

Issued 19 December 1966

Lincoln Laboratory

MASSACHUSETTS INSTITUTE OF TECHNOLOGY

Lexington, Massachusetts



ABSTRACT

This report covers research in the fields of radio physics and astronomy at Lincoln Laboratory for the period from 1 December 1965 through 31 May 1966. In a few cases, material from earlier work is introduced to clarify the discussion of a current program, e.g., "Experimental Evaluation of a 1000-Wavelength Antenna." Twenty-three papers presenting work by the Radio Physics, Communications, Solid State and Radar Divisions of Lincoln Laboratory and by the M.I.T. Research Laboratory of Electronics with the cooperation of Lincoln Laboratory are included. Twenty of the papers discuss work involving the Millstone Hill Field Station which is the Laboratory's primary facility for experimental research in radio physics and astronomy. Two papers describe the 28-ft millimeter research facility (1000 wavelength) at Lincoln Laboratory in Lexington and one is a theoretical paper on scattering from objects with irregular surfaces.

Accepted for the Air Force
Franklin C. Hudson
Chief, Lincoln Laboratory Office

CONTENTS

Abstract	iii
Reports	vii
Foreword	ix
 I. SUMMARY	 1
A. Introduction	1
B. Radar Astronomy	1
C. Radio Astronomy	1
D. Atmospheric Research	2
E. Space Surveillance Techniques	2
F. Systems Development	2
 II. RADAR ASTRONOMY	 3
A. Introduction	3
B. Lunar Studies	3
C. Planetary Studies	14
References	19
 III. RADIO ASTRONOMY	 21
A. Digital Mapping Procedure Applied to Galactic Center	21
B. Real-Time Program for Spectral Line Measurements at Haystack	23
C. Stokes Parameters for 1665-MHz OH Emission Near W3	28
D. Absolute Flux Measurements of Cassiopeia A and Taurus A at 3.64 and 1.94 cm	35
E. Secular Variations in Centimeter Radio Flux from 3C273	37
F. Observations of Hydrogen Recombination Lines	39
G. Haystack-Millstone Interferometer	40
H. Spectrum Measurements Near 1-cm Wavelength Using the 28-ft Millimeter-Wave Antenna	42
References	48

Contents

IV.	ATMOSPHERIC RESEARCH	49
	A. Incoherent Ionosphere Backscatter	49
	B. Lower Atmospheric Studies at X-Band	49
	C. Auroral Observations	64
	References	70
V.	SPACE SURVEILLANCE TECHNIQUES	71
	A. Millstone Radar	71
	B. Haystack X-Band Passive Autotracker	72
	C. Ruby Laser Radar	72
VI.	SYSTEMS DEVELOPMENT	77
	A. Equipment Development for Fourth Test of General Relativity	77
	B. The Millimeter-Wave Facility at Lexington	79
	References	81
	APPENDIX A – Experimental Evaluation of 1000-Wavelength Antenna	83
	APPENDIX B – Extension of Boundary Perturbation Theory	101

REPORTS BY MEMBERS OF THE MILLSTONE HILL FIELD STATION STAFF

December 1965 through 21 May 1966

PUBLISHED

Journal Articles and Meeting Speeches*

JA No.

2541A	Radar Observations of Meteor Deceleration	J. V. Evans	J. Geophys. Res. <u>71</u> , 171 (1966), DDC 630368
2593	Relationship of Geometric Optics and Autocorrelation Approaches to the Analysis of Lunar and Planetary Radar	T. Hagfors	J. Geophys. Res. <u>71</u> , 379 (1966), DDC 633184
2627	Tenuous Surface Layer on the Moon: Evidence Derived from Radar Observations	T. Hagfors R. A. Brockelman H. H. Danforth L. B. Hanson G. M. Hyde	Science <u>150</u> , 1153 (1965), DDC 628565
2699	Radio Structure of the Galactic Center Region	D. Downes [†] A. Maxwell [†] M. L. Meeks	Nature <u>208</u> , 1189 (1965), DDC 635327

MS No.

1354	Radar Studies of the Moon	J. V. Evans	NBS J. Research (Radio Sci.) <u>69D</u> , 1637 (1965)
------	---------------------------	-------------	----------------------------------------------------------

* * * * *

UNPUBLISHED

Journal Article

JA No.

2721	Note on the Effect of Shadowing on the Backscattering of Waves from a Random Rough Surface	R. A. Brockelman T. Hagfors	Accepted by IEEE Trans. Antennas Propag.
------	--------------------------------------------------------------------------------------------	--------------------------------	---------------------------------------------

* Reprints available.

† Author not at Lincoln Laboratory.

Reports

		<u>Meeting Speeches*</u>	
MS No.			
1537A,B	Radar Observations of the Moon	T. Hagfors	Seminar, University of Florida, 2 December 1965; Seminar, University of California, 15 December 1965
1600	Surface Properties of the Moon as Deduced by Radar	G. H. Pettengill	NASA Science and Technology Advisory Committee for Manned Space Flight, Cape Kennedy, Florida, 18 February 1966
1604	Incoherent Scattering from the Ionosphere	J. V. Evans	Seminar, M.I.T., 18 March 1966
1624	A Digital Mapping Procedure Applied to the Galactic Center	M. L. Meeks J. C. Henry	URSI, Washington, D. C., 18-21 April 1966
1671	Radar Observations of Venus at 3.8 and 23 cm Wavelength	J. V. Evans R. P. Ingalls	
1648	The Polarization Parameters for the 1665-Mc/s OH Emission from W3	M. L. Meeks J. A. Ball J. C. Carter	American Astronomical Society, Langley Research Center, Hampton, Virginia, 28-31 March 1966
1680	Recent Radar Results on the Rotation and Surface Features of the Inner Planets	G. H. Pettengill	Colloquium, Goddard Space Flight Center, Greenbelt, Maryland, 27 May 1966

*Titles of Meeting Speeches are listed for information only. No copies are available for distribution.

FOREWORD

This report is the second in a series on research in the field of radio physics and astronomy being carried out at Lincoln Laboratory. It covers activities for a period of approximately six months. Our objective for this series is to provide a medium for the presentation of scientific results, technical and engineering developments, studies, and background reviews; in part, this report serves as an observatory report for the Millstone Hill Field Station. For reasons of expedience in getting the series started, the first report contained only descriptions of programs being carried out by the Radio Physics Division at the Millstone Hill Field Station. It was intended, however, that these reports also include allied work performed by other Lincoln Laboratory divisions as well as similar work by M.I.T. personnel using Lincoln Laboratory's facilities. In that respect the present report, which contains substantial contributions from other Lincoln Laboratory divisions and the Research Laboratory of Electronics, meets these original objectives. However, the Millstone Hill Field Station is the Laboratory's primary research facility in the radio physics and astronomy fields and for this reason descriptions of its programs still account for the major portion of this report.

I. SUMMARY

A. INTRODUCTION

Following the precedent set by our first Radio Physics and Astronomy Report, the material in the present report is organized under four areas of research: Radar Astronomy, Radio Astronomy, Atmospheric Research and Space Surveillance Techniques. A fifth section, Systems Development, has been added. Two papers which do not clearly fall in any of the above classifications are included as appendices. One of these papers gives a detailed description of evaluation tests performed several years ago on the 1000-wavelength (28-ft diameter) antenna at Lincoln Laboratory. The other paper presents an extension of perturbation theory for examination of the scattering characteristics of irregularly shaped objects.

B. RADAR ASTRONOMY

The 23.2-cm Millstone radar and the 3.8-cm Haystack radar continued to be employed in lunar* and planetary studies. In the lunar experiments the scattering laws at the two wavelengths were determined and studies of the polarizing properties of the lunar surface were made at 23.2 cm.

The planetary radar studies consisted mainly of observations on the planet Venus. Measurements were made of range, cross section and the spectrum of the reflected signals which yielded information regarding the orbit and the scattering laws at the two wavelengths.

C. RADIO ASTRONOMY

Radio astronomy continued to be one of our most fruitful areas of research. Interesting observations were made of anomalous spectral line emissions from OH at 1665 MHz near W3. Absolute flux measurements of Cassiopeia A and Taurus A were made at 3.64 and 1.94 cm. The results of these flux measurements enable the use of these sources for measuring the gains of large antennas. Observations at these two wavelengths were also made of the secular variations in the radio flux from 3C273. A digital mapping technique developed by personnel of Lincoln Laboratory and M.I.T. Research Laboratory of Electronics was used to map the center of our galaxy.

The Haystack 120-foot antenna is the basic instrument for most of our radio astronomy programs at wavelengths from hydrogen line to about 1.5 cm. However, the 84-foot antenna at Millstone has been used with the Haystack antenna to form a 2000-foot base-line radiometric interferometer. First use of the interferometer will be to determine the positions and angular sizes of OH emission regions in the 1665-MHz band.

The 28-foot millimeter-wave antenna at Lincoln Laboratory in Lexington was used in radiometric studies of Venus, Jupiter, the moon and the terrestrial atmosphere at wavelengths near one centimeter.

* The lunar studies program is supported by NASA.

Section I

D. ATMOSPHERIC RESEARCH

Studies of the ionosphere by the incoherent backscatter technique continue to be an important area of research. However, because of the lag between data gathering operations and the data reduction and analysis operations, there is little to report in this area that was not discussed in Radio Physics and Astronomy Report (1965:1).

No new data were taken in the auroral studies program during the period covered by this report. All the effort in this area was devoted to the reduction and analysis of auroral data taken earlier.

Because of the increased use of X-band wavelengths in satellite communication systems, there is great interest in obtaining a better understanding of the effects of precipitation on radio propagation at these wavelengths. The Haystack X-band radiometer has been used by the Lincoln Laboratory Communications Division in conjunction with the M.I.T. weather radar research facility to examine the relation between radar reflectivity and thermal effects for a number of showers observed in August 1965.

E. SPACE SURVEILLANCE TECHNIQUES

The space surveillance program for the Millstone L-band radar was discussed in detail in the last radio physics and astronomy report (1965:1). The most important part of this program is the development of improved techniques for the detection and tracking of distant satellites. A versatile system of radar data handling and orbit computation programs is being developed, partially through contractual assistance, for the Millstone computer. Two new approaches have also been studied relative to extending the range of the radar by computer integration techniques while retaining the ability to autotrack.

A new tracking experiment using a ruby laser radar is being conducted at the Millstone Hill Field Station by the Optics and Infrared Group of Lincoln Laboratory's Solid State Division. This instrument uses a precision azimuth-elevation mount installed on a concrete silo adjacent to the Millstone radar. The mount is slaved to the Millstone L-band radar, which is used to bring the laser radar beam on target.

Another interesting development at the Millstone Hill Field Station is the experimental use of the Haystack 120-ft dish for closed-loop passive tracking of cooperative X-band satellites. The precision angle tracking provided by this facility can be used to upgrade the orbital elements of satellites in very high orbits, e.g., certain communications satellites, which are beyond the range of conventional "skin-tracking" satellite radars.

F. SYSTEMS DEVELOPMENT

A great effort is being made to complete a 500-kw average power X-band radar for Haystack. This radar will be used initially in the "fourth test of general relativity" which was proposed by I.I. Shapiro and described in the last radio physics and astronomy report.

A millimeter-wave research facility is being developed around the 28-ft precision surface antenna at Lincoln Laboratory. This facility, when developed according to present plans, will include a CW 1000-W, 35-GHz radar.

II. RADAR ASTRONOMY

A. INTRODUCTION

Observations of the moon were made as part of a program sponsored by NASA. An extensive series of observations at Millstone forms the basis of a paper (in press¹). This work consisted primarily of determining the angular scattering law at 23-cm wavelength and comparing this with determinations at other wavelengths (e.g., the 68-cm results reported by Evans and Pettengill²). Preliminary results of new experiments in which the depolarizing properties of the lunar surface were studied in greater detail than hitherto are reported here. Measurements with the Haystack radar at 3.8 cm have also recently begun. A considerable amount of effort has been devoted to the programming required for the lunar mapping that we plan to carry out at Haystack Hill. The scattering law at 3.8 cm has also been redetermined using Haystack and is found to be in good agreement with the earlier 3.6-cm determination reported by Evans and Pettengill.

The Millstone radar was employed to observe Venus during the past year, primarily in order to secure precise range information on a portion of the orbit not previously observed by radar. Range determinations were made for a period of six months centered on close approach. During the central four months, the flight time was measured to an accuracy of approximately $\pm 10 \mu\text{sec}$ about twice a week. These measurements also form the subject of a separate report.

Perhaps the most exciting event during the past year for the radar astronomers at the Field Station was the availability, for the first time, of a 100-kw, X-band CW radar system at Haystack Hill. A few observations of Mercury have been made with this radar, but most of the effort so far has been devoted to studying Venus. A particularly intensive series of observations was made during the January 1966 inferior conjunction. Since these measurements will be reported separately in a journal article, we only summarize the main conclusions here.

B. LUNAR STUDIES

1. Polarization of Radar Returns from Moon

a. Introduction

Systematic studies of the state of polarization of radar echoes from the lunar surface for different types of polarization of the transmitted wave provide information which, when properly interpreted, relates directly to the structure of the lunar surface. Depolarization experiments have been carried out at $\lambda = 23 \text{ cm}$ with the Millstone radar and have been started at $\lambda = 3.8 \text{ cm}$ using the Haystack radar. Section II-B-1-b briefly describes the equipment which provides the necessary flexibility for such polarization experiments. Sections II-B-1-c and d describe the experiments and give the results. Section II-B-1-e discusses their physical significance.

b. Polarization Equipment

Two circularly polarized waves of opposite sense can be excited in the Millstone antenna by feeding a signal into either one or the other of two antenna input terminals. By providing a

Section II

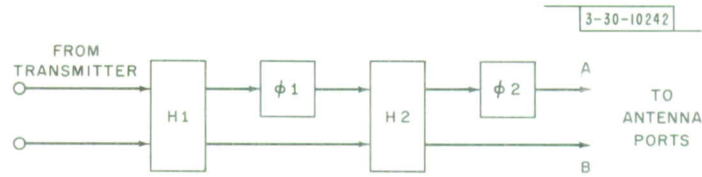


Fig. II-1. Circuit to control transmitter polarization.

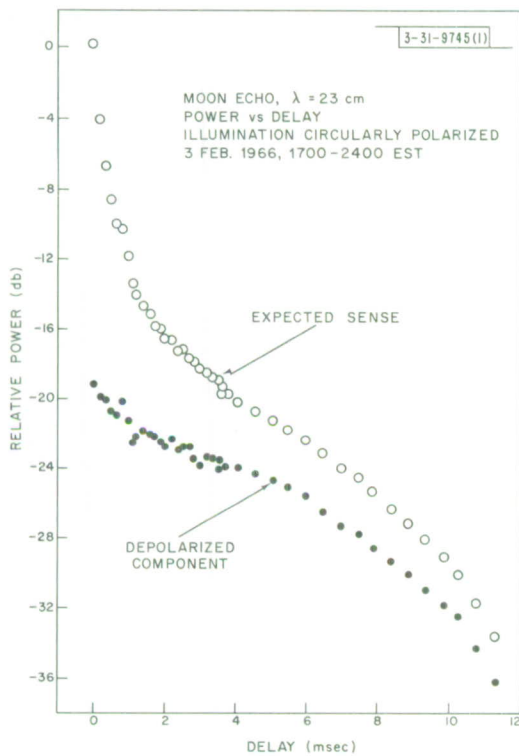


Fig. II-2. Polarized and depolarized circular components vs delay.

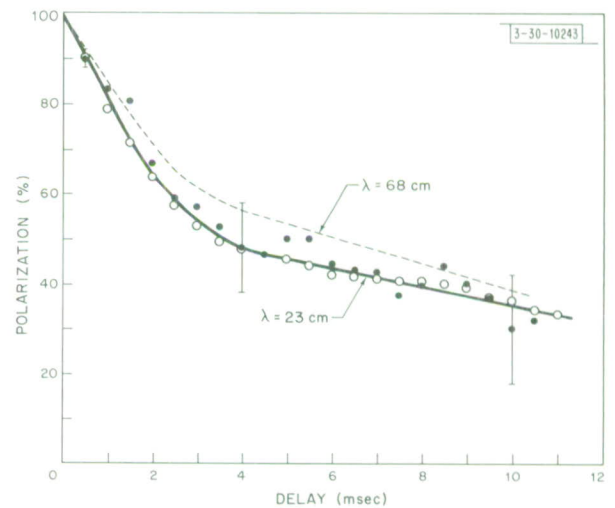


Fig. II-3. Percentage circular polarization vs delay.

network which can arbitrarily divide the power between the two antenna ports and alter their relative phase, it is possible to excite a wave of arbitrary polarization. As shown in Fig. II-1, the signal from the transmitter is applied to the 90° 3-db hybrid H1. In one of the two signal paths of the output of H1, a variable phase changer ϕ_1 is inserted. The two signals are then applied to another hybrid circuit H2. The relative power at the output terminals A and B can thus be varied by changing the phase delay in ϕ_1 and the relative phase of the two signals applied to the antenna terminals by changing the phase delay in ϕ_2 . This combination network allows an arbitrary polarization to be transmitted.

The combination of the two orthogonally polarized received signals at the two input terminals of H1 in a second network similar to that shown in Fig. II-1 allows for the reception of a specified pair of orthogonally polarized components for any arbitrary transmitted polarization. The synthesis of any arbitrary polarizations for the received components could, in principle, be carried out in the computer since quadrature phase detection is employed and detector outputs are digitized for both polarizations. This procedure was not followed, however, because of inadequate phase and gain stability in the receiver chains.

The Haystack system operating at 3.8 cm is at present capable only of transmitting circularly polarized waves. A waveguide network similar to that shown in Fig. II-1 is, however, available for the reception of an arbitrary pair of orthogonally polarized waves.

c. Experiments and Results at 23 cm at Millstone

The moon was illuminated with circularly polarized waves and the two opposite sense circularly polarized received waves were observed. The ellipticity of the transmitted wave was adjusted by means of a near-field test antenna to give a ratio between major and minor axes of less than 0.4 db. The ellipticity of the two receiver channels was typically 0.6–0.8 db and a correction was applied in the data analysis program to account for this. Figure II-2 shows a plot of both polarized and depolarized components as a function of delay beyond the subradar point. Range resolution was $100\mu\text{sec}$ to a delay of 4 msec and $500\mu\text{sec}$ for the remainder of the curve. Figure II-3 shows the percentage polarization measured as a function of delay and compares the results with previous observations at 68 cm (Ref. 2). The polarization is defined by

$$p = \frac{P_R - P_L}{P_R + P_L}$$

where P_R , P_L are the powers in the right and left circularly polarized receiver channels, respectively.

A second experiment consisted in illuminating the moon with linearly polarized radiation and measuring the ratio of the polarized to the depolarized components of the received signal. Because of uncertainty in the amount of Faraday rotation, the receiver polarization was rotated between runs. The relative power output of the two receiver channels will then vary sinusoidally with the angle 2Ω , where Ω is the feed rotation angle. A least-mean-square sine wave was fitted to the data obtained in different runs and the depth of modulation was used to determine the ratio of the depolarized to the polarized components. Figure II-4 shows the two components plotted as a function of delay. The spike in the depolarized component near zero delay

Section II

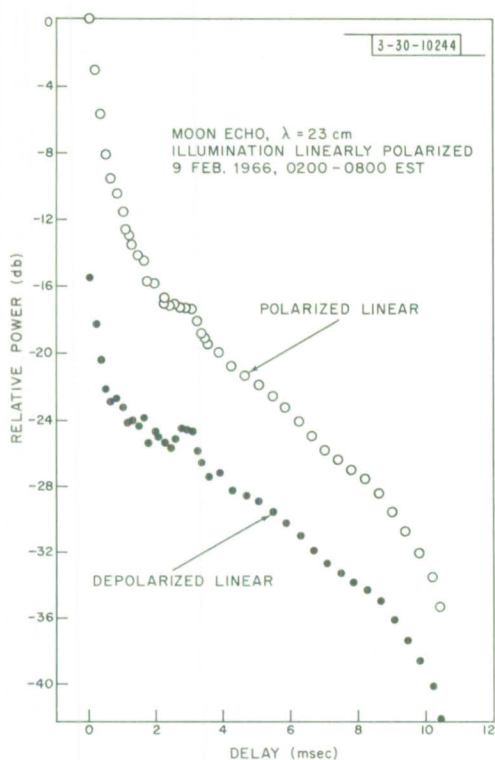


Fig. II-4. Polarized and depolarized linear components vs delay.

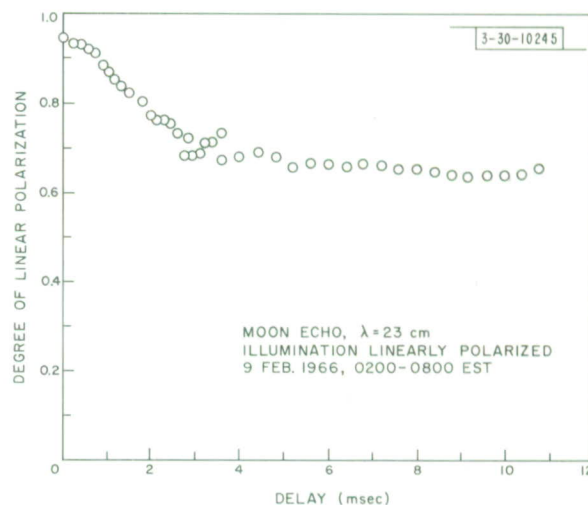


Fig. II-5. Degree of linear polarization vs delay.

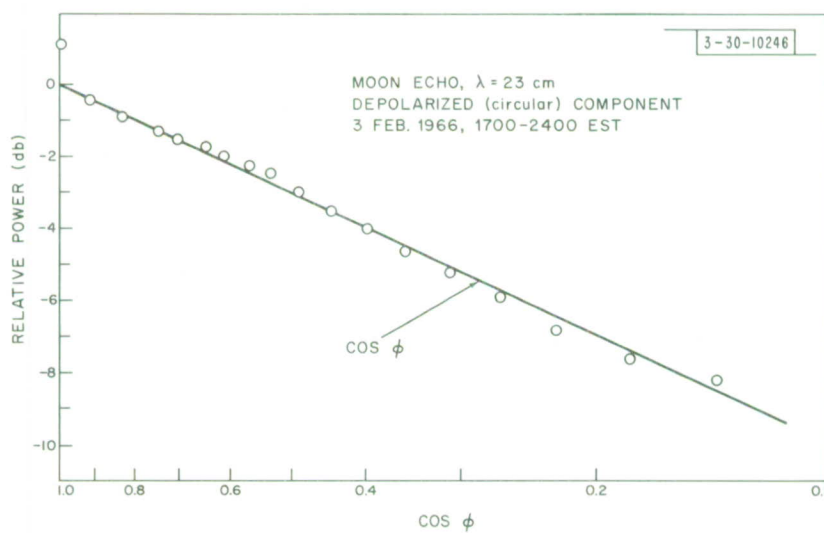


Fig. II-6. Angular scattering law for depolarized circular component.

is at present believed to be caused by insufficient isolation between the two channels. The degree of linear polarization plotted as a function of delay is shown in Fig. II-5. The definition of polarization is similar to that in the case of circular polarization, except that $P_R P_L$ have to be replaced by the power in the two linearly polarized orthogonal channels. Note that the linear depolarization is much smaller than the circular depolarization.

At least one peculiarity of the data just described is worth mentioning. When the depolarized circular component in Fig. II-2 — after appropriate correction for antenna polar diagram effects — is plotted as a function of $\cos \Theta$, where Θ is the angle of incidence, the power-range relationship very closely follows a $\cos \Theta$ law, as shown in Fig. II-6. This corresponds to a uniformly bright disk. When the depolarized linear component in Fig. II-4 after similar corrections is plotted in the same way, it turns out that the scattering law goes as $\cos^{3/2} \Theta$, as shown in Fig. II-7.

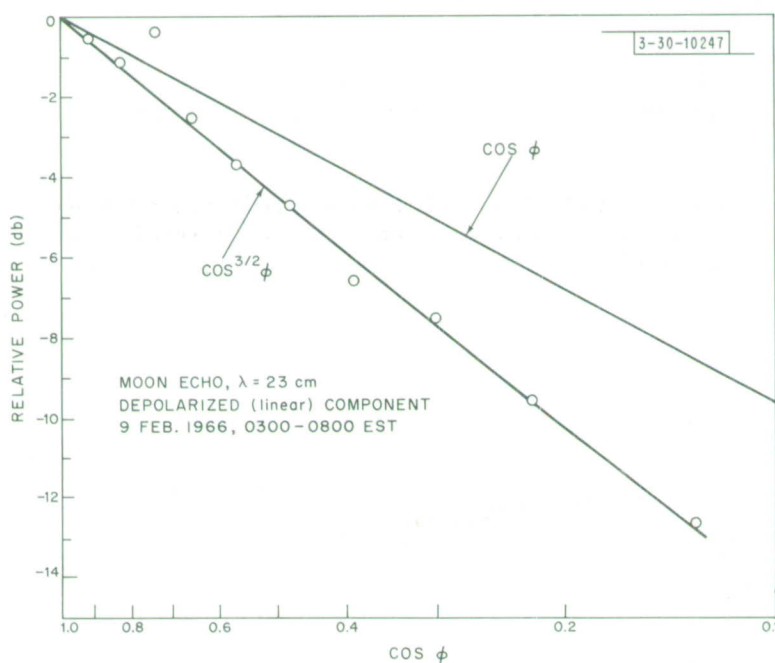


Fig. II-7. Angular scattering law for depolarized linear components.

In the second of the two experiments just described, the transmitted linear polarization will lie within the local plane of incidence at two points on a constant delay ring and will be normal to the local plane of incidence at two other points 90° away. At intermediate points on the range ring considered, the direction of polarization of the illumination with respect to the local plane of incidence will be intermediate between 0° and 90° .

In order to examine the effect of the orientation of the transmitted linear polarization with respect to the local plane of incidence, the linear polarization of the transmitter was programmed to be parallel to the instantaneous lunar libration axis. The resulting measured ratio of depolarized-to-polarized components is shown as a function of delay in Fig. II-8, where it is also compared

Section II

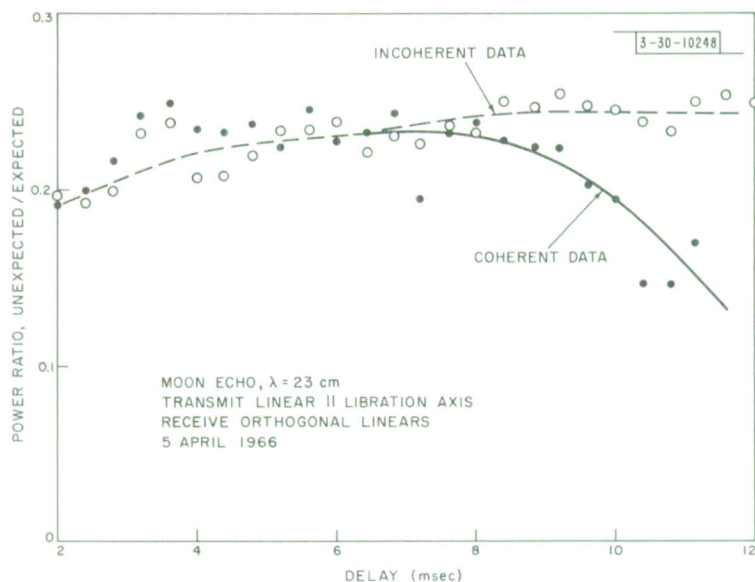


Fig. II-8. Ratio of depolarized-to-polarized components when surface is illuminated with a wave polarized linearly in local plane of incidence.

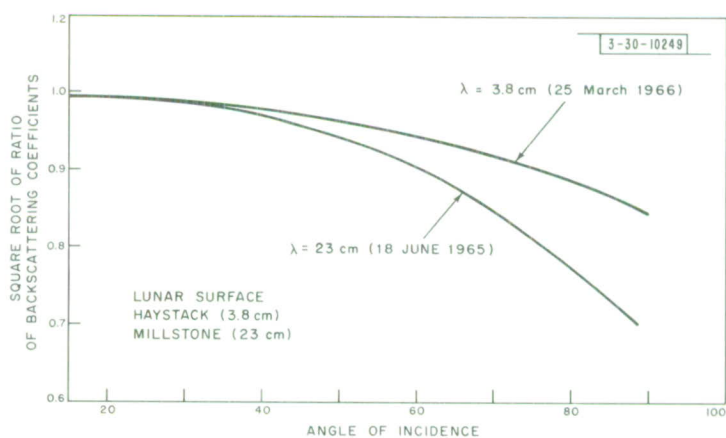


Fig. II-9. Square root of ratio of backscattering coefficients plotted against angle of incidence for $\lambda = 23$ and 3.7 cm.

with the ratio for a complete range ring (obtained from incoherent processing of the data). As explained in the next section, the data shown in Fig. II-8 may be in qualitative agreement only with previous work and the measurements will be repeated to reduce noise and, if possible, to eliminate any systematic errors in the experiment.

d. Results Obtained at Haystack at 3.8 cm

The measurement of the difference of backscattering coefficients for waves polarized in and across the local plane of incidence previously carried out at 23 cm (Ref. 3) was repeated at 3.8 cm, using a slightly different technique. Whereas the original 23-cm experiment used frequency resolution to separate small areas with a well-defined plane of incidence, the 3.8-cm experiment depended on the narrow polar diagram of the antenna beam for this purpose. As before, the antenna was made to transmit a circularly polarized wave. Two orthogonal linearly polarized channels were synthesized in a manner similar to that shown in Fig. II-1. One channel was aligned for maximum sensitivity to correspond with E-field parallel to the disk-radial direction connecting the center of the disk and the point of observation. The variation of the power ratio in the two received components with angle of incidence was derived by moving the antenna beam radially from the center of the disk to the limb with a fixed polarization of the two receiver channels. Figure II-9 shows the square root of the ratio of the two received components as a function of angle of incidence. Also shown is the corresponding curve obtained previously at 23-cm wavelength.³ As can be seen, the polarization effect is significantly smaller at X-band than at L-band.

e. Discussion

The depolarization of the circularly polarized wave may be explained in at least two ways: (1) a difference in the backscattering coefficients of the two principal linearly polarized components but no coupling from one into the other, or (2) a "spillover" from one of the principal linear components into the other. Table II-1 shows a few numerical values for hypothesis (1).

TABLE II-1 PREDICTIONS FOR HYPOTHESIS (1)	
If Ratio of Circular Returns for Circular Illumination Is (in db):	Ratio of Backscattering Coefficients for Linear Components Should Be (in db):
2.0	18.8
4.0	13.0
6.0	9.6
8.0	7.3
10.0	5.6

Section II

Since the ratio of the two orthogonal backscattering coefficients for linear polarization has previously been shown to be, at most, about 3.0 db (Ref. 3), we see that hypothesis (1) is completely inadequate to account for the observed depolarization effect, which, for circular transmitted and circular received waves, corresponds to a ratio of the two components of only between 2 and 3 db (compare Fig. II-2).

Hypothesis (2) appears to be much closer to the actual situation than (1) in accounting for the circular-circular depolarization effect and it may also largely explain the observed linear-linear depolarization effect. One might imagine that the scattering at oblique incidence occurs from a discrete structure of irregular shape, forcing the induced currents to flow in directions which differ from that of the impressed electric field. As a mathematical model, one might imagine the scattering to occur from a collection of randomly oriented dipoles and a collection of nondepolarizing ideal reflectors.⁴ On the basis of such a naive model, one can work out the ratio of total scattered power in the dipole component and the ideally reflected component for various ratios of depolarized-to-polarized components for circular and for linear illumination. A set of predictions based on this dipole-reflector model is given in Table II-2. Toward grazing angles of incidence on the surface, it appears that a percentage of power from the randomly oriented dipoles of about 70 percent will explain both linear and circular polarization. This simple model does not explain completely the variation of depolarization with angle of incidence because the linear/linear depolarization remains virtually constant for angles of incidence $45^\circ < \varphi < 90^\circ$, whereas the circular/circular depolarization increases significantly in this range of angles.

The results shown in Fig. II-8 can be understood at least qualitatively on the basis of previous experiments as follows. Denote the backscattering coefficients for in- and across-plane of incidence polarization by σ_{VV} and σ_{HH} . By reciprocity the "spillover" coefficients σ_{VH} and

TABLE II-2
PREDICTION BASED ON DIPOLE-REFLECTOR MODEL

Function of Power Scattered From Dipoles (%)	Ratio of Depolarized/ Polarized, Linear (linear illumination) (db)	Ratio of Depolarized/ Polarized, Circular (circular illumination) (db)
10	15.9	12.8
20	12.8	9.5
30	10.9	7.5
40	9.5	6.0
50	8.4	4.7
60	7.5	3.6
70	6.6	2.7
80	6.0	1.8
90	5.2	0.85
100	4.7	0

σ_{HV} must be equal. The decrease in the ratio of depolarized-to-polarized components with respect to the average obtained from a whole range ring can be interpreted in terms of the systematic variation in σ_{HH}/σ_{VV} with angle of incidence as previously reported.³

The less pronounced variation of the ratio of the two principal backscattering coefficients with angle of incidence at 3.8 cm than at 23 cm as shown in Fig. II-9 may be accounted for in several different ways. It may be that the scattering from within the tenuous top layer occurs from irregular structure actually suspended in the layer. If the tenuous layer has a smaller dielectric constant at the surface than deeper in the layer, then the fact that the ratio tends toward unity with decreasing wavelength may be taken as evidence of the gradual change in the material properties with depth. It may also be that a sufficient number of small rocks or pebbles lying on top of the tenuous layer may account for a significant amount of scattering at 3.8 cm but not at 23 cm, and this may explain the observations.

2. Lunar Scattering Law at 3.8-cm Wavelength

The observations of the lunar scattering behavior at 23-cm wavelength as described so far only represent a small part of the work required by our contract with NASA. Additional measurements are in progress at Haystack to examine the behavior at 3.6-cm wavelength.

The moon's scattering is known to change markedly as a function of wavelength. This arises, it is thought, partly because the surface is covered with an increasing amount of small scale structure and hence appears "rougher" as the wavelength is reduced, and partly because the surface appears inhomogeneous and hence different wavelengths penetrate to different depths.

Previously X-band observations were made of the moon in 1962 by Evans⁴ using the Lincoln Laboratory - Camp Parks radar. Better accuracy is expected from the Haystack system because of the better pointing accuracy and superior signal-to-noise ratio provided by the Haystack radar, coupled with the better range tracking and integration techniques available with the Millstone radar sequencer and SDS 9300 computer combination.

Observations were made with Haystack each morning from Wednesday, 16 March through Saturday, 19 March for about 7 hours. At Millstone the antenna beam illuminates essentially the whole moon so that the complete law for the variation of echo power with delay can be established with the beam directed at the moon's center. In practice it is usually necessary to employ a variety of pulse lengths so that good delay resolution can be obtained for the region around the subradar point, and yet good signal-to-noise ratio may be had for the limbs. At Haystack the pulse length must be varied and, in addition, the beam must be scanned off center. In the measurements made in March, a pulse of 10 μ sec with a 10- μ sec associated sample spacing was employed to explore the central region. Measurements were made for periods of 5 minutes for beam positions of 0 to 5 arc minutes with respect to the center in 1-arc-minute steps. The beam was scanned away from the center in four mutually perpendicular directions. The region 6 to 12 arc minutes from the center was later explored in 1-arc-minute steps, using 40- μ sec pulses and an associated 20- μ sec sample interval. The beam was scanned away from the center in 8 directions, intersecting at 45° angles. Finally, the limb region 12 to 15 arc minutes from the center was explored in the same 8 directions, using a 100- μ sec sample interval.

Section II

TABLE II-3
RELATIVE ECHO POWER VS DELAY FOR THE MOON
OBSERVED AT LINCOLN LABORATORY M. I. T.

Delay (t) (μ sec)	ϕ°	$\lambda = 3.6 \text{ cm}^*$	23 cm †	68 cm ‡ (db)	Delay (t) (msec)	ϕ°	$\lambda = 3.6 \text{ cm}$	23 cm	68 cm (db)
10	2.38	0	0	0	2.0	34.16	-12.5	-18.65	-21.8
20	3.37	-0.6	-0.85	-0.6	2.25	36.30	-12.9	-19.1	-22.3
30	4.11	-1.15	-1.40	-1.5	2.50	38.33	-13.35	-19.55	-22.7
40	4.77	-1.55	-1.9	-2.2	2.75	40.28	-13.75	-19.85	-23.1
50	5.31	-1.9	-2.35	-2.8	3.0	42.16	-14.05	-20.2	-23.5
60	5.83	-2.2	-2.75	-3.3	3.25	43.97	-14.4	-20.5	-23.8
70	6.30	-2.5	-3.15	-3.8	3.50	45.72	-14.7	-20.85	-24.1
80	6.73	-2.75	-3.55	-4.3	3.75	47.42	-15.0	-21.15	-24.3
90	7.13	-3.0	-3.95	-4.8	4.0	49.08	-15.3	-21.4	-24.5
100	7.53	-3.2	-4.3	-5.2	4.25	50.69	-15.55	-21.7	-24.7
125	8.42	-3.75	-5.05	-6.2	4.50	52.27	-15.8	-21.95	-24.9
150	9.22	-4.2	-5.8	-7.0	4.75	53.82	-16.1	-22.35	-25.1
175	9.96	-4.55	-6.45	-7.7	5.0	55.33	-16.3	-22.5	-25.35
200	10.65	-4.9	-7.0	-8.4	5.25	56.82	-16.6	-22.75	-25.6
225	11.30	-5.2	-7.5	-9.0	5.50	58.29	-16.9	-23.05	-25.9
250	11.92	-5.5	-8.0	-9.7	5.75	59.72	-17.15	-23.3	-26.15
275	12.50	-5.85	-8.45	-10.15	6.0	60.95	-17.5	-23.6	-26.45
300	13.06	-6.1	-8.85	-10.7	6.25	62.55	-17.8	-23.85	-26.8
325	13.60	-6.4	-9.2	-11.1	6.50	63.93	-18.1	-24.2	-27.15
350	14.11	-6.65	-9.55	-11.6	6.75	65.36	-18.5	-24.55	-27.5
375	14.60	-6.9	-9.9	-11.9	7.0	66.65	-18.9	-24.95	-27.85
400	15.09	-7.15	-10.2	-12.35	7.25	67.98	-19.3	-25.35	-28.25
425	15.56	-7.4	-10.5	-12.7	7.50	69.31	-19.7	-25.8	-28.65
450	16.01	-7.6	-10.8	-13.0	7.75	70.63	-20.2	-26.2	-29.0
475	16.45	-7.8	-11.2	-13.3	8.0	71.94	-20.6	-26.65	-29.45
500	16.88	-7.95	-11.35	-13.6	8.25	73.23	-21.05	-27.1	-29.95
600	18.51	-8.5	-12.3	-14.6	8.50	74.53	-21.55	-27.6	-30.45
700	20.01	-9.0	-13.2	-15.4	8.75	75.79	-22.05	-28.15	-30.95
800	21.40	-9.4	-14.0	-16.2	9.0	77.06	-22.55	-28.7	-31.5
900	22.72	-9.8	-14.6	-16.9	9.25	78.33	-23.15	-29.3	-32.1
1000	23.96	-10.1	-15.35	-17.6	9.50	79.59	-23.7	-29.95	-32.75
1100	25.16	-10.25	-15.95	-18.25	9.75	80.84	-24.5	-30.6	-33.35
1200	26.29	-10.75	-16.4	-18.9	10.0	82.09	-25.2	-31.35	-34.05
1300	27.39	-11.0	-16.8	-19.5	10.25	83.34	-26.1	-32.2	-34.9
1400	28.44	-11.25	-17.15	-20.0	10.50	84.58	-27.1	-33.25	-35.9
1500	29.42	-11.5	-17.45	-20.4	10.75	85.82	-28.5	-34.35	-36.9
					11.0	87.06	-30.0	-35.85	-38.35
					11.25	88.29	-31.2	-37.7	-40.1
					11.50	89.53	-32.0	-40.35	-42.7
<p>* Pulse = 10 μsec; resolution at the receiver = 10 μsec. † Pulse = 10 μsec; resolution at the receiver = 10 μsec. ‡ Pulse = 12 μsec; resolution at the receiver = 10 μsec.</p>									

In all these observations the antenna offsets from the moon's center were inserted manually. The timing of the Haystack radar was locked to that at Millstone so that the Millstone radar sequencer (Craig/Fleck machine) could be used to sample the echoes as in earlier Venus runs. One change for the moon was that the IF signal transmitted to Millstone via the intersite coupling was at 2 MHz instead of 200 kHz, so that adequate bandwidth (100 kHz) could be obtained for the 10- μ sec pulse measurements. The runs were processed at Millstone using the SDS 9300 computer to obtain the integrated echo power vs delay. The speed of this program is such that the data integration is completed shortly after the end of the operation.

Only one difficulty was encountered during these operations. This was the failure of the power amplifier pulse modulator to operate continuously above approximately 30-kv applied voltage. It was necessary to bring up the voltage slowly during the first hour in order to reach 75-kw peak power output. Even at this level, however, the modulator safety circuits would trip intermittently.

The data obtained in the manner described above have been analyzed to obtain the plot of echo power vs delay shown in Fig. II-10. In order to obtain this plot, it was necessary to average all the echo power vs delay plots obtained for a given antenna offset at different angular locations on the lunar disk and then to correct this mean curve for the weighting imposed by the antenna beam. In this way portions of the total curve were built up. A check on the accuracy of the procedure was afforded by a comparison of the curves in the regions where they overlap. A change in the assumed beam shape was required before such consistency was achieved. The curve shown in Fig. II-10 is in reasonable agreement with the earlier results, but provides better resolution for the delay region of 10 to 200 μ sec.

Fig. II-10. Lunar echo power vs delay at $\lambda = 3.8$ cm.

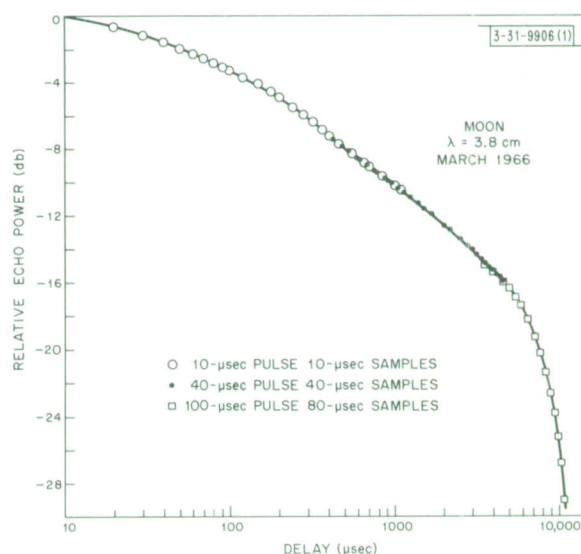


Table II-3 lists the scattering laws obtained for the moon at $\lambda = 68$ cm, $\lambda = 23$ cm and $\lambda = 3.8$ cm, using Lincoln Laboratory radars. Since the resolution in delay was the same in all three sets of measurements, these data should accurately reflect the change in scattering behavior with wavelength.

J. V. Evans
T. Hagfors

C. PLANETARY STUDIES

1. Radar Observations of Venus at Millstone

Venus was observed at Millstone ($\lambda = 23$ cm) from 22 October 1965 to 7 April 1966. The range was determined to an accuracy of $\pm 10 \mu\text{sec}$ from 27 December to 21 March at approximately 3- to 4-day intervals. The measurements terminated somewhat earlier than anticipated owing to poor signal-to-noise ratio, which was later attributed to damage caused by the transmitter to the receiver coaxial line. These range determinations together with those obtained in 1964 at Millstone, and in 1964 and 1965 at the Arecibo Ionospheric Observatory have been used to refine the elements of the orbits of earth and Venus⁵ and redetermine the earth/moon mass ratio. A preliminary reduction of the data has yielded a value of $81,305 \pm 0.005$ for this latter ratio (Smith, *et al.*⁶) which is in good agreement with the recently adopted value.

The scattering law for Venus was determined in 1964 (Evans, *et al.*,⁷), using a combination of short pulse measurements. Russian workers⁸ have reported a change in the scattering law from one year to the next at a 40-cm wavelength. In our view this seems most unlikely because Venus rotates in such a manner that approximately the same face is presented toward the earth at successive inferior conjunctions. Thus the change in the scattering behavior reported by the Russian workers is, we feel, more readily explained as an instrumental effect arising from the much improved delay resolution that they achieved in 1964. Nevertheless, during the 1966 conjunction the scattering law at 23-cm wavelength was redetermined by using methods essentially the same as those employed in 1964. Figure II-11 compares the new and old results. It can be seen that to the accuracy of these measurements there is no difference between the two sets of measurements.

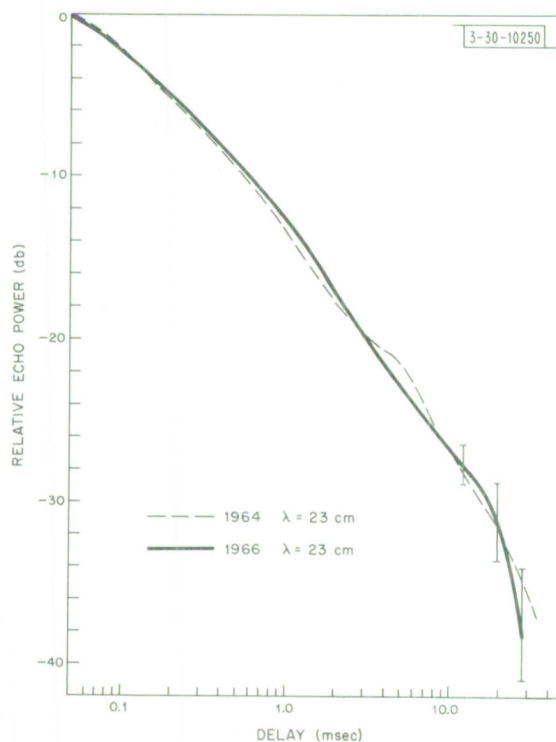


Fig. II-11. Echo power vs delay law observed in 1966 is here compared with that derived by Evans, *et al.*⁷ during 1964. Agreement between two curves would appear to refute conclusion of Kotel'nikov, *et al.*⁸ that law changes from one inferior conjunction to next.

The depolarized circular component of the echoes was observed for the first time at 23-cm wavelength during this series of measurements. The complete scattering law for this component could not be obtained owing to the weakness of the echoes. It was estimated that the total power in this component was 15 db lower than that in the expected sense. Attempts to look for a polarizing effect attributable to a surface layer similar to that described by Hagfors, *et al.*³ from radar observations of the moon, failed because of inadequate signal strength at a delay where such an effect would be expected. The cross section of Venus was determined on a number of occasions and the average was of the order of 18 percent. This is somewhat higher than the mean (15 percent) observed in 1964, though not significantly so.

2. Radar Observations of Venus at Haystack

Karp, *et al.*⁹ made observations of Venus at X-band (3.6-cm wavelength) using the West Ford bistatic radar system. They made the surprising discovery that the cross section was at least a factor of ten lower than that observed at S-band (12.5 cm) and longer wavelengths. The most obvious interpretation of this result would be that attenuation of the X-band signals occurs in traversing the atmosphere of Venus. However, the spectrum of the signals obtained by Karp, *et al.* was wider than would be expected if the signals were reflected from the solid surface, so that a combination of atmospheric absorption together with a scattering agent in the atmosphere (rain or ice) seemed to be required to explain these early results.

CW radar measurements of the cross section of Venus have been made at 3.8-cm wavelength using the Haystack radar system on the days listed in Table II-4. The results shown in this table amply confirm the low value (~ 1 percent) obtained by Karp, *et al.*, although some fluctuation in the cross section has been observed, commencing about 9 weeks after inferior conjunction. The depolarized circular component of the echoes (Table II-4) is found to be ~ 14 db weaker than the expected component — in fair agreement with the ratio observed at longer wavelengths.

The spectrum of the reflected signals has been determined by processing in the CDC 3200 computer signal samples taken at a rate of 500 Hz. Figure II-12 gives an example of such a spectrum. On the basis of these results it can be stated that the echoes are reflected from the solid surface for the following reasons: (a) The center Doppler shift of the echo corresponds precisely to that estimated from simultaneous measurements at Millstone. It is inconceivable that an atmospheric scattering agent could be supported above the surface in such a way that the height with respect to the surface changes at less than ± 5 cm/sec (the velocity accuracy of the measurements). (b) The spectral width of the signals corresponds in all cases to that predicted on the assumption that the echoes are reflected only from the surface. This predicted Doppler width (center to limb) is listed in Table II-4 as f_{\max} and indicated in Fig. II-12 by arrows. (c) Some of the fine structure in the spectra (Fig. II-12) can be attributed to locally rough regions on the surface of Venus. Indeed, it is possible to identify the same features in successive spectra shifted in position owing to the apparent rotation of the planet. In addition, some of these features are apparently the same as those observed in 1964 by Goldstein¹⁰ and Carpenter.¹¹

As a conclusive test that echoes are reflected from the planetary surface, short-pulse range determinations were made nearly simultaneously at Millstone and Haystack. For these

Section II

TABLE II-4
CW OBSERVATIONS OF VENUS

Date (1966)	f_{\max} (Hz)	T_{echo} ($^{\circ}\text{K}$)	b (Hz)	Correction for Terrestrial Atmospheric Attenuation (db)	Cross Section ($\% \pi a^2$)
(a) Polarized Component					
18 Jan.	65.7	400.0 ± 0.4	130.85	0	1.44
1 Feb.	61.0	325.63 ± 0.5	121.08	0	1.10
9 Feb.	76.9	213.55 ± 0.3	152.33	0.2	1.34
15 Feb.	91.6	105.25 ± 0.51	181.6	1.2	1.11
21 March	140.8	8.89 ± 0.54	289.08	0	1.22
30 March	146.5	9.28 ± 0.16	289.08	0	2.08
15 April	154.3	4.51 ± 0.25	304.69	0	2.92
5 May	161.4	1.28 ± 0.24	304.69	0	1.33
17 May	164.5	1.39 ± 0.21	304.69	0	2.29
28 May	166.0	1.02 ± 0.33	304.69	1.3	3.28
15 June	165.6	$1.23 \pm .09$	117.19	0	1.56
27 June	163.2	$0.83 \pm .09$	117.19	0	1.29
(b) Depolarized Component					
19 Jan.	64.0	15.94 ± 0.41	132.82	0	0.057
4 Feb.	65.9	12.63 ± 0.40	132.82	0	0.052

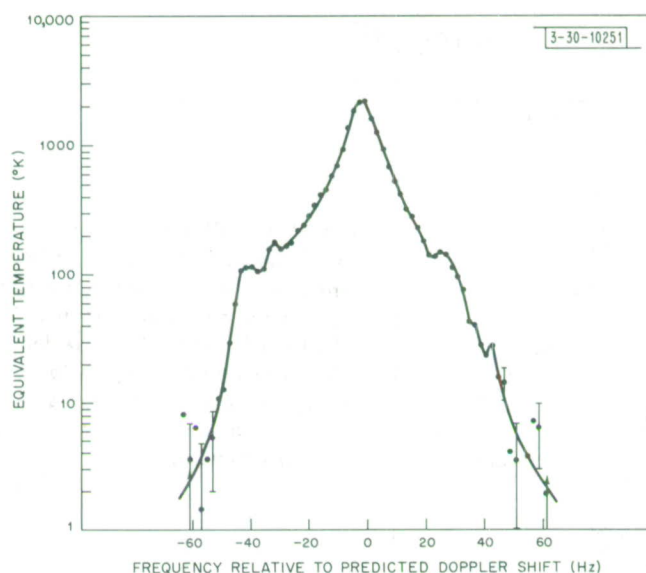


Fig. II-12. Venus power spectrum observed at 3.8-cm wavelength on 1 February 1966. Expected position for reflections from limbs have been indicated by arrows. Note bumps in spectrum which are thought to be reflections from anomalously rough regions on surface of Venus.

the same phase code modulation scheme was applied to the transmitted pulses and the echoes were "compressed," using the same matched-filter delay line. For observations on 24 January and 4 February when the shortest pulses (40 μ sec) were employed, the residuals with respect to a common ephemeris agreed to within 5 μ sec, although the accuracy of each measurement was only approximately ± 10 μ sec. Further, the shapes of the echoes at the two wavelengths were nearly identical, providing separate evidence that the 3.8-cm echo is from the planetary surface (Fig. II-13).

Since the echoes are reflected from the surface we must attribute the low cross section to the effects of atmospheric attenuation, a low intrinsic surface reflectivity or a combination of the two. A low surface reflectivity would require a layer of lossy material overlying the surface, which is not more than about one wavelength thick. While one cannot exclude this explanation, it does seem artificial, and hence a search was conducted for the limb darkening that should be present if atmospheric attenuation is present. Two approaches were adopted. In the first the average of the four best signal spectra was obtained and transformed (using the Bessel transformation routine of T. Hagfors) to yield the angular power spectrum $\bar{P}(\varphi)_X$ of the X-band signals. As a comparison law the mean S-band spectrum reported by Muhleman¹² was similarly transformed to yield the angular scattering law $\bar{P}(\varphi)_S$ at S-band. It was then assumed that in the absence of atmospheric attenuation these two would be the same, i.e., that the scattering law does not change rapidly with wavelength. In the case of the moon this assumption would not hold, but Venus appears to be considerably smoother than the moon, and no clear-cut wavelength dependence has been detected in the scattering law thus far. If the one-way zenithal attenuation

Section II

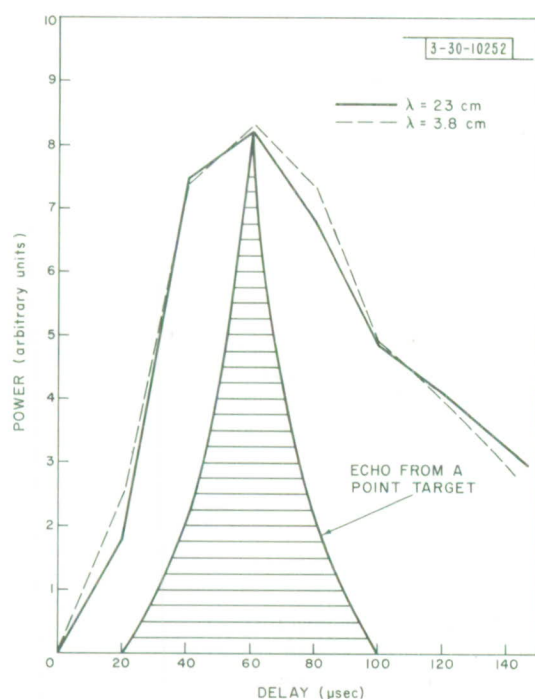


Fig. II-13. Plots of echo power vs delay observed at 23- and 3.8-cm wavelengths on 24 January 1966 when two radars were modulated using same coded pulse waveform, and reflected signals processed in identical fashion. Absolute delays at two frequencies were found to agree to within experimental error, and echo shapes are strikingly alike. This confirms that the surface is responsible for scattering at both wavelengths.

in the atmosphere of Venus is A db we expect the two laws to differ according to

$$10 \log_{10} \bar{P}(\varphi)_S - 10 \log_{10} \bar{P}(\varphi)_X = 2A[\sec \varphi - 1] \text{ db} \quad (1)$$

This expression assumes rectilinear propagation and that the attenuating layer has a height extent that is very small compared with the planetary radius. The results obtained for the difference did exhibit a $\sec \varphi$ dependence, and they suggest a value $A = 1.5 - 2.0$ db.

In the second approach the angular scattering law $\bar{P}(\varphi)_X$ was determined directly from a series of short-pulse experiments. Pulses of 40, 360, 500 μsec , 1.0 and 4.0 msec, were employed to construct the mean echo power vs delay curve $\bar{P}(t)_X$. This was then compared with the function obtained at Millstone in a similar manner. The uncertainty in $\bar{P}(t)_X$ is somewhat larger than that in the mean X-band spectrum, because of the reduced average power achieved when operating the Haystack radar in a pulse mode. A comparison of the X- and L-band scattering laws in the limb region indicated a value $A = 2.5 - 3.0$ db. The difference between this result and that obtained from an examination of the spectra may stem from a difference between $\bar{P}(\theta)$ at 23- and at 12.5-cm wavelength, or may be simply due to experimental error. In any event we conclude that atmospheric attenuation is present but that the zenithal absorption is only of the order of 2 db one way, and not 5 db as anticipated from the cross-section measurements.

It should be pointed out that the above tests for atmospheric attenuation depend upon the scattering behavior near the limbs, whereas the largest part of the echo energy is reflected from the center of the disk. Thus a variation of the attenuation over the face of the planet might account for the difference between the value of A inferred from the observed limb darkening and the low cross section.

The variation in cross section observed with date (Table II-4) supports the view that the attenuation may vary over the face of the disk. It would then seem that the absorbing agent may be a constituent of the atmosphere (like water vapor) whose abundance may be controlled by large scale weather patterns. Plummer and Strong¹³ have argued for such a model on the basis of a number of lines of reasoning. However, it may still be possible to reconcile a dense $\text{CO}_2\text{-N}_2$ model atmosphere with the observations if the height of the terrain near the subradar point with respect to the mean surface varies by several kilometers, since the absorption is expected to vary with the square of the atmospheric pressure.

J. V. Evans
R. P. Ingalls

REFERENCES

1. J. V. Evans and T. Hagfors, "Radio Echo Studies of the Moon at 23 cm Wavelength," J. Geophys. Res. (in press).
2. J. V. Evans and G.H. Pettengill, "The Scattering Behavior of the Moon at Wavelengths of 3.6, 68 and 784 Centimeters," J. Geophys. Res. 68, 423-447 (1963).
3. T. Hagfors, R.A. Brockelman, H.H. Danforth, L.B. Hanson and G.M. Hyde, "Tenuous Surface Layer on the Moon: Evidence Derived from Radar Observations," Science 150, 1153-1156 (1965).
4. J. V. Evans, "Radio-Echo Observations of the Moon at 3.6-cm Wavelength," Technical Report 256, Lincoln Laboratory, M.I.T. (19 February 1962), DDC 274669.
5. M. E. Ash, W. B. Smith and I. I. Shapiro, private communication.
6. W. B. Smith, I. I. Shapiro and M. E. Ash, private communication.
7. J. V. Evans, *et al.*, Astron. J. 70, 486 (1965).
8. V. A. Kotelnikov, *et al.*, Doklady Akad. Nauk SSSR 163, 50 [English Transl. Soviet Phys. - Doklady. 1965].
9. D. Karp, W. E. Morrow and W. B. Smith, Icarus 3, 473, (1964), DDC 613893.
10. R. M. Goldstein, J. Research, Natl. Bur. Standards 69D, 1623 (1965).
11. R. L. Carpenter, Astron. J. 71, 142 (1966).
12. D. O. Muhleman, J. Research, Natl. Bur. Standards 69D, 1630 (1965).
13. W. T. Plummer and J. Strong, Astronautic Acta. 11, 365 (1965).

III. RADIO ASTRONOMY

A. DIGITAL MAPPING PROCEDURE APPLIED TO GALACTIC CENTER

The problem of producing contour maps from measurements of antenna temperature with a radio telescope can, in principle, be handled automatically with a digital computer. The present program is designed to produce contour plots from radiometric drift scans in as much detail as the antenna resolution permits.¹ The problem is to obtain a record of the observations (time, antenna coordinates, and observed antenna temperatures) in a form which can conveniently be read into a computer. The Haystack radiometric system, described in the last report² produces these records on magnetic tape. The mapping program uses these particular tapes as input, but can be adapted to handle similar data taken on other radio telescopes in the form of a series of drift scans across the source, spaced one-half beamwidth apart. An IBM 7094 computer and a Stromberg-Carlson 4020 display device were used for data processing.

The region mapped in the first application of this computer program was centered on the radio source Sagittarius A, believed to be the center of our galaxy. The data were taken jointly with Dr. Alan Maxwell and Mr. Dennis Downes of Harvard University, and manually drawn maps of the central region have been previously published.³ The present map was prepared by computer from the data taken with the 8-GHz Haystack radiometer. This radiometer consists of two channels, each 500 MHz wide, centered at 7750 and 8250 MHz. For a 1-sec integration period, the root-mean-square fluctuations are about 0.1°K for each channel. All the data were taken in drift scans with the observed antenna temperatures consisting of 2-sec integrals of the radiometer output with the recorded antenna pointing in right ascension α , and declination δ , corresponding to the center of each integration interval. The details of the on-line radiometric data system are described in a previous report.⁴ The half-power beamwidth of the Haystack antenna is 4.2 arc minutes at this frequency.

The mapping program consists of three parts: Program A which produces smoothed plots of each drift scan, showing each radiometer channel separately; Program B which compiles coincident drift scans including one or both channels as specified; and Program C which produces an automatic plot of the contour map. These programs run in series, giving the observer a look at the processed data after each step. A more detailed description of each program is given below.

Program A:— The recorded data tapes are read by Program A. A specified length of record at the beginning and at the end of each scan (intervals greater than two beamwidths in each case) are used as baseline data and possible linear drifts in baseline are removed from the central portions of the scan. The data points are then smoothed and interpolated by means of Subroutine Smooth, which fits a Fourier sine series to the observed data. The series is truncated at the highest angular frequency which the antenna resolution permits. The number of Fourier coefficients used is $2\theta/\beta$, where $\theta = (\text{RA interval of scan}) \cos \delta$ and β is the half-power beamwidth. Subroutine Smooth produces the proper smoothing⁵ and interpolates the data to a standard set of equally spaced right ascensions. Thus the data are registered in preparation for

Section III

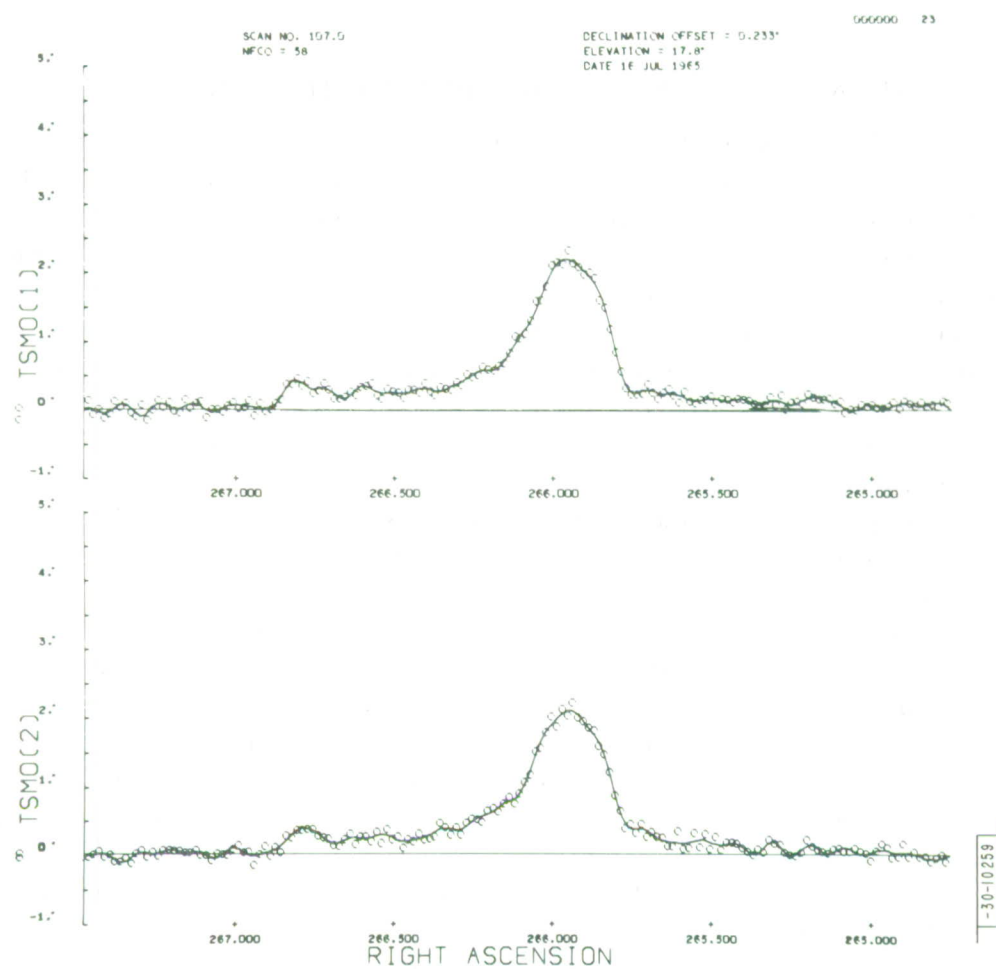


Fig. III-1. Example of graphical output of Program A.

Programs B and C. Figure III-1 shows an example of the graphical output of Program A. The observed data points are plotted as well as the smooth curves for both channels. In addition to these output plots, a magnetic tape record of the smoothed, interpolated data is also written for Program B.

Program B:- After examination of the individual scans above, the observer may omit individual channel records if interference or equipment difficulties are apparent. Program B uses the tape output of A together with editing information on punched cards, indicating the scans to be averaged and the channel to be omitted on specific scans. Program B makes an atmosphere attenuation correction to each scan, averages coincident scans together, and calls Subroutine Smooth for the averaged data for scans at each declination. The antenna temperatures are corrected for atmospheric attenuation by dividing by $\exp[-\tau_0 \sec \Theta]$, where τ_0 is the zenith attenuation and Θ is the zenith angle of the antenna beam. The zenith attenuation τ_0 was determined from radiometric observations of the center of the moon; a value $\tau_0 = 0.023$ (or 0.1 db) was used. Figure III-2 shows an example of the graphical output from this program. Data points from Program A are also plotted.

Program C:- All the information necessary to plot a contour map made with an axially symmetric antenna of resolution β is contained in a regular array of antenna temperature values at positions spaced at intervals $\beta/2$ in right ascension and declination.⁶ Program C assembles such an array, termed the data matrix, from the output of Program B. The contour curves, however, are computed from an array which is more finely subdivided than the Data Matrix. In the present case the spacing of this array, the Augmented Matrix, was $\beta/8$. The program is written so that subsections of the Data Matrix can be interpolated to obtain Augmented Matrices which do not exceed the memory capacity of the computer. A large map can thus be assembled in sections. Interpolation from the Data Matrix to the Augmented Matrix is done by using Subroutine Smooth, first parallel to the right ascension axis and then parallel to the declination axis. The contour lines are determined by computing the intersection points of a given contour level with a rectangular grid which has intersections at the coordinate points of the Augmented Matrix. Linear interpolation is used to locate these intersection points between pairs of adjacent points on the grid. The contour lines are plotted with a series of straight-line segments connecting the grid intersection points. Figure III-3 shows a plot of the contours for the galactic center region exactly as plotted on the SC4020 graphical output device.

The brightest region in Fig. III-3 is the radio source Sagittarius A. These observations confirm that the microwave spectrum of Sagittarius A is nonthermal⁷ and show that the diameter of the source is about 3.5 minutes of arc. The contours north of Sagittarius A evidently correspond to thermal sources which appear to be still unresolved with a beamwidth of 4.2 minutes of arc.

M. L. Meeks
J. C. Henry

B. REAL-TIME PROGRAM FOR SPECTRAL LINE MEASUREMENTS AT HAYSTACK

Microwave spectral analysis is performed "on-line" by the same computer which guides the Haystack antenna. In addition to its previous duties of antenna-pointing and real-time radiometric data reduction, the Univac 490 computer now also sums 100 channels of data from the

Section III

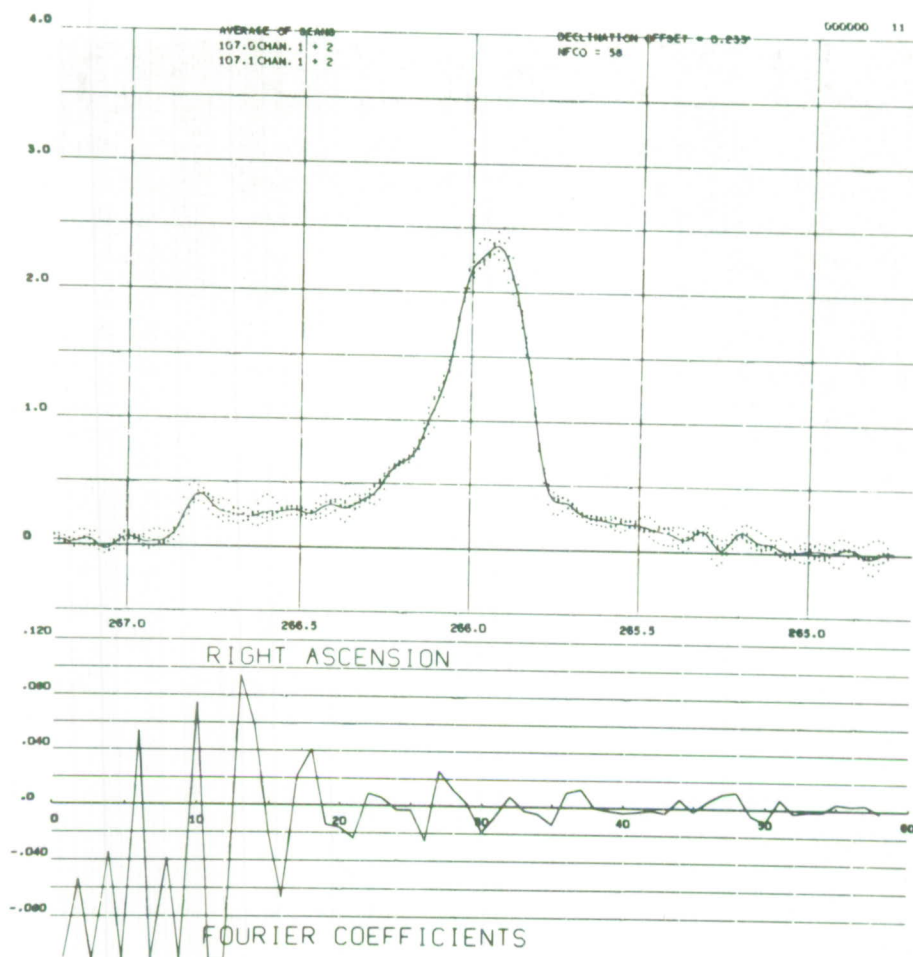


Fig. III-2. Example of graphical output of Program B.

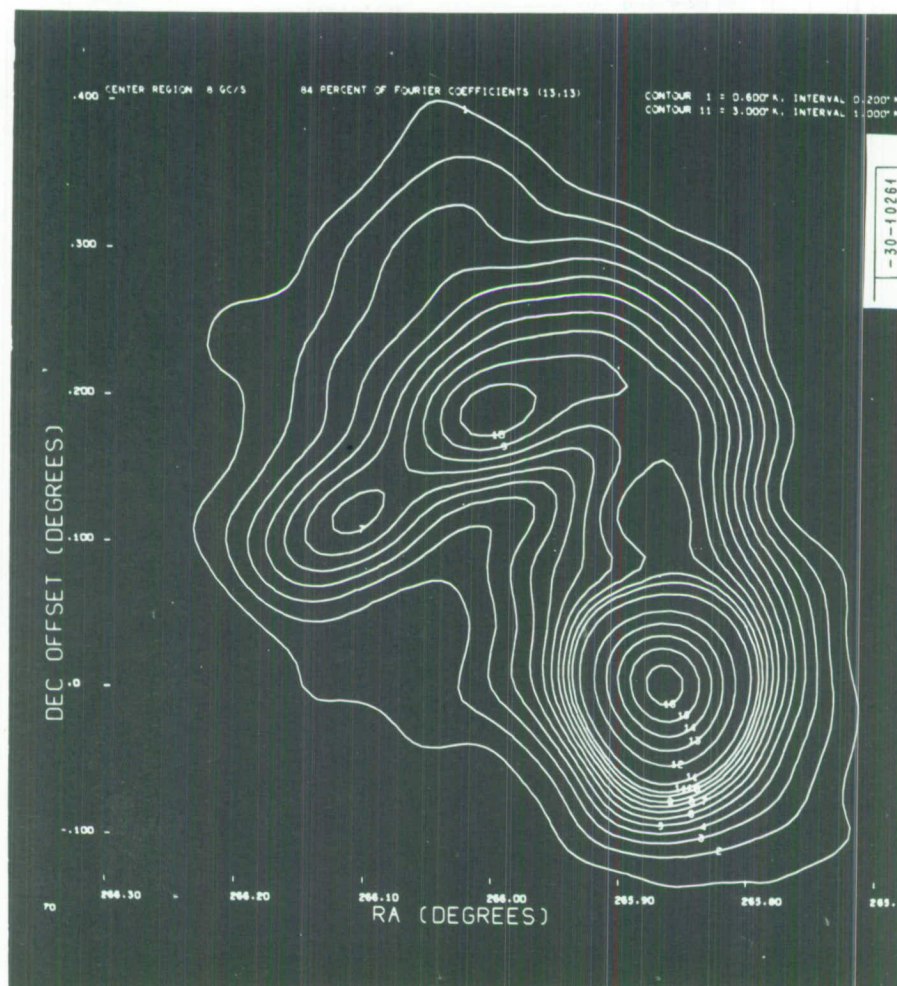


Fig. III-3. Contour map of the Sagittarius A region at 3.7 cm wavelength. This map was prepared by the SC4020 output device from contours computed in the IBM 7094.

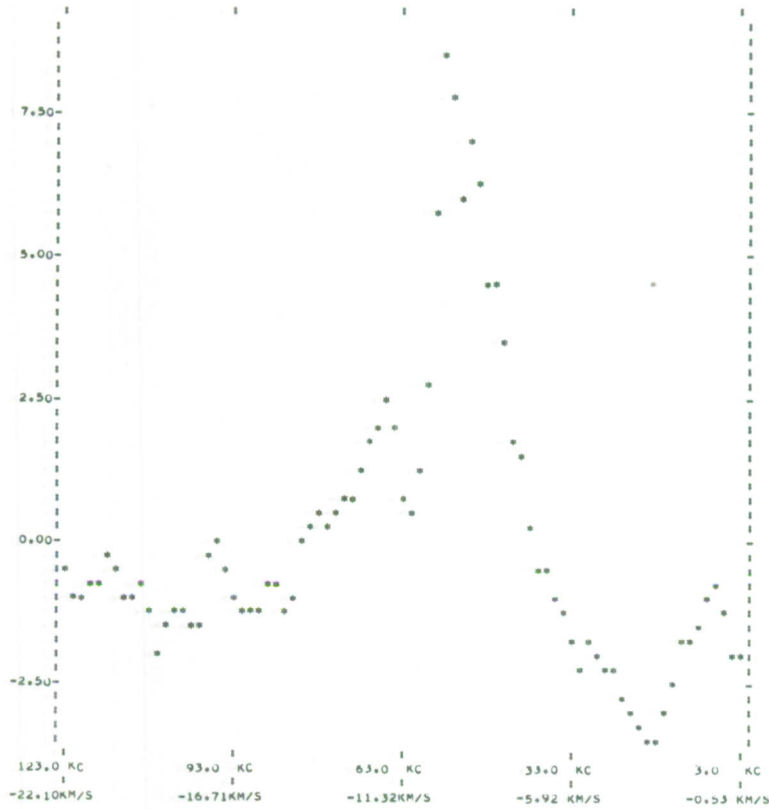
Section III

1.66GC--CLAVIN FEED--LINEAR POL.--OLD PARAMP--BALL
NGC 6334
POLPOS 0

4/13/66

DAY-- 103

T(21-181)



END GMT 07138125
START GMT 07123123
CAL GMT 07121145
DURATION 889.5
RA (H:M:S) 17 18 05
LHA 22 58 34
DEC (D:M:S) 35 42 11
FLSR (KC) 63.0
B (KC) 120.0
FO (KC) 1667358
FLO (KC) 45988.709
RESOLUTION 3.00
TA -1.04
UEL+TA 0.66
TSYS 365.83
SPECTRALDT 0.56
SLOPE-COR. 0.0
SLOPE MEAS 9.4
ERRORS 50

130-1062

Fig. III-4. Output of the spectral line program showing antenna temperature vs frequency.

Digital Autocorrelator. On recognizing the end of the preset integration period, the computer program transforms the multichannel sums, to produce a spectrum which is immediately printed out on the high-speed printer as well as on magnetic tape. The observer can select many options, some via console switches, others via typewriter dialog.

During transforming and printing (plotting), the computer program avoids summing of further data, but continues the antenna pointing. The spectral summations, performed in a burst of 200 every $1/5$ second, may go on for hours of integration. Not quite 20 seconds are needed for the three-page high-speed printout, whereas the transformations take only about 5 seconds in spite of concurrent requirements for pointing the antenna. The mathematical basis for the computation, and the design of the Digital Autocorrelator have been described by Weinreb.⁸

The three printed pages include one containing the Main Data Plot (Fig. III-4) of the temperature profile $T_i = T(f)$. Abscissas are always displayed both as frequencies f_i and as equivalent velocities with respect to the local standard of rest. Ordinates, however, can be altered in appearance if the observer exercises his option to vary the scale and zero line; he may also add a slope-correction factor, which affects the plot but not the ordinate axis values. Every other plotted point is omitted, for brevity, but all 161 points (T_i, f_i) are tabulated on an auxiliary page of the printed output. At the top of each page is printed the title of the run, along with date and day number. The next 3 lines of the Main Data Plot page allow comments, the insertion of which is among the options available to the user. Other options include presetting some of the values of parameters itemized in the legend to the right of the Main Data Plot. In the legend, CAL GMT gives the time at which the user terminated the last prior Cal-Base run sequence.

Console switches, and typewriter dialog, give the observer control over the program. The console switches include the integration-duration dials (values 000 to 999), the 4-position mode switch (STOP, CAL, BASE, OBS) with which the user performs a Cal-Base sequence or starts a spectral Observe run, and eight toggle switches which trigger such actions as replotting, retransformation or reinitializing (including starting a new typewriter dialog).

The typewriter dialog is automatically activated when the AUTOCOR program is first called in from the system tape: after initializing itself, this program identifies itself and types out (Fig. III-5) first a summary of toggle-switch meanings and then a list of some 12 options which can be chosen via typewriter. The user replies by typing a number followed by a carriage return(*).

Several choices result in further dialog. For instance, if the user types 1* for "Comments," the program further inquires which line (1-3) he desires to replace, and on receiving his reply asks for the text of the comment; it then asks for another line choice, etc. (Line choice 0* terminates the "Comments" dialog and returns to the "main" dialog.) If the user chooses 8* for "Slope," the program types out the current slope-correction factor and asks for the new value; similarly, in choice 11* ("Plot-scale") and 12* ("Zero level"), which have been mentioned previously as user-operations which change the appearance of the Main Data Plot. Replying 0* to the "main" dialog terminates it, whereupon the program leaves the initialization section and enters the working section, allowing the observer to start a run.

In summary, the spectral analysis program used at Haystack is characterized by: real-time integration of 100-channel spectral data; transforming and plotting in quasi-realtime (data integration terminated, but antenna pointing continues); quick-look capability implicit in the

Section III

DATA PROCESSING PROGRAM..
NONE(0) AUTOCOR(1) RADIOMETER(2) FOURIER(3)
1*

-30-10263

THIS RDMTR PROGRAM IS THE AUTOCORRELATOR VERSION, DATED 28APR66

S.SW. CONTROLS--
-1 UP MAKES P(I) EQUAL 100. X SD(I) / SC(I)
-2 UP TO RE-INITIALIZE
-3 UP TO RE-DO FOURIER TRANSFORMS
-5 UP REPLOTS LAST TRANSFORM
SW.6-UP FOR UNIT WT.--DOWN FOR WT.W(K)
-7 UP FOR EXTRA PLOTS
-8 UP FOR CONTINUOUS RUNNING.

CHOOSE FURTHER INITIALIZATION DESIRED--
NONE(0), COMMENTS(1), TCAL,TBASE(2), ERASE A,B SUMS(3),
ERASE TRANSFORM-AVERAGES PP(I)AV.(4), F0 AND FLSR(5), DEBUG-SWITCH(6),
FLO(7), SLOPE(8), T(I) ADD(9),SUBTRACT(10), PLOT-SCALE(11), ZERO-LEVEL(12)
1*

CHOOSE LINE(1-3), (0)=NO MORE--
1*

PROCEED, +END LINE W/CAR.RET.

ENTER NAME OF SOURCE HERE*

CHOOSE LINE(1-3), (0)=NO MORE--
2*

CHOOSE ANOTHER--
0*

(NOW WORKING.)

Fig. III-5. Sample of typewriter dialogue for control of spectral line program.

immediate plotting, and especially in unlimited replotting with parameters altered at the will of the observer; magnetic-tape logging of both multi-channel sums and transformed spectrum (plus auxiliary parameters of the run), for later processing by other methods, and for pen-plotter automatic graphical display for publication.

G. Conaut
Consultant
M. L. Meeks

C. STOKES PARAMETERS FOR 1665-MHz OH EMISSION NEAR W3

1. Introduction

The anomalous 1665-MHz spectral line emission from OH near W3 has been observed to be partially linearly polarized by Weinreb, Meeks, Carter, Barrett and Rogers.⁹ Subsequent observations of right and left circular polarization from this source by Barrett and Rogers¹⁰ revealed that all four of the OH transitions at 1612, 1665, 1667 and 1720 MHz produce features in the emission spectrum with predominantly circular polarization.

Linear and circular polarization in the 1665-MHz emission from the W3 source have also been observed by Davies, de Jager and Verschuur.¹¹ This article presents a measurement of

the Stokes parameters as a function of frequency for the 1665-MHz OH emission near W3. The polarization parameters – ellipticity, ellipse position angle, and degree of polarization – are computed and their rapid variation with frequency is described in terms of a simple model.

2. Polarization Parameters

The polarization properties of an electromagnetic wave are completely specified by the four Stokes parameters,¹² which may be determined from measurements of the intensities of the wave with four independent polarizations. If $I(\varphi)$ is the intensity for linear polarization at a position angle φ , and if $I(R)$ and $I(L)$ are the intensities for right and left circular polarizations,* then the Stokes parameters are defined as

$$\begin{aligned} S_0 &= I(0^\circ) + I(90^\circ) = I(R) + I(L) \\ S_1 &= I(0^\circ) - I(90^\circ) \\ S_2 &= I(45^\circ) - I(135^\circ) \\ S_3 &= I(R) - I(L) \end{aligned} \quad (1)$$

These parameters have the property that the polarization of an incoherent superposition of waves is described by Stokes parameters which are just the sums of respective parameters for the separate waves. Other parameters describing the polarization can be obtained from the Stokes parameters as follows. The position angle φ of the major axis of the polarization ellipse is given by

$$\tan(2\varphi) = S_2/S_1 \quad (2)$$

The amplitude ratio of minor-to-major axes b/a for the polarization ellipse is expressed as

$$\tan \chi = \pm b/a \quad (3)$$

where

$$\sin 2\chi = S_3 / \sqrt{S_1^2 + S_2^2 + S_3^2} \quad (4)$$

and the + in Eq.(3) applies to right elliptical and the – to left elliptical polarization. Finally the degree of polarization P is obtained from

$$P = \sqrt{S_1^2 + S_2^2 + S_3^2} / S_0 \quad (5)$$

It is convenient to work with the Stokes parameters because of their additive property, but somewhat better physical insight can be obtained from the ellipse position angle φ , the ellipticity $\pm b/a$, and the degree of polarization P , as defined above.

3. Spectral Line Measurements

Measurements of the polarization parameters for the 1665-MHz OH emission were made with the 120-ft parabolic antenna of the Haystack research facility of Lincoln Laboratory, Massachusetts Institute of Technology, during the period 28 November through 9 December 1965.

* In this paper right circular polarization denotes clockwise rotation of the electric vector when viewed along the direction of propagation.

Section III

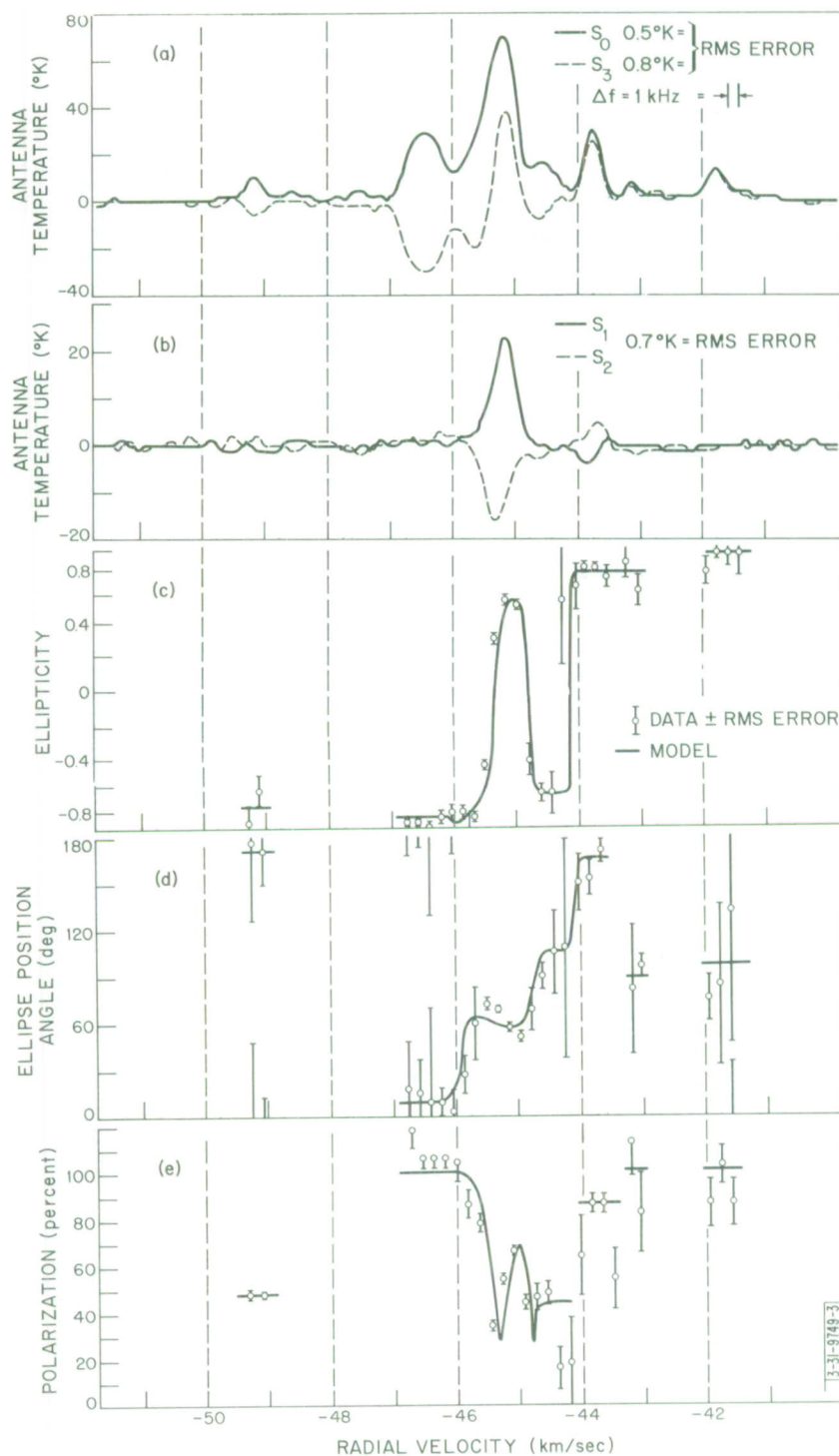


Fig. III-6. Polarization parameters for 1665-MHz OH emission near W3. (a) and (b) show measured values of Stokes parameters. Points plotted in (c), (d) and (e) were computed from Stokes parameters, and solid lines represent values derived from model from -46 to -44 km/sec, or otherwise best estimates of parameters.

The observation of various linear and circular polarizations with a single system made possible a complete determination of the polarization parameters of the spectral features as a function of frequency, or equivalently as a function of radial velocity with respect to the local standard of rest. At this OH-transition frequency a radial velocity of +1 km/sec gives a Doppler shift of -5.555 kHz.

The spectral line radiometer used in these measurements included a 100-channel digital autocorrelator and a room-temperature parametric amplifier. The autocorrelator is tied directly to a real-time computer which produces plots of the observed spectra immediately after each integration period. Most of the observations were made with a 1-kHz frequency resolution, but the brightest features were also examined with 200-Hz resolution. The overall system temperature was 320°K for linear polarization measurements and 360°K for circular polarization; the increased system temperature resulted from a network that combined horizontal and vertical linear polarization to produce the circular polarizations. The observed antenna temperatures for Cassiopeia A continuum emission were 240°K and 180°K , for linear and circular polarization respectively. The isolation of right and left circular polarization was greater than 15 db, and the half-power beamwidth was 22 minutes of arc.

Figure III-6(a) and (b) shows the measured Stokes parameters plotted as a function of radial velocity with the RMS errors and frequency resolution specified. In Fig. III-6(b) the antenna temperature scale has been expanded by a factor of two over that of Fig. III-6(a). It is clear from these curves that the polarization is primarily circular, progressing from totally right circular on the right side of Fig. III-6(a) to totally left circular for the feature just to the left of the central maximum. Figure III-6(b) shows that the amount of linear polarization is relatively small by comparison. The polarization behavior across the central maximum is evidently very complex.

4. Interpretation of Polarization

Once the Stokes parameters have been determined, it is desirable to use them to compute the ellipticity, the ellipse position angle, and the degree of polarization for the emission spectrum. These last three parameters, however, are not proportional to the received signal and can be determined only when the signal-to-noise ratio is sufficiently high.

Equations (3) through (5) were used to compute the ellipticity $\pm b/a$ and the degree of polarization P . The ellipse position angle ϕ was determined as a parameter in the least-square fitting procedure, Eq.(8). The root-mean-square (RMS) errors associated with these three parameters were computed by estimating the RMS errors in the Stokes parameters and assuming linear error-propagation. The polarization parameters and the RMS error bars are shown in Fig. III-6(c), (d), and (e). The plotted points here are separated by an equivalent filter width in frequency; so they represent independent measurements. The large errors are associated with low signal-to-noise ratios, and no points are plotted when the errors become excessive.

The polarization parameters in Fig. III-6 show continuous variation around the central maximum, but outside this region of variability, the polarization parameters appear to remain constant, within experimental error, across the individual emission features. We have used a simple model to describe the variability of the polarization parameters in the region of the central maximum. This model assumes that there are three incoherent emission features in the

TABLE III-1 PARAMETERS FOR 1665-MHz OH EMISSION FEATURES (Radial velocities are with respect to local standard of rest.)						
Radial Velocity (km/sec)	Maximum T _A (°K)	Width Half-maximum (km/sec)	Ellipticity (±b/a)	Ellipse Position Angle (deg)	Polarization (percent)	Comments
-49.13	11.0	0.27	-0.75 (±0.1)	170 (±30)	51 (±3)	Isolated feature
-46.39	28.0	0.68	-0.93 (±0.07)	10 (±10)	100 (-6)	Slightly overlapped feature
-45.42	35.0	0.55	-0.84	65	100	Parameters from model
-45.13	50.0	0.45	+0.65	55	100	Parameters from model
-44.55	16.0	0.50	-0.70	105	100	Parameters from model
-43.73	30.0	0.35	+0.78 (±0.06)	165 (±10)	86 (±6)	Slightly overlapped feature
-43.08	8.0	0.26	+0.78 (±0.2)	90 (±14)	100 (-20)	Isolated feature
-41.73	14.0 (±0.5 RMS)	0.36 (±0.05)	+0.96 (±0.04)	110 (±30)	100 (-12)	Isolated feature

radial velocity interval -46 to -44 km/sec. These features are assumed to be 100-percent polarized and to have Gaussian profiles. Polarization variability then results from incoherent superposition. The problem of fitting this model to the observed polarization parameters in the region of the central maximum is not a simple one. Five parameters are necessary to specify the center frequency, width, peak intensity and polarization of each feature. These parameters were obtained by repeated trial and error with a computer program that combined trial values of the Stokes parameters in this model and plotted the resulting polarization parameters with the observed data superimposed. The solid curves in Fig. III-6(c), (d) and (e) show the best fit that was obtained by this procedure. The parameters that produced this fit are given in Table III-1 which also includes the corresponding parameters for all features in the spectrum shown in Fig. III-6. The overall agreement is good between the observed data and the model in Fig. III-6(c), (d) and (e). However, there are small discrepancies that nevertheless may be large compared with the RMS error bars on the data points. We believe that these discrepancies result from the following causes: (a) the features are not exactly Gaussian in shape; (b) the resolution of 1 kHz is not quite sufficient to completely resolve the spectrum of the source; (c) the cut-and-try fitting procedure did not produce the best-fit parameters. In general, this simple model does indeed appear to fit the observed variations in polarization parameters.

Outside the interval -44 to -46 km/sec in which an overlap of 100-percent polarized features is assumed to account for $P < 1$, only two of the remaining five features are significantly less than 100-percent polarized. The feature at -49.1 km/sec is 51-percent polarized (± 3 RMS error) and the features at -43.7 km/sec is 86-percent polarized (± 6 RMS error).

It has been proposed by Davies, de Jager and Verschuur¹¹ that the Zeeman effect might account for this spectrum. However, the identification of Zeeman components suggested by these authors does not appear consistent with our observed polarization parameters and the results in Table III-1. It is, of course, impossible to say on the basis of our measurement that no combination of simple Zeeman components can produce the observed spectrum for the 1665-MHz transition. But the circular polarization observations of the other three OH transitions from the W3 source by Barrett and Rogers¹⁰ appear to rule out a simple interpretation of this 1665-MHz spectrum in terms of Zeeman splitting.

5. Conclusions

The spectrum of the 1665-MHz OH transition observed near W3 shows the bright, narrow emission features that are characteristic of the anomalous emission associated with interstellar gas clouds near H II regions. A detailed examination of the polarization parameters shows that the spectrum can be interpreted as an incoherent superposition of emission features, each with polarization parameters that are constant across the feature. The features are roughly Gaussian in shape, but some significant deviations from Gaussian shape are observed. Eight features appear to be present in the spectrum, but some additional low-level emission may be present, particularly in the interval -49 to -47 km/sec. Three emission features are observed to be 100-percent polarized within the observational errors. Three other features, which overlap in frequency, are consistent with a model in which the features themselves are 100-percent polarized and the observed degree of polarization is a consequence of an incoherent superposition. The

Section III

TABLE III-2 RADIOMETRIC SYSTEM PARAMETERS			
Quantity	Center Frequency (GHz)		Units
	8.25	15.50	
Bandwidth	500	1000	MHz
Noise temperature	1300	2150	°K
Sensitivity for 1-sec integration	0.10	0.16	°K

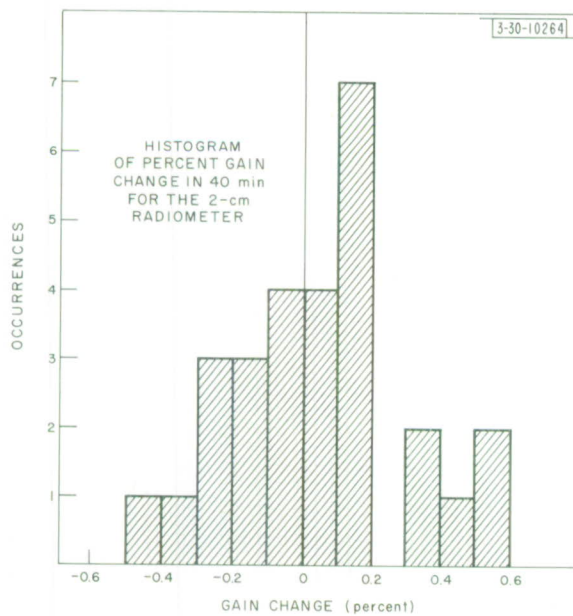


Fig. III-7. Histogram of percent gain change in 40-minute time interval for 2-cm radiometer.

two remaining features are not obviously overlapped, yet give $P < 1$. However, some overlap with low-level emission may be present in these two cases. Generally the observations are consistent with a superposition of 100-percent polarized features that are mutually incoherent. The observed polarization varies continuously from left circular through linear to right elliptical and back to left elliptical between radial velocities of -46 and -44 km/sec. The model simulates this behavior with features that are elliptical with ellipticity $|b/a| \geq 0.65$ or equivalently with linear polarization amounting to 41 percent or less.

The mechanism by which these features are produced is not clearly understood. However, the description of the emission in terms of our simple model makes it possible to conclude that the 1665-MHz emission near W3 is not qualitatively different from that of the other three transitions, notwithstanding the observed variations in the polarization parameters as a function of radial velocity.

M. L. Meeks
J. A. Ball
J. C. Carter

D. ABSOLUTE FLUX MEASUREMENTS OF CASSIOPEIA A AND TAURUS A AT 3.64 AND 1.94 cm

1. Introduction

Measurements of the absolute intensity of the radiation received at the earth from a celestial radio source are important for two reasons: such measurements at different wavelengths yield information about the physical processes occurring in the object itself, and they provide a method of measuring the gain of large antennas which is free of many of the spurious effects associated with the use of pattern transmitters.

The requirements for absolute flux measurements at centimeter wavelengths are: sensitive, stable, accurately calibrated radiometers, and an antenna of known aperture efficiency.

2. Radiometric System

At the Haystack Research Facility, the first requirement previously mentioned has been admirably met with equipment designed by Dr. Sander Weinreb.* Briefly, the radiometers at both frequencies are simple Dicke-switched TRF receivers, employing a cascade of wide-band tunnel diode amplifiers followed by a traveling-wave tube. The signal at the output of the final RF amplifier is split into two 500-MHz bands (as an aid in identifying interference) and delivered first to separate square-law detectors, then synchronously demodulated and applied to linear integrators. The 500-MHz band at 7.75 GHz is frequently hampered by interference; the two channels at 15.25 and 15.75 GHz are averaged after final processing. Table III-2 lists the relevant parameters for the radiometric system.

The great stability of these radiometers is exhibited in Fig. III-7. The overall system has been examined for linearity by means of standard techniques (gas discharge tube and precision attenuator) and correction to the present measurements has been negligible (0.6 percent at 8.25 GHz and 0.1 percent at 15.50 GHz). The calibration noise source in the radiometer has been referred to the temperature difference between a termination at room temperature, and a similar termination immersed in liquid nitrogen. The experimental accuracy of this measurement is better than 1 percent.

* See Ref. 2, Sec. III.

3. Cornucopia Reflector

A horn reflector antenna with approximately 6-m^2 aperture was obtained for observations of the strong radio sources Cassiopeia A and Taurus A. Measurements of the aperture efficiency of this antenna from 2.7 to 16.0 GHz were performed by A. Sotiropoulos, utilizing the substitution method on a simulated free space range. The data have been analyzed by Sotiropoulos and Dr. J. Ruze, who have published these results in a technical report.¹³ The conclusions pertinent to the present observations are presented below.

Frequency (GHz)	η	ρ
8.25	0.719 ± 0.028	633 ± 25
15.25	0.583 ± 0.023	780 ± 31
15.75	0.572 ± 0.023	795 ± 31

where η = aperture efficiency

$\rho = 2k/\eta A_g$ is the number that converts antenna temperature from an unpolarized point source to flux in units of 10^{-26} watts. $\text{m}^2 \cdot \text{Hz}^{-1}$ according to $S_\nu = \rho T_a$. (1)

This antenna is mounted as a transit instrument* movable in elevation along the local meridian, and connected to the radiometer through a rotary joint and a short piece of flexible waveguide. The loss-VSWR combination of this additional plumbing has been measured across the bandwidth of the radiometers and introduces losses of 4.9 percent at 8.25 GHz and 6.2 percent at 15.50 GHz.

4. Observations

Transit observations of the two strong radio sources Cassiopeia A and Taurus A were made during December 1965 and January 1966. Drift scans on a source were taken at several slightly different elevations to remove any pointing error. Each drift scan was corrected for baseline drift, atmospheric attenuation on that particular day, scaled to temperature, and fitted by a Gaussian curve with a least-squares iteration technique. A sample record is shown in Fig. III-8. The resultant peak temperatures at different elevation offsets were again fitted by a Gaussian curve, and the final peak temperature obtained. The data shown in Fig. III-9 illustrated the

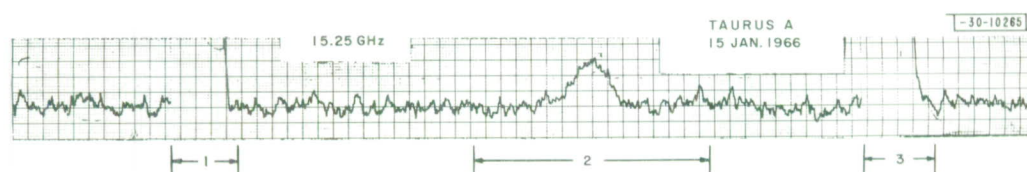


Fig. III-8. Drift scan of Taurus A at 2 cm with Cornucopia horn antenna on 15 January 1966 (region 2). Recording time constant is 10 sec and time lapse from region 1 to region 3 is about 40 minutes.

* See Ref. 2, p. 24.

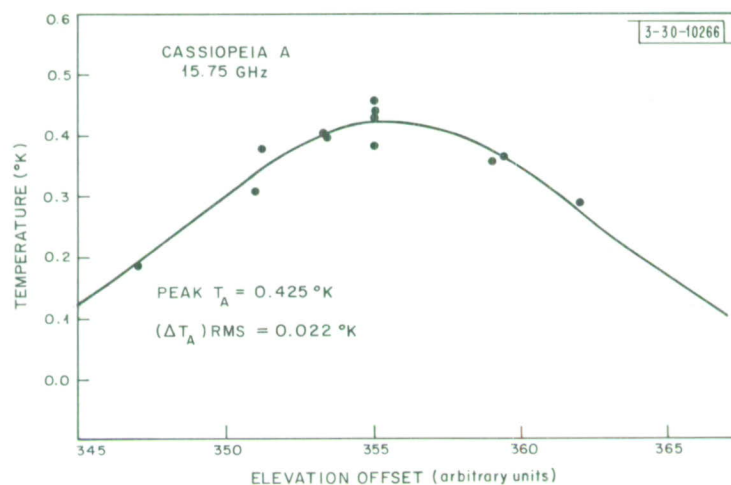


Fig. III-9. Peak temperatures of all drift scans on Cassiopeia A at 15.75 GHz. Solid curve is least-squares Gaussian curve through data points. One unit on abscissa corresponds to approximately 2.2 arc minutes of offset in elevation.

results of drift scans at different elevations. The peak temperatures were corrected for rotary joint loss and source size, and converted to flux using Eq.(1). (The data for Taurus A have also been corrected for polarization.) The tabulation below summarizes the results.

Source	Frequency	Flux
Cassiopeia A	8.25	616 \pm 4.5% RMS
	15.50	380 \pm 6% RMS
Taurus A	8.25	567 \pm 4.5% RMS
	15.50	461 \pm 6% RMS

The data indicate that the spectrum of Cassiopeia A is well represented by a constant spectral index at least to 15.5 GHz, in contradiction to the results of Baars, Mezger, and Wendker.¹⁴ Figure III-10 shows the present observations for Cassiopeia A plotted along with data obtained by other groups listed in Ref. 14. The data for Taurus A agree fairly well with the lower frequency measurements, although a fit to $S_\nu = k_\nu^\alpha$ for constant α is less convincing than for Cassiopeia A. Figure III-11 shows the spectrum of Taurus A.

R. J. Allen
Prof. A. H. Barrett
(Research Laboratory
of Electronics, M.I.T.)

E. SECULAR VARIATIONS IN CENTIMETER RADIO FLUX FROM 3C273

Observations of the quasi-stellar radio source 3C273 have been made at 8.25 and 15.50 GHz with the Haystack antenna. Data obtained during the first few months of 1966 have been compared with similar observations during the spring and summer of 1965. The results at 8.25 GHz indicate a moderate increase in radio flux of 16 percent per year, in agreement with Dent.¹⁵

Section III

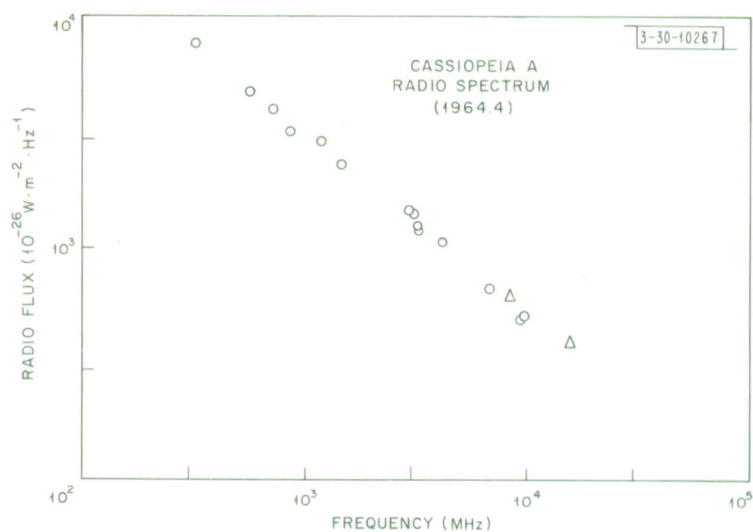


Fig. III-10. Radio spectrum of Cassiopeia A(a). Present measurements are shown as open triangles. Open circles are previously published measurements of less than 10-percent quoted error.

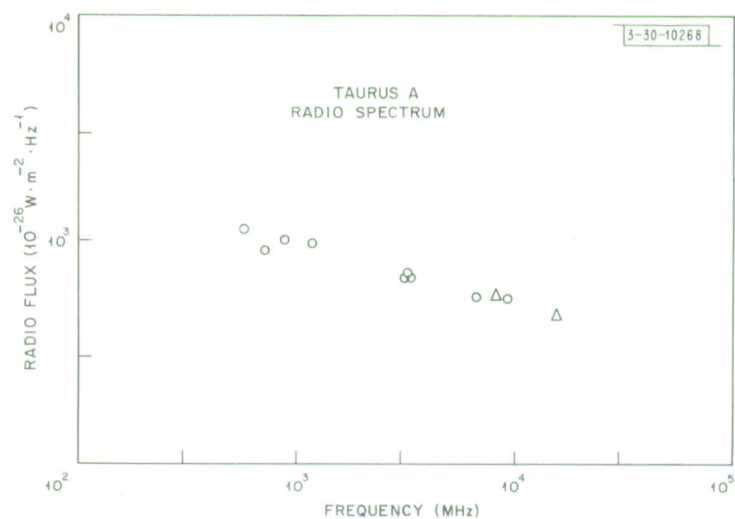


Fig. III-11. Radio spectrum of Taurus A.

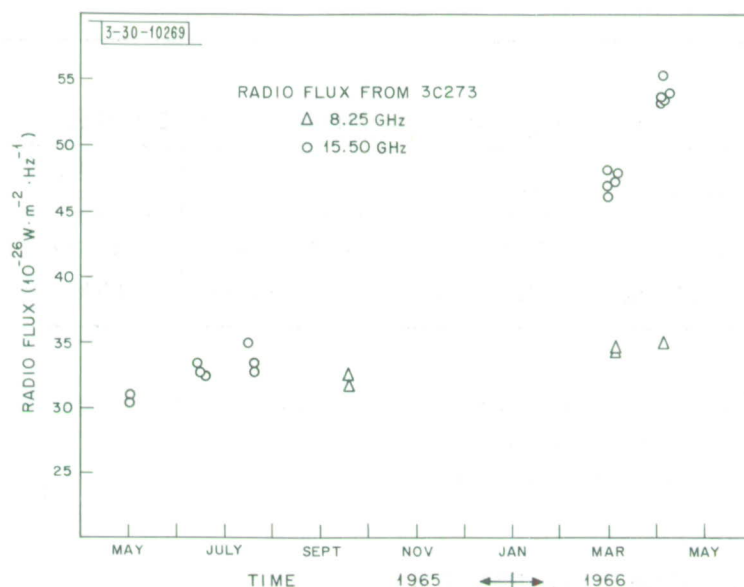


Fig. III-12. Increase in centimeter radiation received from quasi-stellar source 3C273.

On the other hand, observations at 15.5 GHz show a nonlinear increase in flux by a factor of almost two in the past year. On 6 April 1966, the flux at 8.25 GHz was 35.0 flux units,^{*} while at 15.50 GHz it was 54.5 units. Thus at that time, 3C273 has an upturned spectrum similar to 3C84 and 3C279.¹⁶ The flux from Virgo A has remained constant at both frequencies; 42.7 units at 8.25 GHz and 27.5 units at 15.5 GHz. Figure III-12 shows the time dependence of the radio emission at the two frequencies.

R. J. Allen
Prof. A. H. Barrett
(Research Laboratory
of Electronics, M.I.T.)

F. OBSERVATIONS OF HYDROGEN RECOMBINATION LINES

In April 1966, the Haystack radar receiving system was modified to permit radiometric observations of the hydrogen recombination line at 7.793 GHz. The modifications included mounting a Clavin feed next to the normal horn feed of the radar and adjusting the two local oscillators to appropriate frequencies. Doppler frequency shift caused by the motion of the Haystack site with respect to the local standard of rest was compensated by tuning the second local oscillator during observations. The parametric amplifiers were cooled by liquid N₂ to give a system temperature of approximately 200°K. The spectral line equipment normally used with the radiometer receivers was arranged to process the signal from the radar receiver.

Observations were made of the 92 α hydrogen line in emission in the Orion Nebula, Omega Nebula and W3. The frequency resolution was 100 kHz over a spectral range of 4 MHz. Table III-3 lists the measured temperatures and line widths for two of the sources. The parameters T_C , T_L , and $\Delta\nu_L$ refer to the increase in antenna temperature due to the continuum and line emission, and the half-power width of the line, respectively.

* 1 flux unit = $10^{-26} \text{ W m}^{-2} (\text{Hz})^{-1}$

TABLE III-3 TEMPERATURES AND LINEWIDTHS FOR TWO SOURCES			
Source	T_C	T_L	$\Delta\nu_L$
Orion Nebula	$21.1^\circ (\pm 0.6)$	$1.5^\circ (\pm 0.2)$	850 kHz (± 100)
Omega Nebula	$14.5^\circ (\pm 0.6)$	$0.95^\circ (\pm 0.1)$	1100 kHz (± 50)

The velocity of the hydrogen recombination line source in W3 is $-45 \text{ km/sec} \pm 2 \text{ km}$, the same as that of the strong OH-line source in W3. This coincidence in velocity space suggests a spatial association of the two emission regions.

M. L. Meeks
M. A. Gordon

G. HAYSTACK-MILLSTONE INTERFEROMETER

The Haystack 120-ft antenna and the Millstone 84-ft antenna have been used jointly as an interferometer in an attempt to obtain the positions and effective sizes of OH emission regions. The separation of 2257 feet between the two antennas produces a minimum fringe-lobe separation of 54 seconds of arc at 1665 MHz as illustrated in Fig. III-13. Phase measurements relative to a radio source of known position allow position measurements to about 20 seconds of arc if the phase is measured to within a radian. While instrumental phase changes and the accuracy of the baseline limit the precision of the absolute measurements, the measurements of position of one feature relative to another can be made with much higher precision, since the features are separated by only a few kilohertz.

A block diagram of the interferometer is shown in Fig. III-14. The radiometers are image-rejected, tunnel-diode amplifiers followed by mixers and 30-MHz IF amplifiers. A common LO signal is derived from oscillators phase-locked to the sum of a harmonic of 67 MHz and an

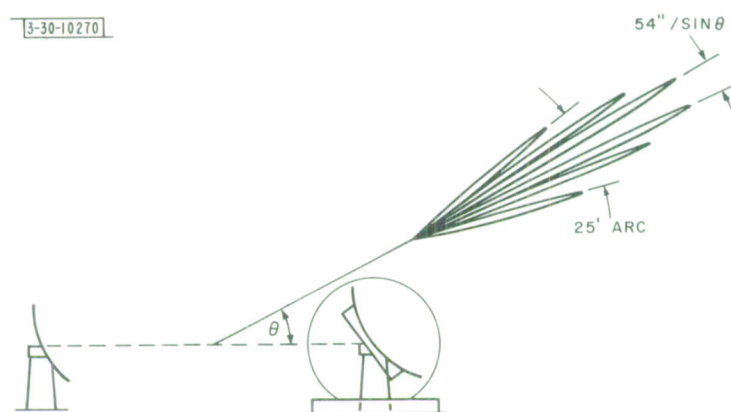


Fig. III-13. Lobe pattern for Haystack-Millstone interferometer at 1665 MHz.

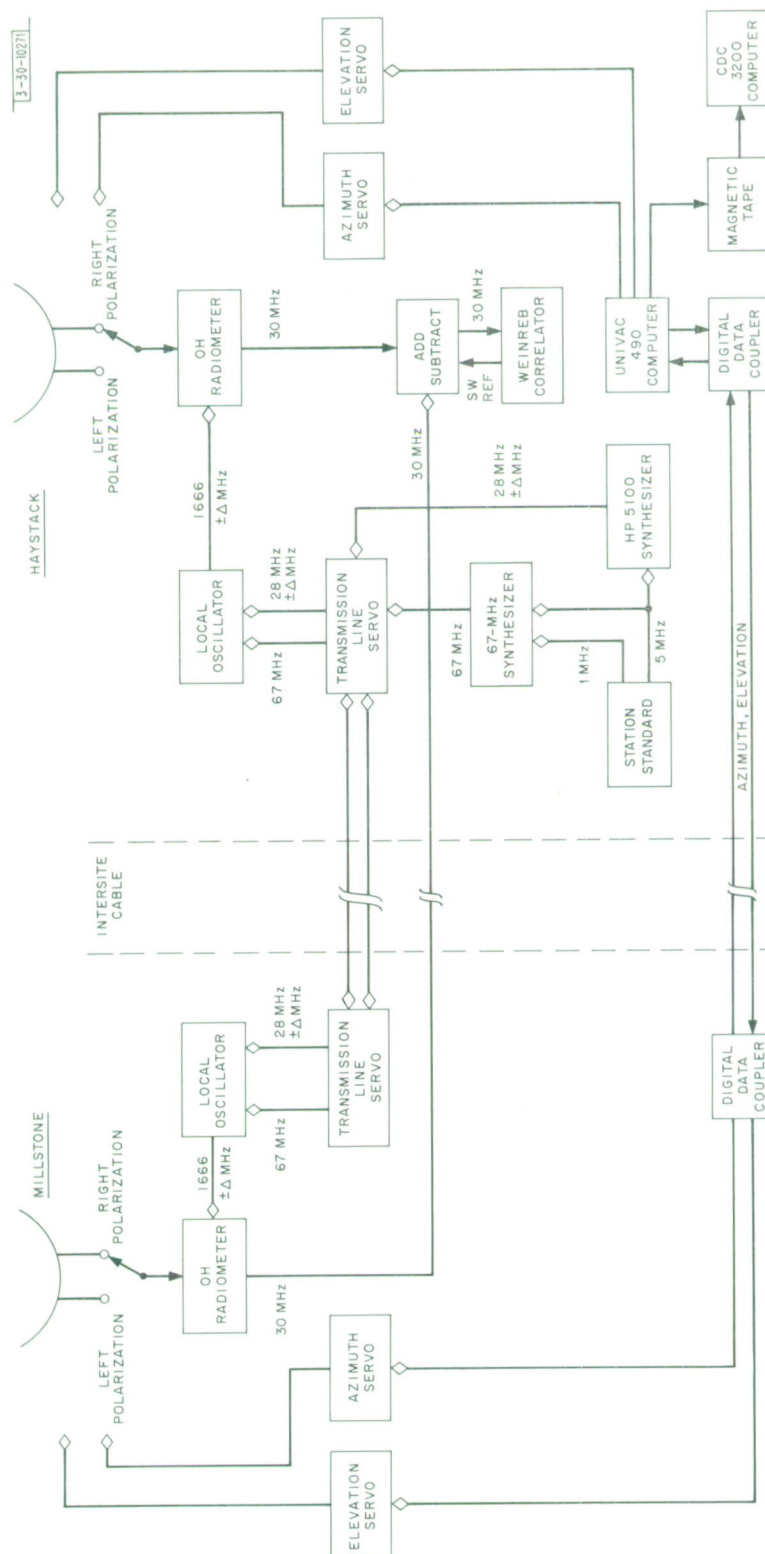


Fig. III-14. Haystack-Millstone interferometer.

Section III

adjustable frequency around 28 MHz. The phase shift of the 67 and 28 MHz signals caused by line-length changes is eliminated by a line servo system that maintains a constant electrical length along the line between radiometers. Typically, the line servo has to adjust for a length change of 6 feet between day and night temperatures.

The 30-MHz signals are alternately added and subtracted with a 200-μsec period. The autocorrelation functions for the clipped versions of the sum and difference signals are transferred from the output of a digital correlator to the Univac 490 computer. These autocorrelation functions together with antenna command coordinates are written onto magnetic tape. A post-real-time program then analyzes the data for fringe amplitude and phase information over the spectrum.

A reference phase is computed every 200 μsec from the relation

$$\Phi_{\text{ref}} = \frac{\omega_0}{c} [D \sin E_H \sin E_{s,t} + D \cos E_H \cos E_s (A_{s,t} - A_H) - d \cos E_{s,t}]$$

Here D , E_H , A_H , and d are parameters of the baseline and $A_{s,t}$, $E_{s,t}$ are the refraction-corrected azimuth and elevation of a reference position in the sky.

Multiplication of the difference of autocorrelation functions of the added and subtracted signals by the sine and cosine of the reference phase allows a least-squares estimate of the fringe amplitude and phase to be made.

Plots of the un-normalized fringe amplitude and phase are shown in Figs. III-15 and III-16 as typical examples of the data output.

A. E. E. Rogers
(Research Laboratory
of Electronics, M.I.T.)
G. M. Hyde

H. SPECTRUM MEASUREMENTS NEAR 1-cm WAVELENGTH USING THE 28-ft MILLIMETER-WAVE ANTENNA*

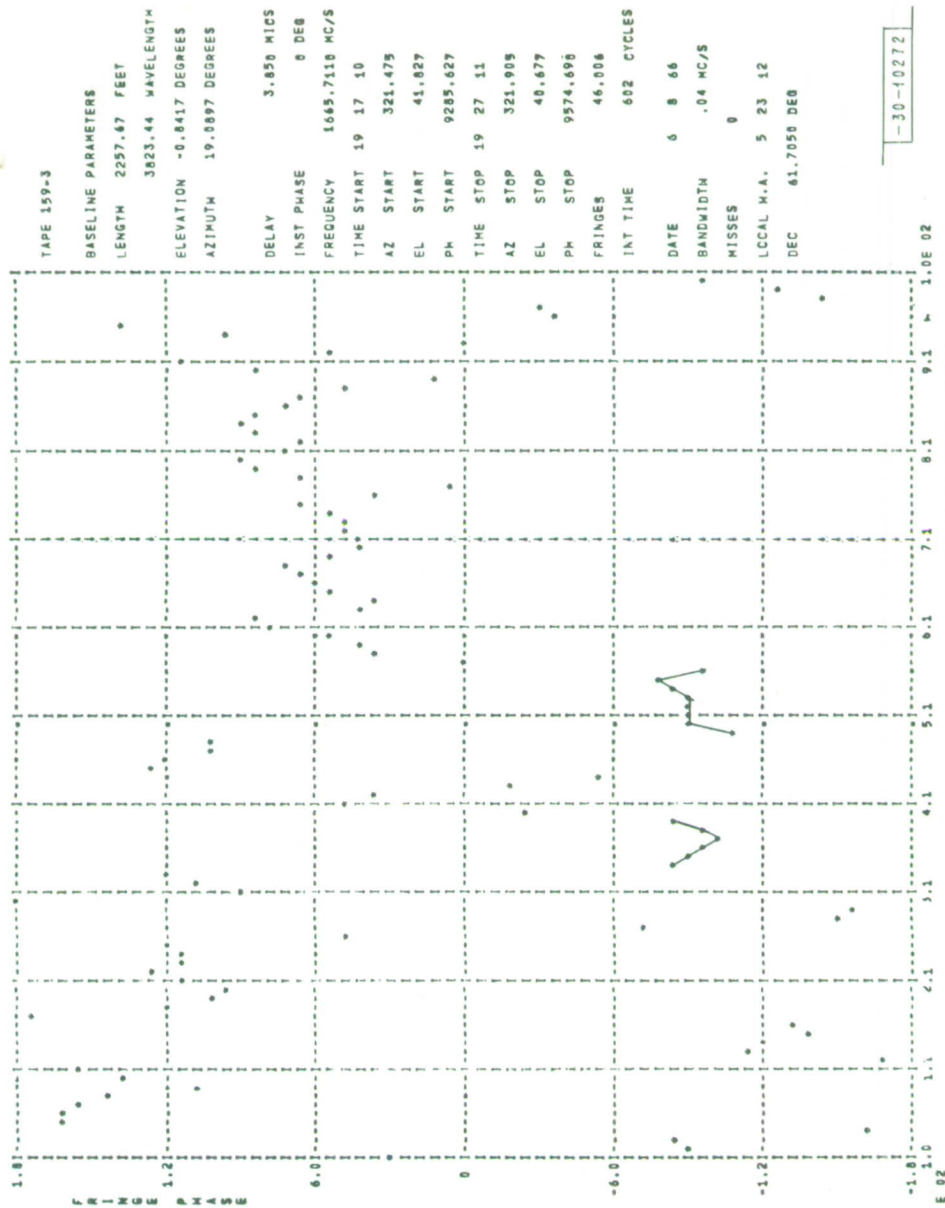
1. Introduction

Several research programs have been conducted since April 1964 using the 28-ft millimeter antenna* in conjunction with a five-channel microwave radiometer developed by the M.I.T. Research Laboratory of Electronics (Staelin,¹⁷ Staelin and Barrett¹⁸). A block diagram of the radiometer is shown in Fig. III-17. The major programs include spectrum studies of the following: the planet Venus, the planet Jupiter, the moon, the sun, and the terrestrial atmosphere.

2. The Planet Venus

Venus was observed on 15 days from June to August 1964 at wavelengths of 0.92, 1.02, 1.18, 1.28, 1.37, and 1.42 cm and was observed on 14 days from January to March 1966 at wavelengths of 1.18, 1.28, 1.35, 1.43, and 1.58 cm. The planetary spectrum was determined by measuring the planet-moon ratio and then correcting the ratio for the measured antenna pattern. An extensive set of atmospheric absorption measurements was used to correct the observed spectra for atmospheric absorption.

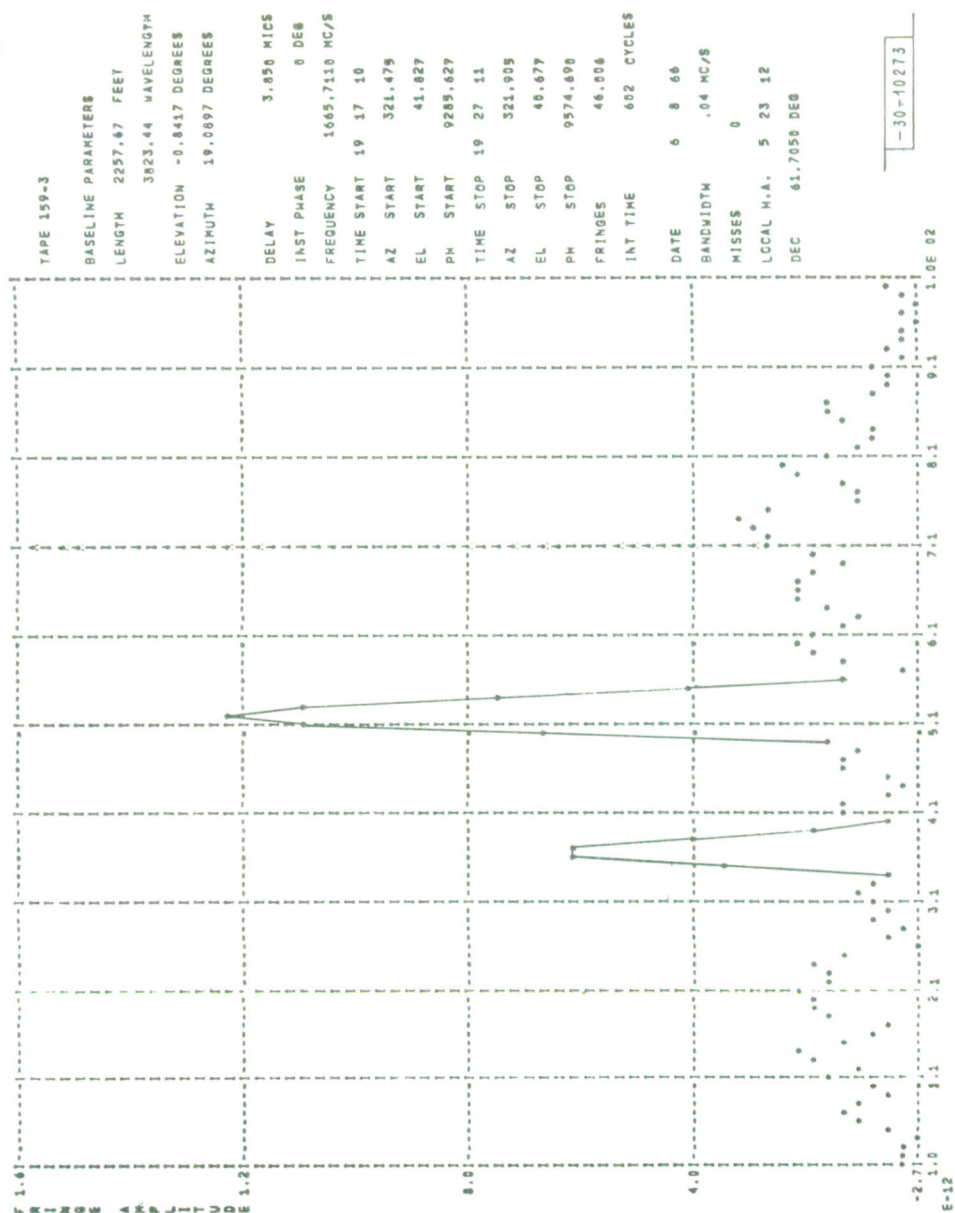
* See Sec. VI-B and Appendix B for description.



Section III

Fig. III-15. Un-normalized fringe amplitude, W3 OH-emission source, right circular polarization. Points on emission features are connected with straight lines.

Section III



-30-10273

Fig. III-16. Fringe phase, W3 OH-emission source, right circular polarization. Points representing phases of two emission features in previous figure are connected with straight lines.

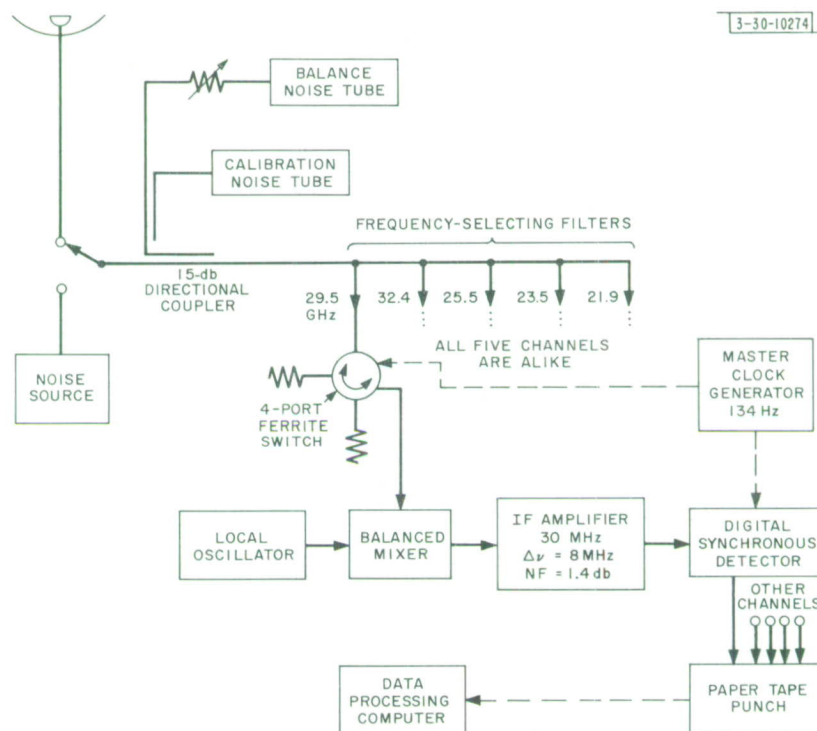


Fig. III-17. Five-channel microwave radiometer.

This region of the microwave spectrum of Venus is important because it includes a rather sharp transition, the shape of which may distinguish various atmospheric models. Certain atmospheric models that have been proposed incorporate molecules such as H_2O which show absorption at these wavelengths (Barrett and Staelin¹⁹). The first series of observations indicated the possible presence of a time-varying absorption feature near 1.35-cm wavelength, a resonant frequency of water vapor (Staelin and Barrett¹⁸).

More recent observations of 1966 were made with an improved antenna feed and radiometer. These observations, not fully analyzed, presently indicate no spectral feature at 1.35-cm wavelength (Staelin and Neal²⁰).

3. The Planet Jupiter

Jupiter was observed on five days from February to March 1966, using the same equipment and procedures as for the simultaneous Venus observing program. The preliminary average spectrum shows no sharp feature near 1.35-cm wavelength (Staelin and Neal²⁰). Resonance features of NH_3 may also occur in this wavelength region, and will be sought later.

4. The Moon

The moon was observed principally during the summer of 1964 (Moran, Barrett and Staelin;²¹ Moran²²). Scans through the center of the moon were used to determine the lunar brightness temperature at the center of the lunar disk as a function of phase. By measuring the asymmetry

Section III

TABLE III-4 DETERMINATION OF LUNAR HARMONIC COMPONENTS						
Frequency (GHz)	Assumed T_o (°K)	T_1 (°K)	θ_1 (deg)	T_2 (°K)	θ_2 (deg)	T_3 (°K)
21.9	217	21 ± 2	41 ± 5	5 ± 1	38 ± 5	1
23.5	217	22	48	6	31	1
25.5	217	25	42	6	40	1
32.4	217	29	41	8	38	1

in the lunar brightness temperature as a function of phase, the harmonic components were determined. The results are summarized in Table III-4, where the lunar brightness temperature T_B is given as a function of lunar phase ϕ by

$$T_B = \sum_{i=0}^{\infty} T_i \cos(i\phi - \theta_i) \quad .$$

Measurements of the difference in temperature observed when the antenna feed is linearly polarized along and across the direction of scan as a function of angular offset from the center, as shown in Fig. III-18, are consistent with a lunar dielectric constant of 1.5 ± 0.1 for a smooth lunar surface, and 1.7 for a surface with an RMS slope of 15° .

5. The Terrestrial Atmosphere

Three major series of atmospheric observations have been made: June-August 1964, June-August 1965, and January-March 1966. The wavelengths observed were 0.92, 1.02, 1.18, 1.28, and 1.37 cm; 0.92, 1.02, 1.28, 1.35 and 1.37 cm; 1.18, 1.28, 1.35, 1.43 and 1.58 cm, respectively. The observations consisted principally of atmospheric absorption measurements made by means

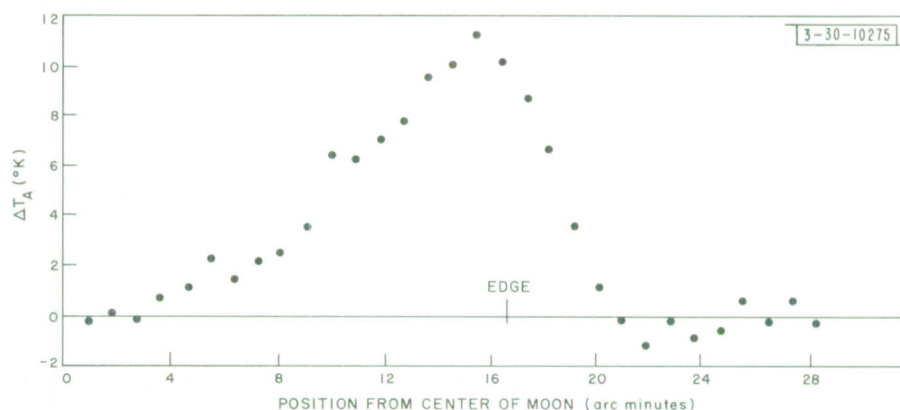
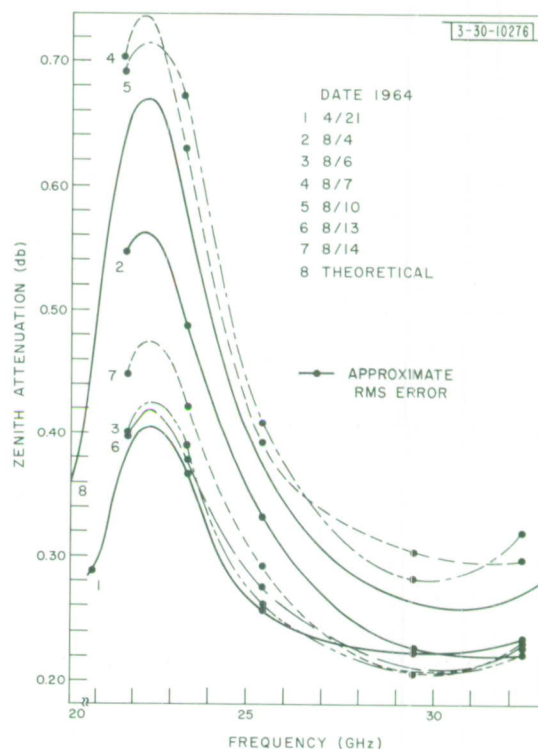


Fig. III-18. Polarization dependence of lunar brightness temperature at 35 GHz.

Fig. III-19. Absorption spectra of terrestrial atmosphere.



of solar-extinction observations. Over 40 of these were accompanied by a radiosonde launched either from Hanscom Field or from the M.I.T. campus in Cambridge. The observed spectra (Staelin,²³ Gant and Staelin²⁴) all exhibit the 1.35-cm water vapor resonance, which varied in amplitude and shape depending upon the water vapor profile of the atmosphere. Figure III-19 shows typical observed spectra.

Prof. D. H. Staelin	} Research Laboratory of Electronics, M. I. T.
Prof. A. H. Barrett	
N. E. Gant	
J. J. Moran	
J. J. G. McCue	
J. R. Cogdell	

REFERENCES

1. J.C. Henry, Master's Thesis, M.I.T. (August 1965).
2. Radio Physics and Astronomy Report, Lincoln Laboratory, M.I.T. (1965:1), pp. 23-28, DDC 629923.
3. D. Downes, A. Maxwell, and M.L. Meeks, *Nature* 208, 1189 (1965).
4. Ref. 2, p. 40.
5. C. Lanczos, *Applied Analysis* (Prentice Hall, N.J., 1956), pp. 331-337.
6. R.N. Bracewell, *Australian J. Phys.* 9, 297 (1956).
7. A. Maxwell and D. Downes, *Nature* 204, 865 (1964).
8. S. Weinreb, Ph.D. Thesis, M.I.T. (1963). Printed as Technical Report 412, Research Laboratory of Electronics, M.I.T. (30 August 1963).
9. S. Weinreb, M.L. Meeks, J.C. Carter, A.H. Barrett and A.E.E. Rogers, *Nature* 208, 440 (1965).
10. A.H. Barrett and A.E.E. Rogers, *Nature* 210, 188 (1966).
11. R.D. Davies, G. de Jager and G.L. Verschuur, *Nature* 209, 974 (1966).
12. M. Born and E. Wolf, *Principles of Optics* (Pergamon Press, N.Y., 1959), p. 550.
13. A. Sotiropoulos and J. Ruze, "Haystack Calibration Antenna," Technical Report 367, Lincoln Laboratory, M.I.T. (15 December 1964), DDC 611436.
14. J.W.M. Baars, P.C. Mezger, H. Wendker, *Astrophys. J.* 142, 122 (1965).
15. W.A. Dent, *Science* 148, 1458 (1965).
16. W.A. Dent and F.T. Haddock, *Nature* 205, 487 (1965).
17. D.H. Staelin, ScD. Thesis, Department of Electronic Engineering, M.I.T. (January 1965).
18. D.H. Staelin and A.H. Barrett, *Astrophys. J.* 144, 1, 352 (1966).
19. A.H. Barrett and D.H. Staelin, *Space Sci. Rev.* 3, 109 (1964).
20. D.H. Staelin and R.W. Neal, private communication.
21. J.M. Moran, Jr., A.H. Barrett and D.H. Staelin, Quarterly Progress Report No. 81, Research Laboratory of Electronics, M.I.T. (1966), p. 21.
22. J.M. Moran, Jr., S.M. Thesis, Department of Electronic Engineering, M.I.T. (June 1965).
23. D.H. Staelin, *J. Geophys. Research* 71 (15 June 1966).
24. N.E. Gant, and D.H. Staelin, Quarterly Progress Report No. 81, Research Laboratory of Electronics, M.I.T. (1966), p. 12.

IV. ATMOSPHERIC RESEARCH

A. INCOHERENT IONOSPHERE BACKSCATTER

In the last radio physics and astronomy report¹ we described in some detail the program of incoherent backscatter observations of the earth's ionosphere. No major changes have been made to the equipment nor to the methods of data gathering described in that report, though some changes have been made in the methods of data reduction.

Observations using the 440-MHz radar have continued throughout 1966 for two periods of 24 hours each, every month. Measurements are also made with the 1295-MHz steerable radar once a month for a 12-hour period.

The backlog of data reduction continues to be the most pressing problem. A second data technician has been acquired to assist with the hand analysis. In addition, some computer program changes have been made which should eliminate one tedious part of the hand analysis. These improvements are, however, too recent to have yet seriously affected the situation. At present the complete analysis of the 1964 results is nearly finished. Partial analysis (computer reduction) of the 1965-1966 results has been carried out, but much long and tedious hand analysis remains. The remedy ultimately lies in providing the sophisticated computer programs required to permit much greater dependence upon machine processing.

J. V. Evans R. F. Julian
W. A. Reid R. A. Brockelman

B. LOWER ATMOSPHERIC STUDIES AT X-BAND

A program to investigate the effects of the lower atmosphere on earth to space propagation paths was initiated in support of the Laboratory's Space Communications Program. The initial area of investigation is in the effects of the atmosphere on X-band, line-of-sight systems. In this frequency band, the predominant propagation problems are caused by rain: signal attenuation, enhanced scatter interference from ground sources, and increased receiver noise. The current X-band propagation study is directed primarily toward the analysis of these effects.

1. Scattering by Rain and Clouds

The microwave rain scattering phenomenon has been known for many years. Since World War II, this phenomenon has been used by radio meteorologists for storm detection and study. The increased use of microwave, line-of-sight paths for reliable communications has revived a study of the details of this phenomenon. The communication systems engineer now needs statistics of the rain effects: attenuation, bistatic scattering cross sections, and increased sky temperature. Each of these scattering effects may be computed by using simplifying assumptions about the rain drops, their size, shape, dielectric properties, and numbers, about the scattering process, by neglecting cooperative effects between individual drops, and by invoking single scattering theory to describe the overall effects of an ensemble of drops. With these assumptions, computations of the attenuation and backscattering cross sections have been made

Section IV

for model, homogeneous rain-drop distributions (Ryde and Ryde²; Gunn and East³; Oguchi^{4,5}; Medhurst⁶). Recent computations of bistatic scattering cross sections have been made by Deirmendjian⁷ and of sky temperature change by Hogg and Semplak.⁸

The computations and, in some cases, experimental data indicate the order of magnitude of the scattering effects. The attenuation, sky temperature, and scattering statistics depend both upon the per-unit-volume scattering statistics and on the way these statistics are organized in rain showers and storms. Weather radar data have been used to study the details of the large scale storm processes. These data show that the rain storm structure varies from storm to storm and location to location. Statistical analysis of rain storm data is, however, not available for the estimation of the rain scattering effects of interest. The only crude statistical estimates available of rain attenuation (Bussey⁹; Ugal and Kaneda¹⁰) were made from measurements of rain rate taken at a point on the surface.

The program described here for studying rain-scattering effects consists of making a detailed analysis of both the microscale and macroscale scattering effects of rain. The microscale or per-unit-volume scattering statistics are being studied by using a large sample of measured rain-drop distributions and by experimentally checking the results of scatter computations on artificial rain-drop distributions. The macroscale scattering analysis consists of a study of the details of storm organization through comparisons of measured sky temperature with computations based on weather radar measurements. The goal of these studies is a method by which climatological rain data, such as rain gauge statistics and weather radar statistics can be converted into attenuation, sky temperature, and interference statistics.

2. Microscale Studies

The interpretation of weather radar data in terms of rain or scattering parameters requires a detailed knowledge of the integrated scattering and rain parameters for many different drop-size distributions. To provide a statistical transformation from weather radar measurements of reflectivity to rain rate, liquid water content, attenuation coefficient and sky temperature, computations were made for a large sample of drop-size measurements by means of the filter paper method at M.I.T., in Cambridge.* The rain drops were assumed to be spherical, to be all at a constant drop temperature, and to have a parent drop-size distribution given by the measured drop-size distribution. The scattering effects were computed using Mie Theory as described by Van de Hulst.¹¹ For these computations, the dielectric constant for water was taken from Kerr¹² (Table 8.8, page 675). The rain rate was computed using the terminal velocity data of Gunn and Kinzer.¹³

The effective reflectivity factor (Z_{eff}) as defined by Eq. (1) is used to characterize the backscattering of an ensemble of scatterers.

$$Z_{\text{eff}} = \frac{\beta \lambda^4}{\pi^5 |k|^2} \quad \text{mm}^6/\text{m}^3 \quad (1)$$

β = backscatter cross section per unit volume in millimeters squared per cubic meter.

* The sample consists of 338 drop-size measurements made over a two-year period by the M.I.T. Weather Radar Research Facility and it represents many different types of storms.

λ = wavelength in millimeters

$$k = \frac{m^2 - 1}{m^2 + 2}$$

m = complex refractive index of water.

Figure IV-1 shows the relation between rain rate and Z_{eff} at 2.8 GHz obtained from Eq. (1) and the observed drop-size distributions. This figure provides the connection between values of Z_{eff} obtained from weather radar measurements and the usual rain parameter, rain rate. The line labeled

$$Z_{\text{eff}} = 200R^{1.6}, \quad \text{where } R = \text{rain rate in millimeters per hour,} \quad (2)$$

is normally used by radar meteorologists to provide this connection. The Laws and Parsons model¹⁴ represents the averages of drop-size measurements made over a three-year period in the Washington, D.C. area. This model is used for most of the attenuation computations referenced above. The spread in data points is caused in part by the natural variability of parent drop-size distributions that occur in the many different storm types represented by the New England storm sample. A second cause in the spread in data points is instrumental, being mostly due to the use of a limited sample volume. The relative importance of the instrumental uncertainty is presently unknown and is the subject of continuing investigation.

The attenuation coefficient in decibels per kilometer as a function of rain rate and of reflectivity is presented in Figs. IV-2 and IV-3. The spread in data points about the Laws and Parsons line is smallest at low rain rates or at high reflectivities. From this, it is seen that for the very low rain rates, a measurement of rainfall rate not dependent upon weather radar data is desirable while at the highest rainfall rates, weather radar data provides a better measurement of attenuation than does a method based on rainfall rate data. For this data sample, less than a factor of two uncertainty in the attenuation coefficient is evident for log Z values greater than 4.0 or rain rates above 10 to 15 mm/hr.

The sky temperature for a homogeneous, constant temperature slab volume of rain drops is given by

$$\begin{aligned} T &= \int_0^d T_D \beta_{\text{ext}} \exp \left[- \int_0^s \beta_{\text{ext}} ds \right] ds \\ &= T_D (1 - e^{-\tau}) \end{aligned}$$

$$\text{where } \tau = \int_0^d \beta_{\text{ext}} ds = \text{optical depth} = \frac{A}{4.343}$$

A = total attenuation along path

β_{ext} = extinction cross section per unit volume

T_D = constant drop temperature

d = distance across slab volume

s = distance along the path.

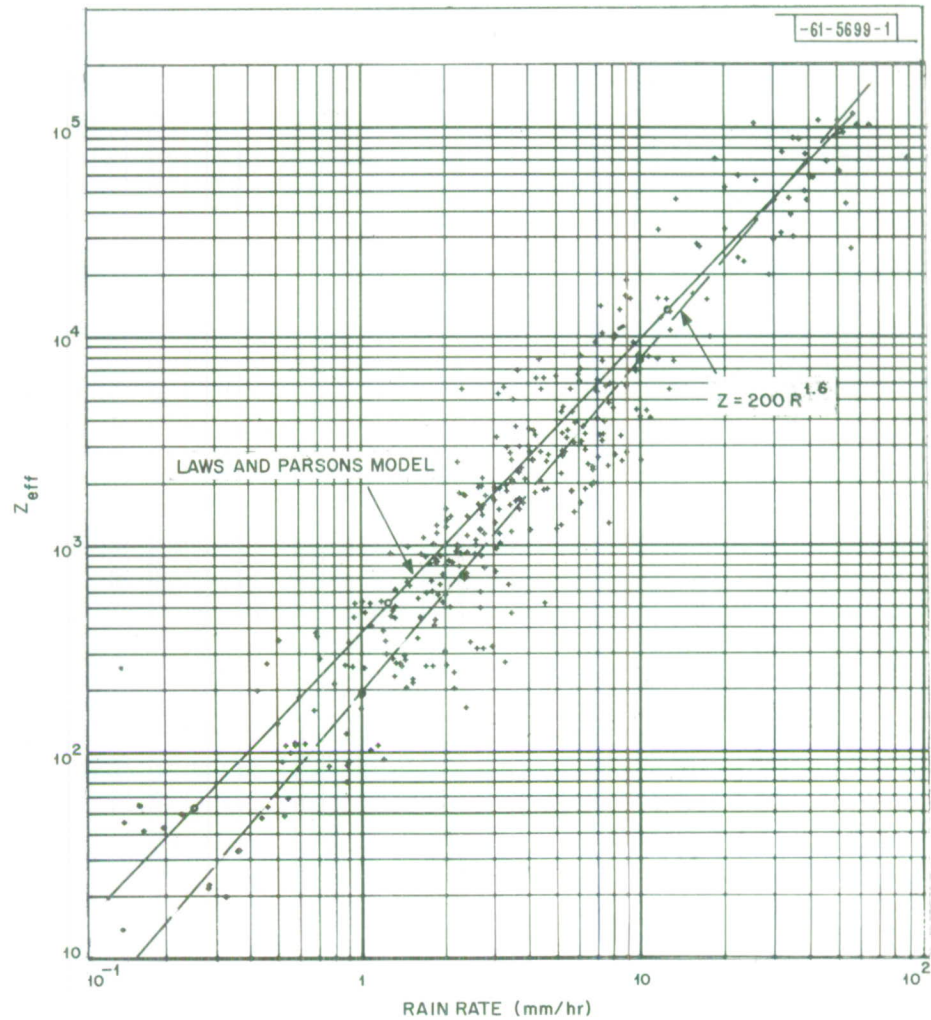


Fig. IV-1. Reflectivity vs rain rate for New England storm sample.

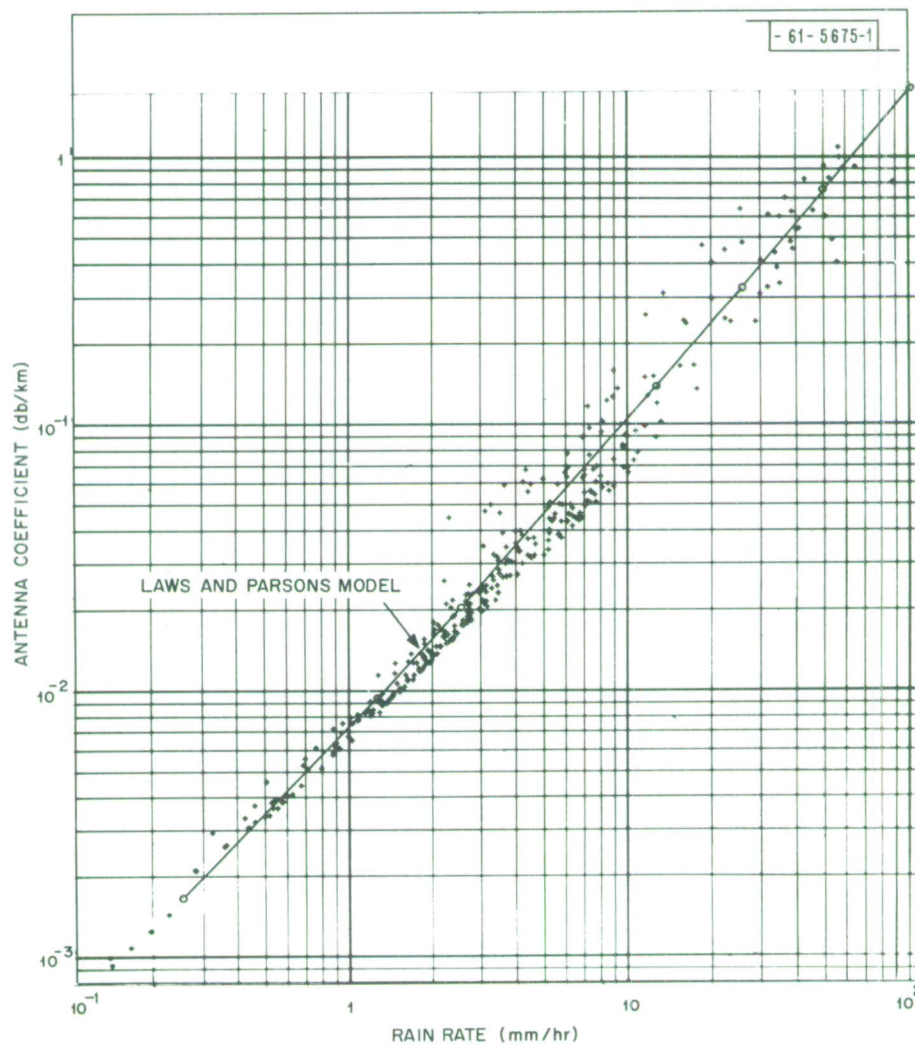


Fig. IV-2. 8.0-GHz attenuation coefficient vs rain rate for New England storm sample.

Section IV

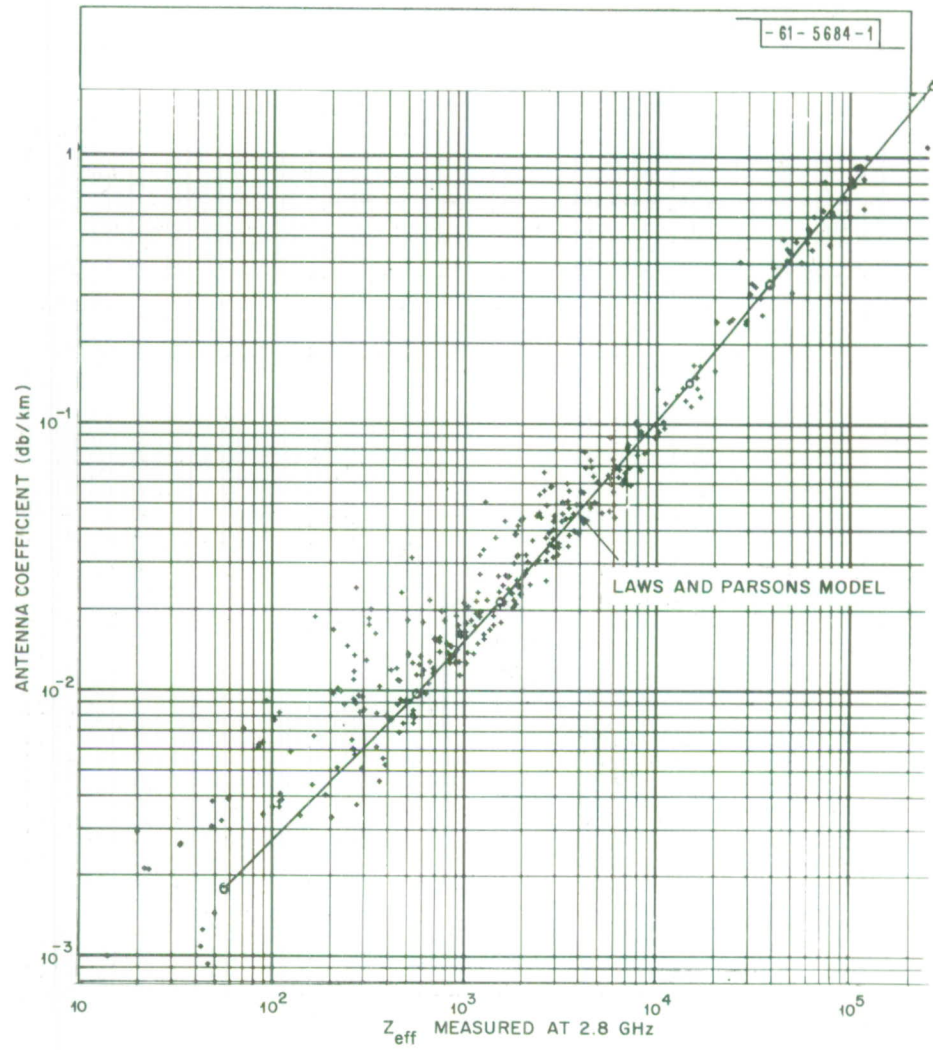


Fig. IV-3. 8.0-GHz attenuation coefficient vs reflectivity for New England storm sample.

This integral as given by Hogg and Semplak⁸ represents a low-order scattering solution to the radiative transfer equation. Sky temperature computations for an isolated slab at 0.0° C are given in Figs. IV-4 and IV-5. These results apply reasonably well to drop temperatures that may occur in New England because, at 8.0 GHz, the attenuation coefficient changes only slightly with temperature and T_D varies by, at most, ten percent.

An experimental check is being sought for the above calculations by computing and measuring the attenuation and phase shift caused by an artificial water-drop distribution existing over a distance of 15 feet in the center of a 1000-ft line-of-sight propagation path. Facilities are being provided for measuring both the instantaneous and average values of attenuation and phase shift for a time-stationary parent water-drop distribution. The experimental check is necessary to answer some of the questions raised by the lack of experimental verification of scattering computations made for longer path lengths as reported by Medhurst.⁶

The final part of the microscale investigation is concerned with the bistatic scattering cross sections per unit volume. The bistatic scattering cross section is a function of both the polarization of the incident radiation and the scattering angle. The polarization dependence can be investigated by considering two linear, orthogonal polarizations, one in the plane of scattering and the other perpendicular to this plane. For spheres, using this polarization representation, there are no cross-polarization terms generated by single scattering and the result is a function only of the scattering angle, the angle between the direction of propagation of the incident and the scattered radiation. Two bistatic scattering cross sections are sufficient to describe the scattering process, one for polarization in the plane of scattering, $\beta_2(\theta)$ and the other perpendicular to this plane $\beta_1(\theta)$. Figure IV-6 shows the normalized bistatic scattering cross sections per unit volume as a function of scattering angle for the Laws and Parsons model.¹⁴ In this plot,

$$p_1(\theta) = \frac{\beta_1(\theta)}{\beta_{\text{scat}}} \quad (4)$$

$$p_2(\theta) = \frac{\beta_2(\theta)}{\beta_{\text{scat}}} \quad (5)$$

β_1, β_2 = bistatic scattering cross section per unit volume

$$\beta_{\text{scat}} = \int_0^\pi [\beta_1(\theta) + \beta_2(\theta)] \sin \theta \, d\theta \quad (6)$$

= total scattering cross section per unit volume.

The lines labeled Rayleigh scatterer depict the results for Rayleigh scattering where the phase functions $p_1(\theta)$, $p_2(\theta)$ are given by

$$p_1(\theta) = 3/2 \quad (7)$$

$$p_2(\theta) = 3/2 \cos^2 \theta \quad (8)$$

A measure of the departure of the bistatic scattering cross sections for rain at 8 GHz from those for Rayleigh scatterers is given by the ratio of $p_1(0^\circ)$ to $p_1(180^\circ)$ or of the forward-to-backscattered energy. Figure IV-7 gives this ratio as a function of reflectivity. A second

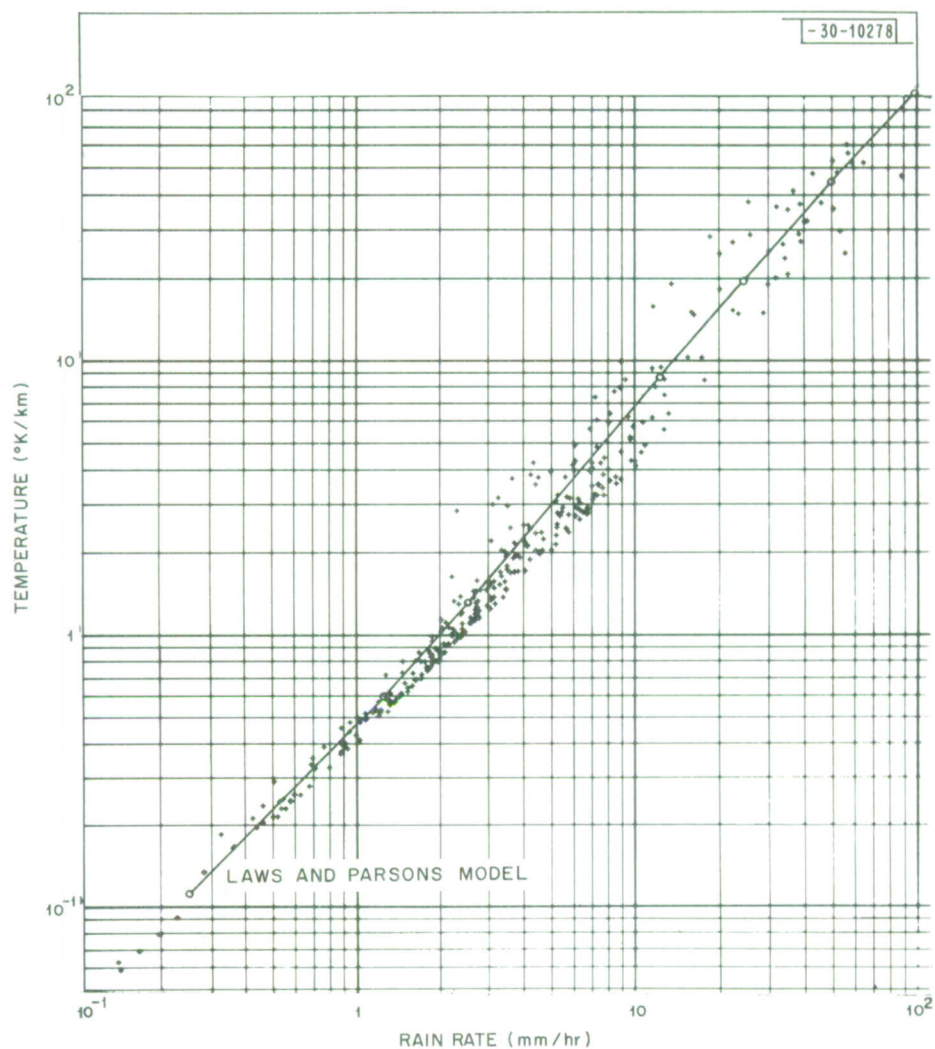


Fig. IV-4. Antenna temperature at 8.0 GHz vs rain rate for a homogeneous, 1.0-km-thick rain slab.

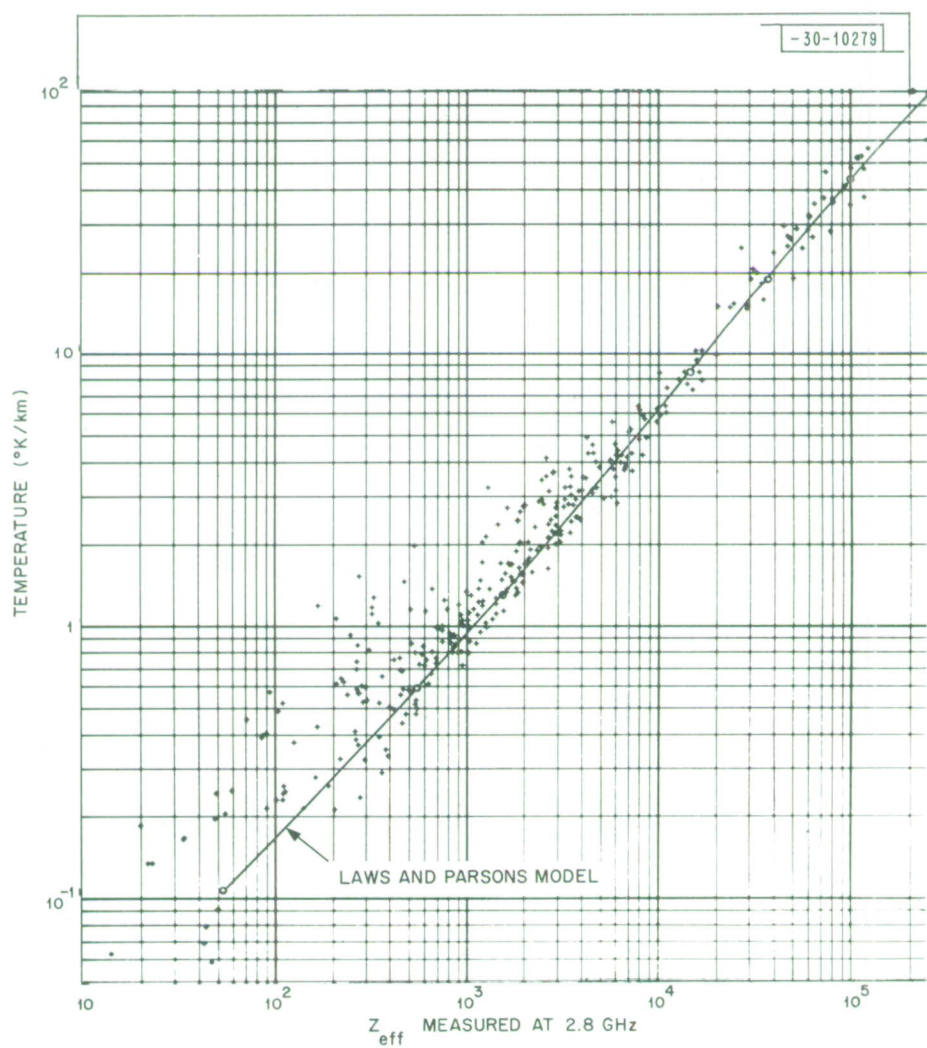


Fig. IV-5. Antenna temperature at 8.0 GHz vs reflectivity for a homogeneous, 1.0-km-thick rain slab.

Section IV

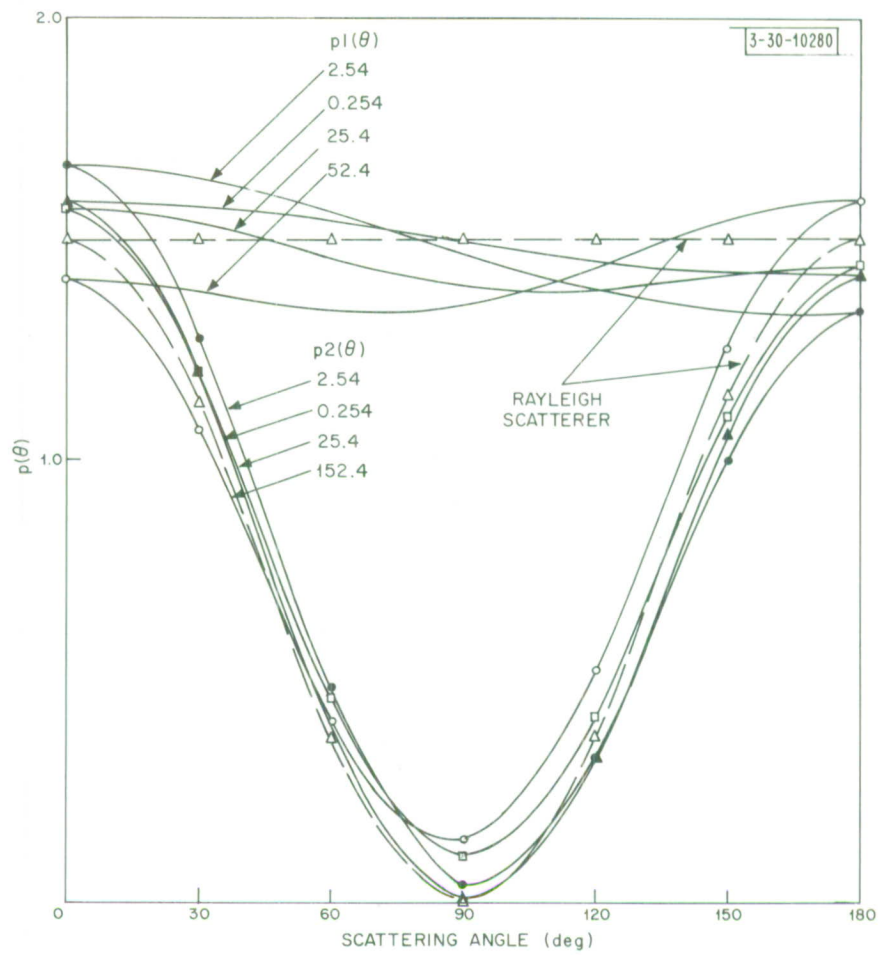


Fig. IV-6. Normalized bistatic scattering cross sections at 8.0 GHz vs scattering angle for Laws and Parsons model data.

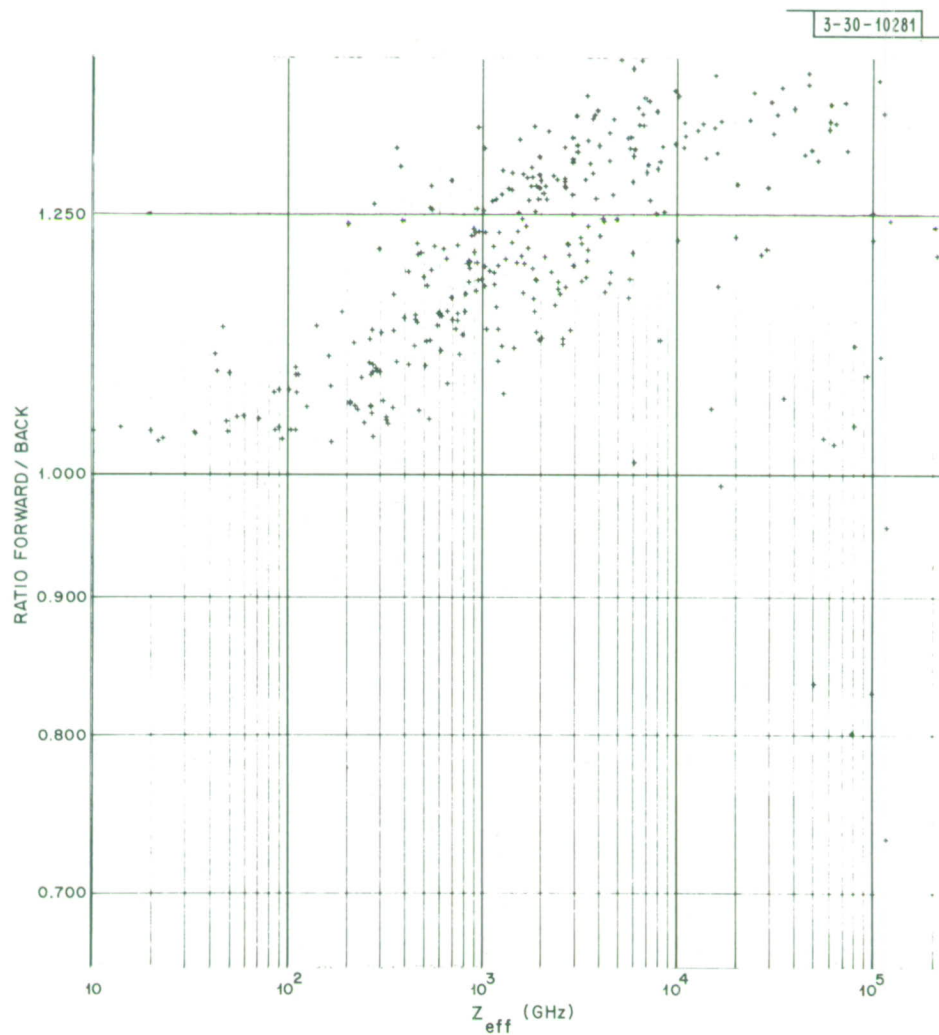


Fig. IV-7. Ratio of forward-to-backscattering cross section at 8.0 GHz vs reflectivity for New England storm sample.

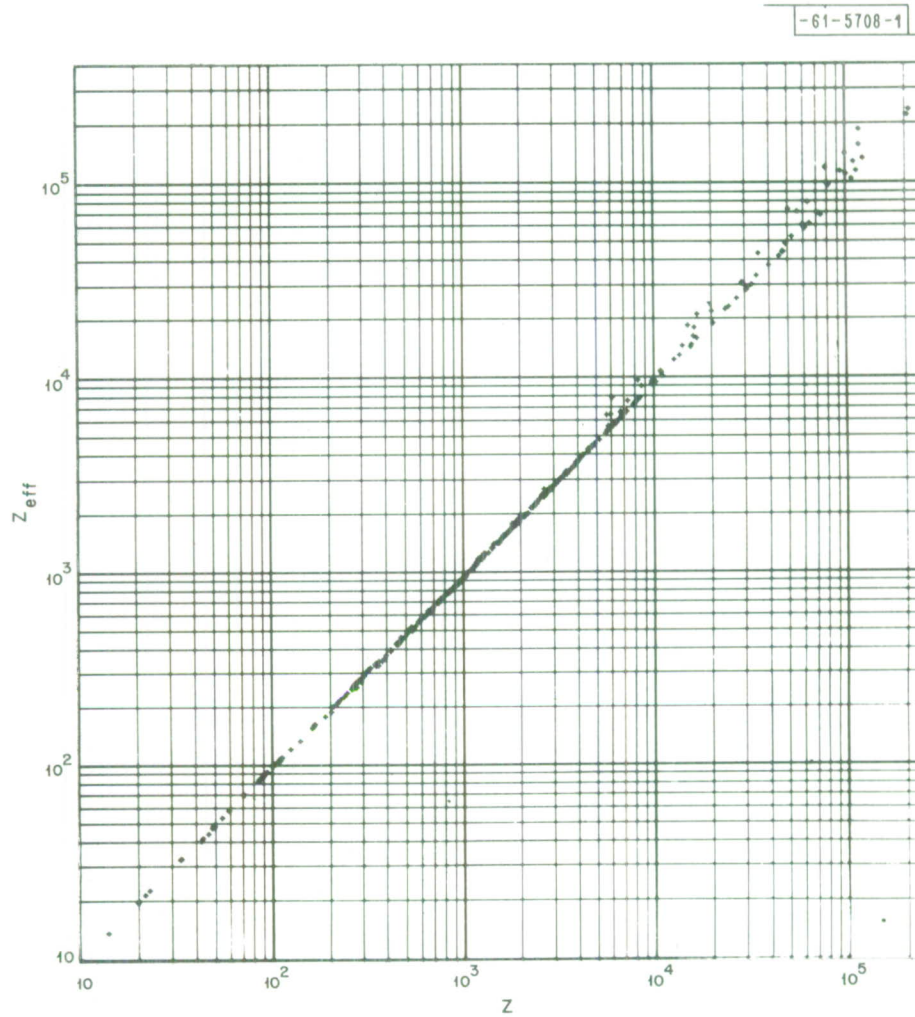


Fig. IV-8. Comparison of reflectivity calculated for 8.0 GHz using Mie theory with values calculated using Rayleigh theory.

measure is given by the departure of the Z effective from Z as given in Fig. IV-8. The quantity Z is found by substituting in Eq. (1) the backscatter cross section calculated for an ensemble of rain drops using Rayleigh theory. The data show that, for scattering, an ensemble of rain drops behaves as an ensemble of Rayleigh scatterers, except at the highest value of reflectivity. Rayleigh scattering theory, however, cannot be used to compute attenuation or sky temperature at 8 GHz.

3. Macroscale Studies

The microscale studies described above are oriented toward providing a means to interpret weather radar data with the least possible uncertainty due to rain storm types and the location of the scattering volume in the storm. The macroscale study is directed at using weather radar measurements of storm structure to compute attenuation, sky temperature, and composite bistatic scattering cross-section statistics. The method used to establish the validity of these computations is to make simultaneous measurements of Z_{eff} and sky temperature, using the 10-cm weather radar operated by the M.I.T. Weather Radar Research Facility at Cambridge and the X-band radiometer facility at Haystack.

The mode of operation is to observe rain storms at a distance from the Haystack site. Azimuth scans are taken with Haystack through a rain storm at a fixed elevation angle. Under these conditions, the change in sky temperature is due to the emission from rain and clouds and to the changes in the energy emitted by the surface of the earth and collected by the antenna side lobes. The contribution of the ground and clouds represents uncertainties in the measurements because both the side-lobe ground structure and the cloud structure are not readily measurable. For operation at elevation angles between 0.5 and 2.0 degrees, measurements of the ground contribution show less than a 2.0° K fluctuation after correction using previously measured data for each azimuth. The uncertainties in measurement due to clouds is related to the uncertainty in the integrated liquid water content of the clouds along the antenna beam. For clouds at 0.0°C, the sky temperature for an isolated 1.0-km-thick cloud is given by

$$T = 4.0W \text{ degrees Kelvin} \quad (9)$$

where

W = liquid water content in grams per cubic meter.

The cloud error can be large, being as much as 20.0° K for a large, nonraining cumulus cloud. These errors far exceed the instrument errors caused by calibration uncertainties and the short, 0.3-second integration time.

The results of a measurement made on 10 August 1965 are given in Figs. IV-9 through IV-11. Figure IV-9 is a weather radar map which shows a section of squall line visible both to the M.I.T. SCR-645B, 2.8 GHz weather radar and Haystack. The showers in the wedge bounded by 60°, 90° and 1.0° elevation horizon for Haystack are numbered 1 to 8. The horizon was chosen as the distance at which the 1° elevation ray would reach 5.0 km height. Per-unit volume reflectivities computed from weather radar cross-section data are shown in Fig. IV-10 as reflectivity contours. The figure also includes a reflectivity contour table which gives the maximum and minimum values of reflectivity which the volumes between successive levels, as described by the outer contours, can have.

Section IV

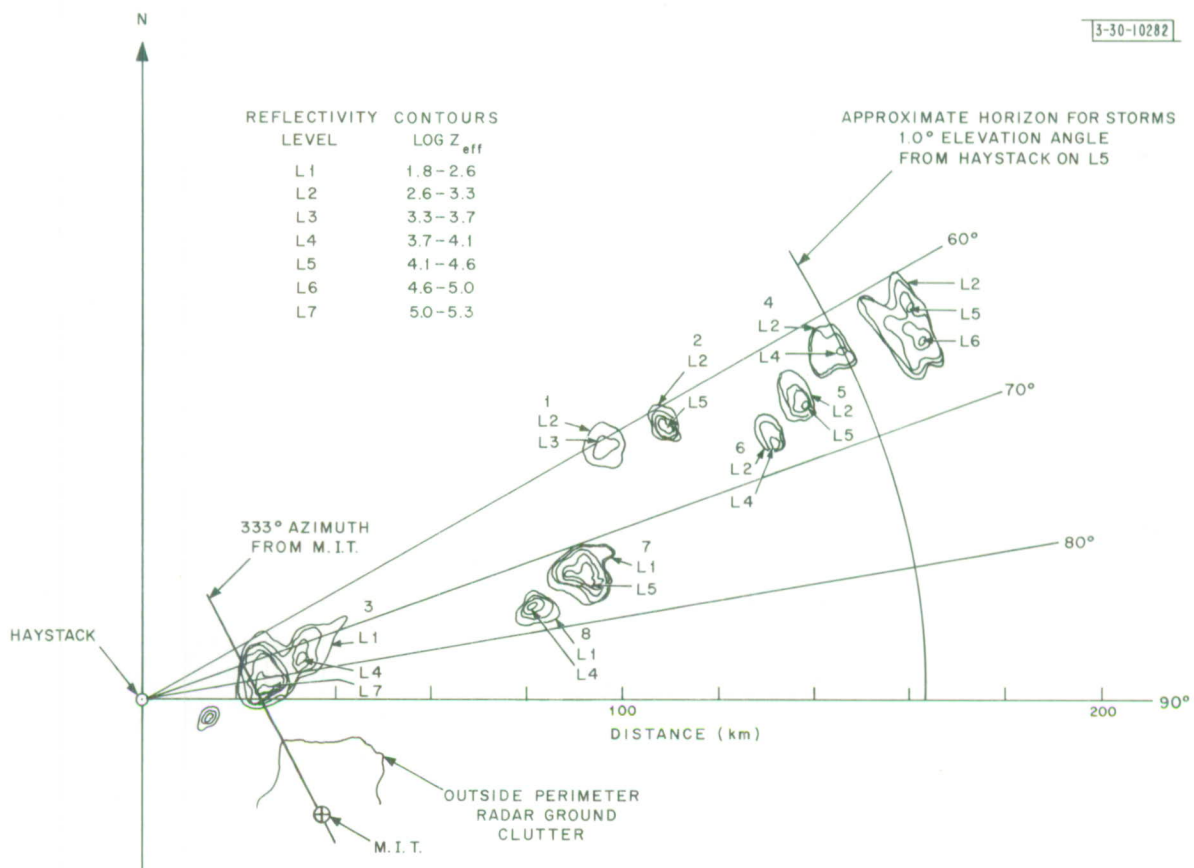


Fig. IV-9. Weather radar map for section of squall line east of the Haystack site.

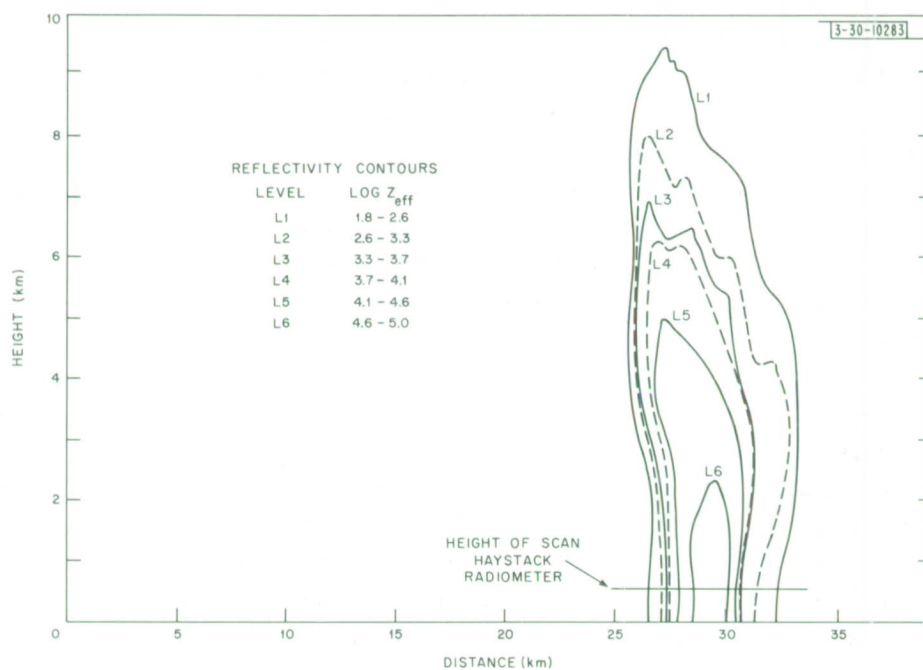


Fig. IV-10. Reflectivity cross section through section of squall line east of Haystack site.

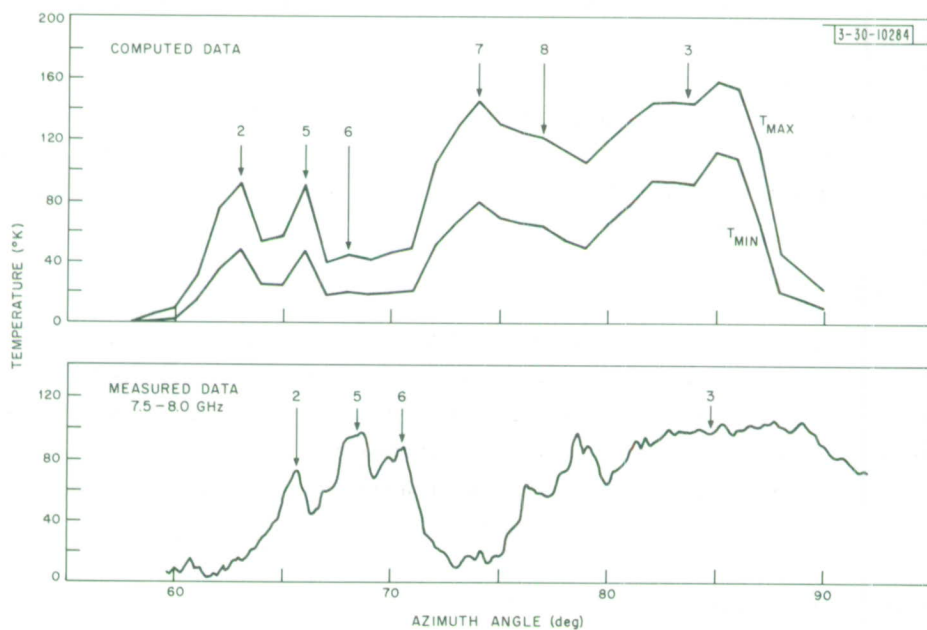


Fig. IV-11. Comparison of computed and measured antenna temperature for azimuth scan through section of squall line east of Haystack site.

Section IV

The composite sky temperature for the eight showers is shown in Fig.IV-11. Showers 1 and 4 contribute less than 15°K each and are lost in the contributions of the stronger rain cells. Reflectivity values in excess of L5 are necessary to generate the peaks in the measured and computed temperature data. The peaks due to showers 2, 5 and 6 are obvious. The measured sky temperature peaks fall within the expected maximum and minimum temperatures. The maximum and minimum expected temperatures are generated by using the Laws and Parsons curve in Fig.IV-3. The attenuation coefficient for the maximum and minimum Z_{eff} value for each level was multiplied by the distance along the ray in the volume corresponding to the level on the weather map, then converted to sky temperature. The azimuths of the measured and computed temperature peaks 2, 5 and 6 do not correspond exactly. A range error of the order of 10km is possible at the distances greater than 100 km from M.I.T. This can contribute to a 2° azimuth error relative to Haystack, sufficient to reconcile the computations and measurements for showers 2, 5 and 6.

The results for azimuths between 80° and 90° show a difference between the measured temperature, 100° peak, and the computed data 113°-160°, narrow peak. The source of attenuation at these azimuths is the strong cell in shower 3 along the cross section given in Fig.IV-10. The ray from Haystack crosses the shower at about the same height as the center of the beam for the weather radar. The map data should be directly applicable to sky temperature computations for this shower position. The height data show that the southern edge of the cell is in reasonable agreement with the map, but the northern edge is not. An error of as much as 4° may be evident in positioning the northern edge on the radar map. This means that except for the sharp peak in the computed curve, the shapes of the observed and computed curves can be reconciled. The sharp peak may be due to hail which can cause a large backscatter cross section but does not contribute to the sky temperature.

Peaks 7 and 8 evident in the measured data between azimuths 75° and 80° appear to be caused by showers 7 and 8. The identification of these peaks is difficult and the lack of agreement in sky temperature is obvious. Lack of agreement in the temperature for shower 3 is also evident. Interpretation of results for shower 3 is difficult because it is in the near field of the Haystack antenna system.

4. Summary

The rain propagation studies are progressing toward refining the estimates of attenuation and sky temperature by means of weather radar. At present a sizable statistical spread in the per-unit-volume scattering statistics and, in some instances, a lack of agreement in the sky temperature and weather radar measurement comparisons are evident. These problems are being worked on by improving both the computation procedures and the measurement techniques.

R.K. Crane

C. AURORAL OBSERVATIONS

1. Introduction

Radar investigation of the aurora borealis using the Millstone L-band system and the 84-ft parabolic antenna, which was begun in February 1965, was discontinued in December 1965

largely because radar echoes from the aurora were being obtained less frequently than earlier in the year and were usually quite weak. Analysis of the data recorded during this period of observation is continuing and will be the subject of a future report.

On the majority of days when auroral echoes were obtained, they were of relatively short duration – from a few minutes to almost an hour – and were received only at the lowest elevation angles, i.e., from zero to about 3° . On a few days, however, the echoes persisted for periods up to several hours and were also obtained at appreciably higher elevation angles – on one day up to 13° . The data obtained on these days are of particular interest because they can be used to determine the spatial distribution of the scattering centers which are the source of the auroral echoes. Some of the data recorded on 5 November 1965 have been chosen for analysis in this report, primarily because the echoes on this day were the strongest obtained in nearly a year of auroral observation. These data are examined to determine the spatial distribution of the auroral echoes, their aspect sensitivity and height dependence and the radar cross section of these echoes for the Millstone L-band radar system.

2. Observation Procedures

The method of recording auroral data consisted in stepping the antenna in 5° increments of azimuth at constant elevation angle across the sector from which the auroral echoes were received. At the completion of each pass across the sector, the elevation angle was changed by 0.5° and the antenna again stepped across the sector. At each step the received signal was integrated for a period of 10 seconds. During the time when the data examined here were obtained, the region producing the auroral echoes extended from about 320° true bearing in the west to beyond 15° in the east and from zero-degree elevation to 4.5° . However, the region to the east of 15° was not investigated because of the possibility that the Millstone radar might interfere with the Haystack site at a bearing of about 19° . The total time required to probe the volume producing the auroral echoes was approximately thirty minutes.

3. Results

The shape of a typical strong auroral echo is shown in Fig.IV-12. Each point in the curve gives the cross-section per unit volume at the indicated slant ranges. These values of cross section are computed for a volume whose diameter is determined by the half-power beamwidth of the antenna (0.7°) and whose length is determined by the length of the transmitted pulse ($500\mu\text{sec}$). The shape of this curve shows only approximately the distribution of the echo-producing sources. It is distorted by the width of the pulse over the entire curve and at the leading and trailing edges by the fact that at these low elevation angles the beamwidth of the antenna is not filled over the first and last 60 to 75 km of slant range. Height above the earth for the center of the pulse at the center of the antenna beam has been computed from the slant range and the refraction-corrected elevation angle.

Values of cross-section per unit volume, similar to those in Fig.IV-12, were obtained for each azimuth step of the antenna at each elevation angle. The values at all azimuths for a given elevation angle were arranged in the form of a grid, and contours which are 1, 3, and 6 db down from the maximum cross section at this elevation angle were drawn. These contours for

Section IV

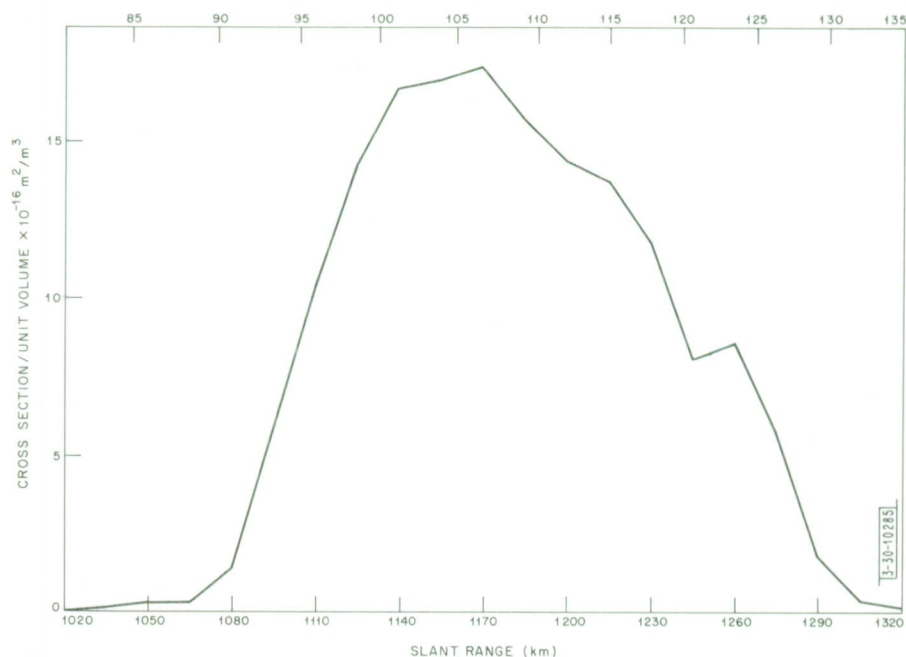


Fig. IV-12. Distribution of auroral echo strength with slant ranges, 0.5° elevation, 0° azimuth, 5 November 1965, 17:17:15 – 17:17:25 EST.

elevation angles of 0.5° , 1.5° , 2.5° , 3.5° , and 4.5° are shown in Figs. IV-13 through IV-17, respectively. The heavy dot in each figure gives the location of the strongest portion of the auroral echo at the given elevation angle. The symmetrical curves on these figures show the location of equal angles between the direction of the radar ray and the normal to the earth's magnetic field lines. At zero angles the rays are parallel to the normal and orthogonal to the field lines. These curves are based on computations made by using a 48-term Legendre polynomial to describe the earth's magnetic field. (The computations were made by Dr. Shou-Chin Wang of Lincoln Laboratory.) The height above the earth was calculated from the slant range as explained previously for Fig. IV-12.

Examination of Figs. IV-13 through IV-17 shows that the strongest portion of the echo at each elevation angle is located very close to the orthogonality curve and that the 1-db contour shows a very strong tendency to be centered about this line. It is evident, also, that most of the echoes are within about $\pm 2^\circ$ of orthogonality. This is in good agreement with Leadabrand, *et al.*,¹⁵ and other workers at lower frequencies who have found that auroral echoes are strongly aspect-sensitive and that this sensitivity increases with increase in the transmitted frequency.

The location of the 6-db contours gives some idea of the heights from which the auroral echoes are received. However, the heights shown here are only approximate in that they are for the center of the antenna pattern, whereas in reality the lower limit of the auroral region height is measured by the upper edge of the half-power width of the antenna beam and the upper limit by the lower edge of the antenna beam. From the data considered in this report, it was determined that the average thickness of the region producing the auroral echoes was 30 km and that

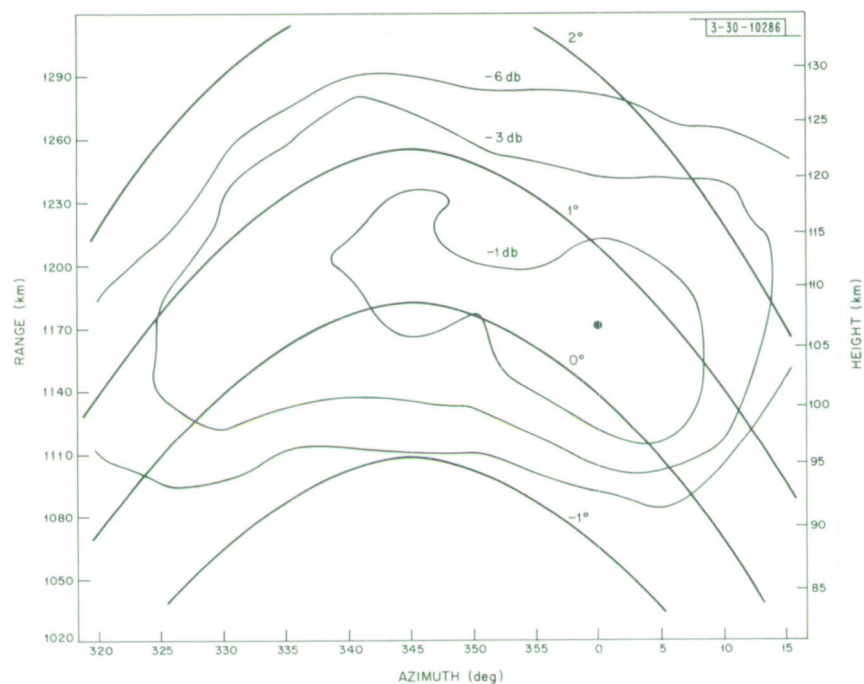


Fig. IV-13. Spatial distribution of auroral echoes, 0.5° elevation, 5 November 1965, 17:16:30 – 17:19:25 EST.

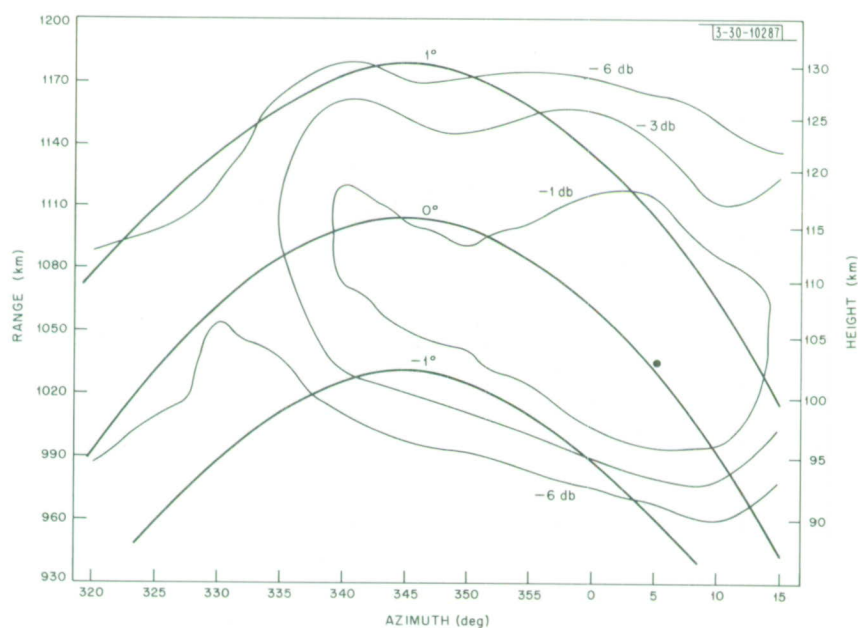


Fig. IV-14. Spatial distribution of auroral echoes, 1.5° elevation, 5 November 1965, 17:23:30 – 17:26:25 EST.

Section IV

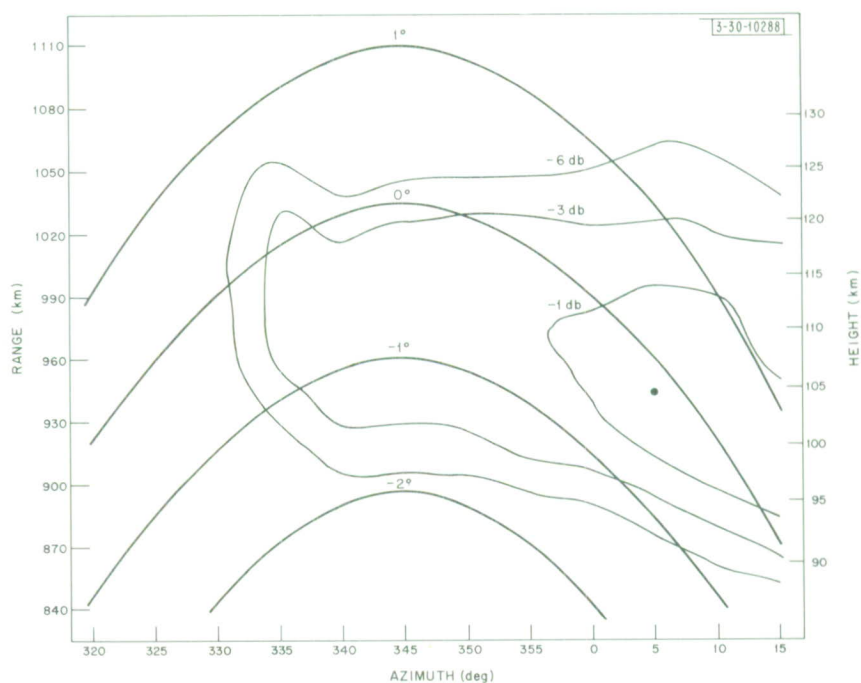


Fig. IV-15. Spatial distribution of auroral echoes, 2.5° elevation, 5 November 1965, 17:30:30 – 17:33:25 EST.

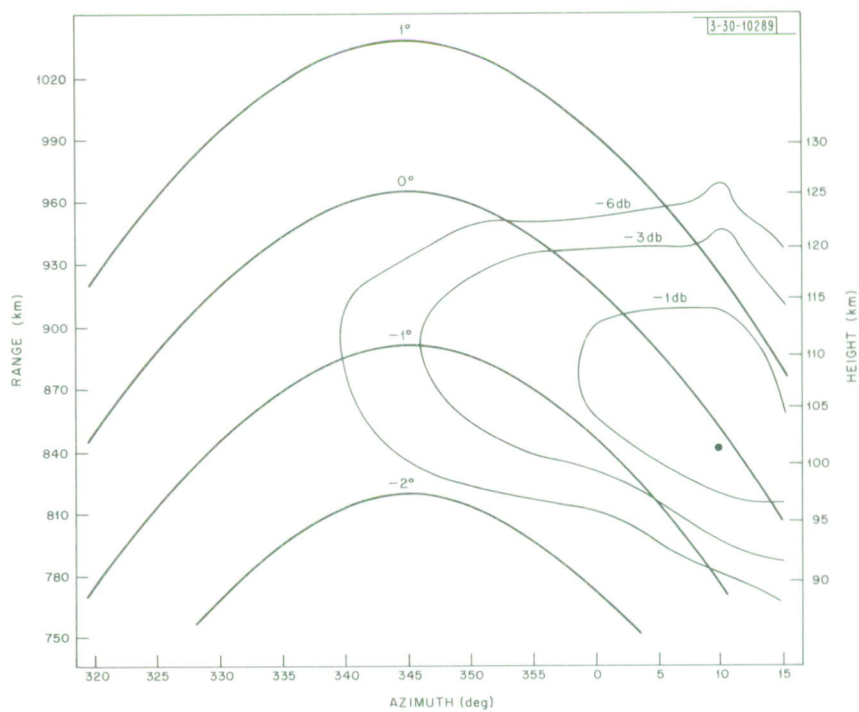


Fig. IV-16. Spatial distribution of auroral echoes, 3.5° elevation, 5 November 1965, 17:37:30 – 17:40:25 EST.

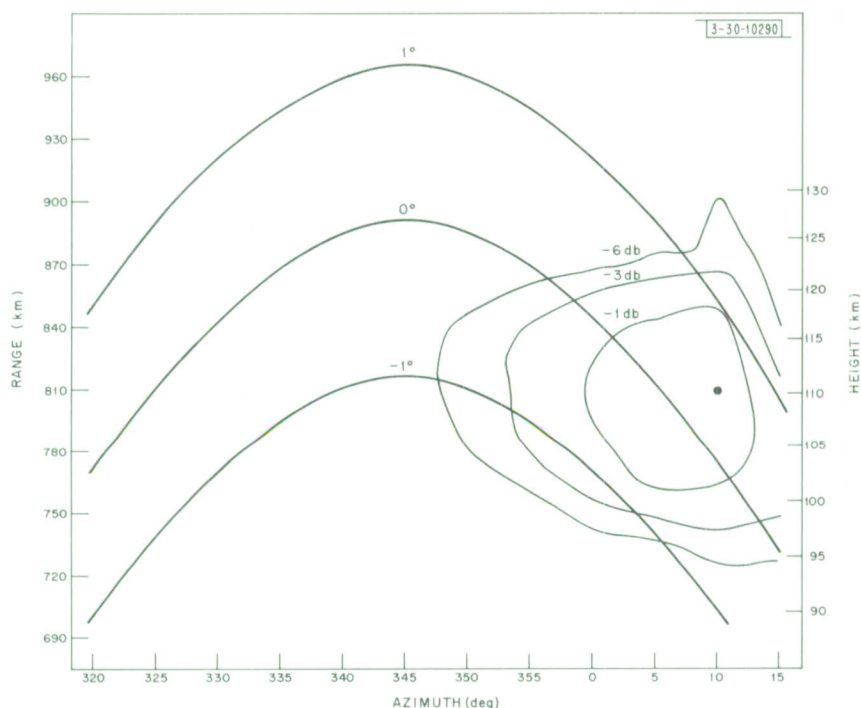


Fig. IV-17. Spatial distribution of auroral echoes, 4.5° elevation, 5 November 1965, 17:44:30 – 17:47:25 EST.

it extended from about 90 to 120 km above the earth. This is a somewhat greater thickness than that previously reported by Unwin,¹⁶ Stone, *et al.*,¹⁷ and Leadabrand, *et al.*,¹⁵ but it should be emphasized that this value is for a strong aurora whereas those reported by other workers are the average of many auroras, both weak and strong. Moreover, our data do show that the larger values of layer thickness are associated with the stronger echoes.

In the last report¹ it was erroneously stated that the radar cross section of L-band auroras could have values up to many tens of square meters for the Millstone radar. It should have been given as tenths of square meters. The largest value of radar cross section measured to date was approximately 0.4 m^2 .

Future work on L-band radio auroras at Millstone is indefinite at this time. However, it is hoped that since we are now in the period of increasing solar activity and the accompanying increase in the rate of occurrence of aurora, an opportunity will be found to resume auroral observations on the same modest scale as during 1965. In the meantime, the analysis of auroral data is continuing and it is expected that a report on this work will be out shortly.

W. G. Abel

Section IV

REFERENCES

1. Radio Physics and Astronomy Report, Lincoln Laboratory, M.I.T. (1965:1), DDC 629923.
2. J. W. Ryde and D. Ryde, "Attenuation of Centimetre and Millimetre Waves by Rain, Hail, Fog and Clouds," Report No. 8670, General Electric Corporation Research Laboratory, London (1945).
3. K. L. S. Gunn and T. W. R. East, "The Microwave Properties of Precipitation Particles," Quart. J. Roy. Meteorol. Soc., 80 (346), 522-545 (October 1954).
4. T. Oguchi, "Attenuation of Electromagnetic Wave Due to Rain with Distorted Raindrops," J. Radio Research Lab. (Japan) 7, 467-485 (September 1960).
5. ———, Part II, J. Radio Research Lab. (Tokyo) 11, 19-44 (1964).
6. R. G. Medhurst, "Rainfall Attenuation of Centimeter Waves: Comparison of Theory and Measurement," IEEE Trans. Antennas Propag. Ap-13, 550-564 (1965).
7. D. Deirmendjian, "Complete Microwave Scattering and Extinction Properties of Polydispersed Cloud and Rain Elements," Report No. RAND-R-422-Pr, RAND Corporation, Santa Monica, California (December 1963), AD-426-139.
8. D. C. Hogg and R. A. Semplak, "The Effect of Rain and Water Vapor on Sky Noise at Centimeter Wavelengths," Bell System Tech. J. 40, 1331-1349 (September 1961).
9. H. E. Bussey, "Microwave Attenuation Statistics Estimated from Rainfall and Water Vapor Statistics," IRE Proc. 38, 781-785 (July 1950).
10. S. Ugai and Y. Kaneda, "Statistical Estimation of Microwave Attenuation due to Rain Cells," Rev. Elec. Commun. Lab. (Japan) 11, 268-283 (May-June 1963).
11. H. G. Van de Hulst, Light Scattering by Small Particles (Wiley, New York, 1957), Ch. 9.
12. D. E. Kerr, Propagation of Short Radio Waves, Vol. 13, M.I.T. Radiation Laboratory Series (McGraw-Hill, New York, 1951).
13. K. L. S. Gunn and G. D. Kinzer, "The Terminal Velocity of Fall for Water Droplets in Stagnant Air," J. Meteorol. 6, 243-248 (August 1949).
14. J. O. Laws and D. A. Parsons, "The Relation of Rain Drop Size to Intensity," Am. Geophys. Union Trans. 24, 452-460 (January 1944).
15. R. L. Leadabrand, J. C. Schlobohm and M. J. Baron, "Simultaneous Very High Frequency and Ultra High Frequency Observations of the Aurora at Fraserburgh, Scotland," J. Geophys. Research 70 (17), 4235-4284 (September 1965).
16. R. S. Unwin, "Studies of the Upper Atmosphere from Invercargill, New Zealand 1, Characteristics of Auroral Radar Echoes at 55 Mc/s," Extrat Des. Ann. Geophys. 15 (3), 377 (July-September 1959).
17. M. L. Stone, R. P. Ingalls, C. H. Dugan and L. P. Rainville, private communication.

V. SPACE SURVEILLANCE TECHNIQUES

A. MILLSTONE RADAR

The Space Surveillance Techniques (SST) program for the Millstone radar was described in considerable detail in the last Radio Physics and Astronomy Report.* This program consists basically of two parts: (1) routine satellite tracking operations, including support to the MITRE/Millstone Interferometer experiment and (2) a sensor improvement program, including the acquisition of an orbit upgrading program for the SDS-9300 computer and development of a range extension program utilizing both coherent and incoherent signal integration techniques. Routine satellite tracking continues on about the same level as described in the earlier report. Significant progress has been made in the sensor improvement program.

An orbit upgrading program has been procured from TRW Systems, Inc. This program which is based on ESPOD (Electronics Systems Precision Orbit Determination) programs developed for the Air Force is a two-part program. The first part is a non-real-time program, called NRTPOD, which makes use of tracking data from one or more sensors to update orbital elements. The second part, called MHESPOD, is a real-time program which makes use of nominal orbital elements corrected by data that are currently obtained by the radar to upgrade pointing instructions for the remaining portions of a satellite pass. NRTPOD and MHESPOD have been delivered and are presently being integrated into the Millstone Hill system.

Discussion of the range extension program in the previous report described two methods of digitizing the radar data and passing it to the computer at the required rate. The first, called DIGIMON, used a special-purpose computer and involved the use of frequency multiplexing and a pair of high-speed analog-to-digital converters. The second, called MACS, uses sample-and-hold circuits and analog-to-digital converters to encode the outputs of sine and cosine phase detectors. DIGIMON has since been abandoned because of the inability to obtain A/D converters with the required speed and accuracy. An expanded version of MACS has been designed which normally uses six 10-bit A/D converters to encode the sine and cosine outputs of one sum receiver and the two difference receivers in the monopulse system. An additional pair of A/D converters is provided which can be used when needed to encode the output of a fourth receiver. The new MACS assembles a 20-bit word consisting of 10 bits each from two data channels and passes it to the computer in approximately the 1.75- μ sec cycle time of the memory. The A/D converter system which employs integrated circuitry has been ordered for delivery in July 1966.

The computation rates required in the range extension program are very high. The computation problem was discussed in the last report and one method of attacking it by Fourier analysis using the Cooley-Tukey algorithm was mentioned. A seemingly more promising approach is being investigated which involves a correlation filter (CFE-1) made by Scientific Data Systems. The CFE-1 is a special-purpose high-speed accessory designed for use with the SDS-9300 computer. It has a basic word length of 12 bits and it can perform 10 complete multiply-and-add

*Radio Physics and Astronomy Report, Lincoln Laboratory, M.I.T. (1965:1), DDC 629923.

Section V

routines in one memory cycle (1.75 μ sec) of the SDS-9300. It can obtain an autocorrelation function directly, and, in conjunction with appropriate programs in the 9300, can, at a great saving in time, perform most of the digital filtering that is usually done by the main computer alone. These properties of the CFE-1 make it a useful tool for many other experiments requiring very high-speed signal processing.

J. C. Henry D. P. Hynek
G. M. Hyde V. C. Pineo

B. HAYSTACK X-BAND PASSIVE AUTOTRACKER

An X-band passive tracking capability utilizing the 120-ft antenna has been developed at Haystack Hill. This tracker is intended to angle track cooperative satellites such as Lincoln Experimental Communications Satellites LES-2 and LES-4. These satellites are in eccentric orbits with great apogee heights; consequently, conventional satellite radar trackers such as Millstone can observe only a small portion of the orbit near perigee. However, the Haystack large-aperture precision angle tracker can obtain good time-angle data on approximately an eight-tenths segment of a LES-4 10-hour orbit in 20 percent of the passes. Data obtained on such a large portion of the orbit enable a precise determination of the orbital parameters. The accuracy of this method of orbit determination has been demonstrated on LES-4. Haystack angle data on this satellite taken on 24 and 25 February 1966 used in an orbit fitting program had an RMS error of only 0.0061 deg.

The Haystack passive tracker employs solid state electronics with a four-horn monopulse type feed in an auto-track system in which the tracking loop is closed through the Univac U-490 computer. A duplexed single-channel receiver is used for the elevation and azimuth error signals. Error voltages, determined with phase detectors, are digitized and fed to the U-490. Antenna commands are given as digital numbers to the digital angle servos. Doppler frequency tracking is accomplished with a computer-directed local oscillator and a phase-locked loop.

R. R. Silva

C. RUBY LASER RADAR

A program for studying the extension of radar techniques into the region of infrared and optical wavelengths is in progress. High peak powers are available from ruby lasers operated in the "Q-switched" mode where single pulses of 250 megawatts or more, with about 20 nanosecond duration, may be produced at up to one pulse per second rates. With such high peak powers available in narrow beams (about one milliradian), it has been possible to obtain strong reflections from orbiting satellites which have been equipped with cube-corner optical reflectors.* Such short pulse durations enable precise timing of the return echoes such that accurate satellite ranges may be obtained.† The low repetition rate and the narrow beam angle of the laser effectively prevent acquisition and tracking with the laser radar alone. However, by interconnecting the laser mount with a microwave radar capable of tracking satellites within the accuracy required by the laser beam, laser echoes are not necessary for tracking but may be used for precise ranging. In

* H. M. Plotkin, Quantum Electronics, Proceedings of the Third International Congress (Columbia University Press, New York, 1964).

† P. H. Anderson, C. G. Lehr, L. A. Maestre and G. L. Snyder, IEEE J. Quantum Electron. QE-2 (August 1966).

addition, microwave radar tracking allows laser ranging during any period satellites are overhead, not solely when they are sunlit against a darkened sky.

The Millstone L-band radar is able to track small satellites to within one milliradian, hence can provide pointing information to a laser mount. A Nike-Ajax radar mount has been modified to accept a ruby laser head and a ten-inch receiving telescope. Position synchros on the mount are interconnected to position synchros on the Millstone antenna to allow slave tracking by the laser mount. The mount has been installed on a 40-ft tower, Tower 3, located approximately 350 ft west of the Millstone 84-ft antenna. A photograph of the mount with the laser radar being pointed by Millstone is shown in Fig. V-1. Operating controls are provided in a van located beside the base of the tower, with supporting laboratory space available in a 50-ft trailer. The pointing mount is installed on a hexagonal wooden platform with side walls and enclosed by a folding aluminum frame covered with weatherproofed canvas. In order to allow for optical alignment of the equipment during daylight hours, the canvas cover has a black interior surface and has a white exterior to minimize the temperature rise inside.

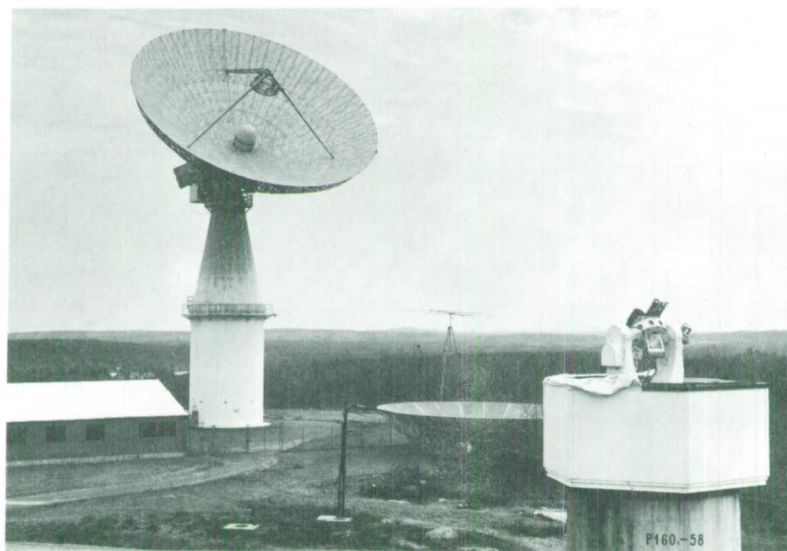


Fig. V-1. Ruby laser radar (right) and Millstone 84-ft tracking antenna (left).

The Millstone antenna beam-pointing direction is sometimes as much as a milliradian from the synchro indications over its full elevation range, because of mechanical deflections.* Therefore, the interconnecting synchro line has been provided with a pair of position correction synchros that allow both elevation and azimuth position signals to be modified by handwheel controls. A boresight television camera allows the mount operator in the control van to view an illuminated object (such as the Echo balloons) during a track. By observing a number of Echo I and II tracks on the boresight monitor, it was possible to determine a set of elevation corrections to apply to

*Data from the Millstone computer are corrected for this sort of error as well as refraction. The optical radar, however, since it is synchro-positioned from the antenna directly, receives uncorrected angle data.

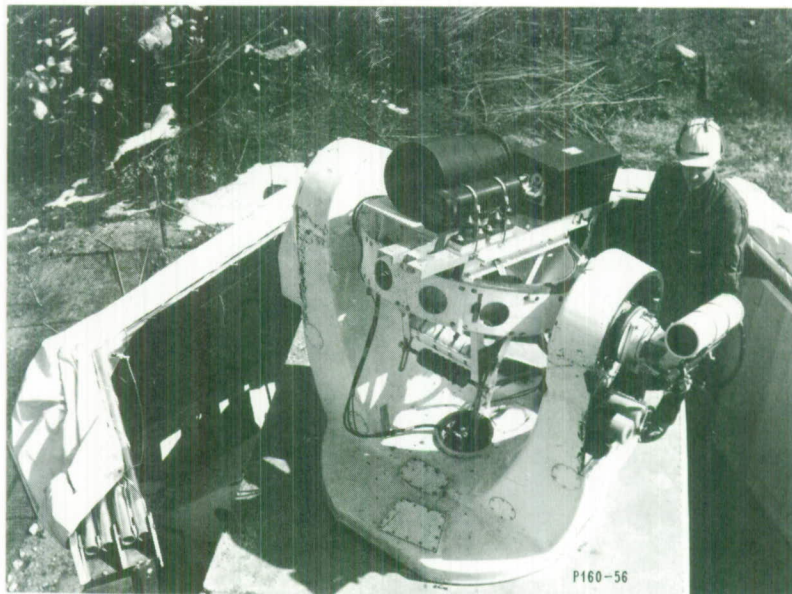


Fig. V-2. Ruby laser radar on Nike-Ajax mount.

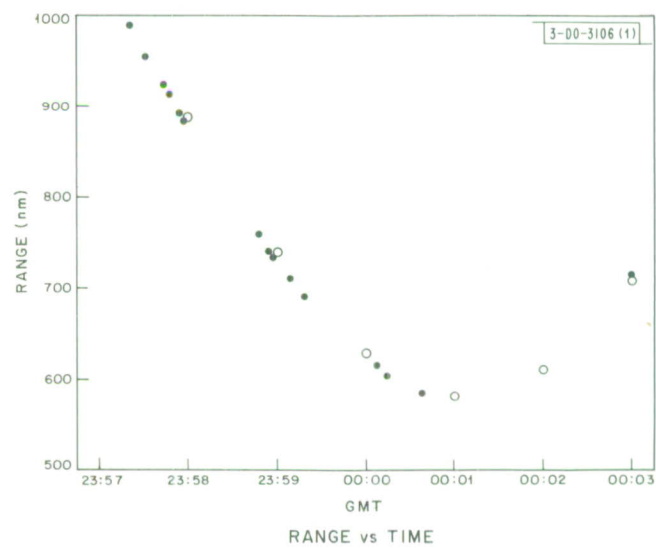


Fig. V-3. Range determination for Explorer XXII.

the Millstone antenna positions. Using these corrections, it is possible to hold the image of the Echo balloons well within one milliradian of the Nike mount axis.

The ruby laser employed in this program is a commercial unit (supplied by Applied Lasers, Inc., Stoneham, Mass.) consisting of a 5/8 in. diameter by 7-1/4 in. long ruby mounted for output at Brewster's angle and excited by two linear flashlamps in a dual elliptical cavity. The optical cavity is Q-switched by a combination of a rotating quartz rooftop prism and a saturable dye cell. Circulating water (in winter months, and alcohol-water mixture) maintains the temperature of the lamps and ruby at a constant temperature. The operating temperature of the laser is selected so that the output wavelength does not coincide with any of the narrow atmospheric absorption lines. The 20-kw power supply and the water circulation system are located inside the tower below the mount.

Next to the laser head is a 10-inch Cassegrainian telescope for reception of the satellite echoes. A red-sensitive photomultiplier with a 30-Å interference filter provides skylight discrimination, and the pulse output is fed through an adjustable height discriminator. This passes pulses which exceed a predetermined threshold level during a gate period. The discriminator output pulse is used to stop a time interval counter which has been initiated by the outgoing laser pulse. Time intervals are resolved to a precision about one nanosecond with the unit in use. The laser transmitter and receiving telescope in place on the mount are shown in Fig. V-2.

Echoes from the satellite Explorer XXII have been obtained for ranges between 580 and 1000 nautical miles. Data given in Fig. V-3 show the laser radar range measurements as solid circles and position prediction (from month-old orbital parameters) as open circles. Time-of-day determinations for these observations are good only to about 3 seconds, because recording was performed manually.

Modification of the laser radar is currently in progress. The 10-in. telescope has been replaced by a 23-in. telescope. A thermoelectrically cooled photomultiplier housing and a 5-Å interference filter are being included to increase threshold sensitivity of the receiving system. Accuracy in both the time of observation and time interval measurements is being improved by referring a digital clock and the interval unit to the station frequency standard located at Haystack. Automatic data recording is also being provided.

H. A. Bostick
P. R. Longaker

VI. SYSTEMS DEVELOPMENT

A. EQUIPMENT DEVELOPMENT FOR FOURTH TEST OF GENERAL RELATIVITY

A new high-accuracy high-sensitivity ranging radar is being developed at Haystack for the measurements required for the fourth test of general relativity.¹ The detection ability of the radar will be improved by about 10 db over that provided in the system currently in use for planetary observation. System parameters for a new plug-in box for planetary radar astronomy are given below.

Frequency	7.840 GHz
Transmitter power	500-kw CW
Antenna gain (including radome effect)	66 db over isotropic
System temperature	75°K

The increase in performance will be achieved by the use of a newly developed klystron power amplifier and a traveling-wave maser. Varian Associates has completed initial testing of a klystron at 200 kw. The objective of the development program is a 250-kw klystron. Two klystrons will be operated in parallel to produce from 400 to 500 kw. The transmitter power output will be limited to 400 kw average until the safe operating margins on the waveguide components have been established. A TW maser has been completed and delivered to Lincoln Laboratory. The maser contributes 10°K to the system noise temperature while operating with gain in excess of 35 db and with a bandwidth of 25 MHz.

The system block diagram shown in Fig. VI-1 gives the configuration of the microwave transmitting and receiving equipment installed in the planetary radar box and the frequency translation,

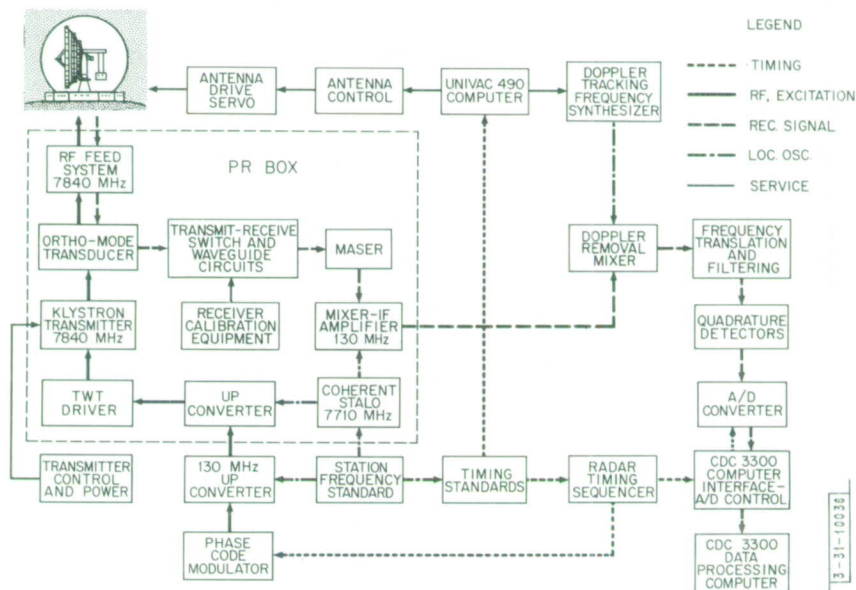


Fig. VI-1. System block diagram for fourth test experiment.

Section VI

control and digital data processing equipment located in the Haystack control room. The antenna will be illuminated with a circularly polarized feed horn. Initially a single receiver channel polarized orthogonally with respect to the transmitted signal will be used for receiving. A mechanically operated switch is provided to prevent overloading the maser during the transmitting interval. Coherence of the transmitted and received signals is established by a phase-locked stable LO. An appropriately phase-coded IF signal is mixed with the LO output to provide the excitation for the transmitter. The received signal is heterodyned to an IF of 130 MHz, after being amplified by the TW maser. This IF signal is further processed by equipment located in the control room where the Doppler frequency shift is removed and the signal data digitally encoded for computer processing. Improved ground level receiving, data processing and control instrumentation are required for the fourth test experiment. A description of this new instrumentation follows.

1. Receiver Ground Equipment

The Doppler shift of the received signal is removed by offsetting the frequency of the 100-MHz second receiver LO using a coherent frequency synthesizer. A slewed 1-MHz clock signal is derived from the Doppler synthesizer output which, when appropriately divided in frequency, is used by the radar timing equipment to track the target in range. The frequency synthesizer is externally programmed to track the predicted Doppler frequency. The existing equipment steps the synthesizer smoothly in 0.1-Hz steps, with provision for extending this to 0.01-Hz increments for greater precision. The frequency synthesizer is controlled either by the Univac 490 pointing computer, using a computed Doppler ephemeris, or by a device which is programmed to produce a linear rate of change in frequency with time at a rate which best matches the predicted Doppler frequency rate.

2. Terminal Equipment

A new set of terminal equipment operating at a 2-MHz IF frequency has been designed for the experiment and is currently under construction. This terminal equipment provides phase detection (zero frequency conversion) of the radar signals to generate the two orthogonal components to be analyzed by computer processing. Matched filtering of these signals to the pulse width or baud length of the modulation is used to obtain the highest signal-to-noise ratio.

The filtered signals are converted to digital form for computer processing with an analog sample-and-hold multiplexer and a high-speed analog-to-digital converter. A versatile interface subsystem has been constructed and partially checked. This subsystem transfers the digitally encoded data from the converter to the Control Data Corporation 3200 data processing computer. This interface also reads time from the station clock for use in the data processing procedure, and provides a channel for the computer program to control events or devices external to the computer or to ascertain the status of the experiment (i.e., whether transmitting or receiving).

3. Radar Timing Sequencer

The radar sequencer equipment presently under construction will control the system timing for the NASA Lunar Mapping Program and for the instrumentation of Shapiro's fourth test of the

general theory of relativity. Subsystem timing (pulse length, repetition rate, etc.) will be controlled by existing equipment under supervision of the radar sequencer.

The sequencer unit will provide for operator control of the following functions:

- (a) System start
- (b) Phase code modulation of transmitted signal
- (c) Radar return processing
- (d) System stop.

Various status signals will be available to drive external equipment and to present a visual indication of the overall system operation. In addition, several synchronization tests will be implemented and the results displayed on the operator control panel. Facilities will be provided for remote sensing of all status and test signals in anticipation of future requirements.

The radar sequencer is presently under construction with a 1 July 1966 target date to start checkout. Unit checkout will require a minimum of 2 to 3 weeks, at which time the system tests are scheduled.

M. L. Stone
R. P. Ingalls

B. THE MILLIMETER-WAVE FACILITY AT LEXINGTON

1. Introduction

Lincoln Laboratory procured a 28-ft-diameter antenna in 1961 as part of a millimeter-wave system development program. The reflector, which was required to operate at wavelengths in the region of 8 mm, was formed by a technique known as "spincasting" by the Kennedy Antenna Division of the Electronic Specialty Corporation. This technique for constructing precision paraboloidal reflectors with a large aperture-to-wavelength ratio has been described by Dawson.² A more complete description of the antenna and its electrical performance is given in Appendix B of this report. Evaluation tests of the 28-ft reflector were performed using an El-Az mount installed on the roof of Lincoln Laboratory Building D, and a test transmitter at a distance of about 6 miles. The results of these tests were so favorable that the antenna was later used as the basis of a radar operating at 8.6 mm and for millimeter-wave radiometry.

The first data on the reflectivity of the moon at millimeter wavelengths were obtained with this radar and were reported by Lynn, *et al.*³ Use of the radar was discontinued following the moon measurements because of lack of funds required to accomplish a significant improvement in performance. However, the antenna has since been used for radiometry at 8.5 mm (Ref. 4) and 1.5 cm. An account of the radiometric measurements at 1.5 cm is given in Sec. III-A of this report.

Recently, as a result of renewed interest in radar studies of the lunar surface, the radar has been reassembled and a program to upgrade its performance has been undertaken.

2. The 8.5-mm Radar

The present radar is essentially the same as that used in the moon experiments reported by Lynn, *et al.*³ The transmitter consists basically of a 10-watt floating-drift-tube klystron oscillator, phase-locked to the required frequency which is derived from a crystal-controlled frequency multiplier. The klystron is an Elliott Brothers (England) type 8FK1.

Section VI

The front end of the receiver is a balanced mixer using 1N53CMR crystal diodes. The noise figure is about 14db. Triple conversion reduces the signal to 2.5 kHz, after which it passes through a bandpass filter into a detector and a pen recorder. Equipment now being prepared will integrate the detected signal and register the received energy on an IBM card. The present bandwidth of the receiver is 170 Hz, somewhat more than the greatest Doppler spread caused by the moon's libration. Doppler shift introduced by rotation of the earth and by ellipticity of the moon's orbit is compensated by programming the second LO.

3. Millimeter Radar Improvement Program

The first improvement will be made in the transmitter with the replacement of the 10-watt 8FK1 klystron by a 50-watt 8FK15 during the latter half of 1966. The 50-watt klystron oscillator is similar to the 10-watt tube presently in use and phase-locking to a frequency standard will be necessary in order to attain the frequency stability required in moon experiments. A 1000-watt klystron amplifier is being developed by Varian Associates for Lincoln Laboratory in connection with the NASA lunar studies program.

Another important improvement will be the introduction of polarization diversity to permit three modes of operation:

- (a) Transmit circular polarization and receive two circular polarizations of opposite sense.
- (b) Transmit circular polarization and receive orthogonal plane polarizations, oriented at will.
- (c) Transmit plane polarization oriented at will and receive in that plane and in the orthogonal plane.

It is expected that at millimeter wavelengths there will be a very appreciable amount of depolarization by most or all parts of the moon, and that a useful signal-to-noise ratio will be found in both channels of the dual-polarization receiver even when the transmitted power is only 50 watts. Later, when the 1-kw tube is delivered, it may be possible to split the beam into narrow strips by Doppler filtering, and thus to examine specific features of the lunar surface which have exhibited anomalous scattering behavior at longer wavelengths (Thompson^{5,6}).

4. Radiometry with Millimeter-Wave Facility

Heretofore, the usefulness of the antenna in radiometry has been limited by the coarseness of the pointing mechanism; five meshes of low precision gears have intervened between the indicating equipment and the azimuth or elevation axis of the dish. Sixteen-bit angular position encoders are now being placed directly on the azimuth and elevation axes. When binary-to-decimal round-off errors are allowed for, these encoders will indicate position with maximum errors of +23 or -32 seconds of arc. Elasticity of the mount and thermal displacement of the supporting columns will affect the fiducial positions, but these factors can be measured and considered. It seems realistic to hope for pointing indication with error not exceeding one minute of arc, which is a quarter of the 3-db beamwidth.

A second limitation on the use of this facility for radiometry has been the sensitivity of the available receivers. At 35 GHz, the noise temperature of the radiometer receiver has been

more than 3300°K. Parametric amplifiers available at 35 GHz have not been attractive for radiometry, because the few that have been built have had narrow pass bands. A new development in varactors now gives promise of a 35-GHz parametric amplifier with a noise temperature of only about 20°K and a bandwidth of at least 1 GHz. The effective temperature of the system, including waveguide and atmosphere, would be about 330°K. The possibility of procuring a pair of these amplifiers to be used with the dual-polarization plumbing is being considered.

The existing parameters and planned improvements for the microwave facility are summarized below.

Antenna:	Half-power beamwidth (one way) at 35 GHz	4.0'
	Gain, including 1.4-db losses	65.9 db
	Polarization { Existing Goal	Horizontal Complete flexibility
Transmitter:	Existing - locked oscillator	10 watts
	Near future - locked oscillator	50 watts
	Goal - coherent amplifier	1000 watts
Receivers:	Existing - single channel	3300°K
	Goal - dual channel	330°K

J. J. G. McCue
A. F. Standing
E. A. Crocker

REFERENCES

1. Radio Physics and Astronomy Report, Lincoln Laboratory, M.I.T. (1965:1), pp. 61-68, DDC 629923.
2. J. W. Dawson, "28-ft Liquid-Spun Radio Reflector for Millimeter Wavelengths," Proc. IRE 50, 1541 (June 1962).
3. V. L. Lynn, M. D. Sohigian and E. A. Crocker, "Radar Observations of the Moon at 8.6-mm Wavelength," Technical Report 331, Lincoln Laboratory, M.I.T. (8 October 1963), DDC 426207. See also, J. Geophys. Research 69, 781-783 (1964).
4. V. L. Lynn, M. L. Meeks and M. D. Sohigian, "Radiometric Measurements at 8.5-mm Wavelength with a 28-Foot Antenna During December 1962," Technical Report 330, Lincoln Laboratory, M.I.T. (8 October 1963), DDC 430926.
5. T. W. Thompson, "Enhanced Radar Scattering of Young and Rayed Craters," Ph.D. Thesis, Cornell University (September 1965).
6. T. W. Thompson, "Lunar Mapping by Coherent-Pulse Analysis," Radio Science, Special Issue on Planetary Atmospheres and Surfaces (December 1965).

APPENDIX A

EXPERIMENTAL EVALUATION OF 1000-WAVELENGTH ANTENNA

W.D. Fitzgerald, V. L. Lynn, K. J. Keeping

A. INTRODUCTION

The recent demands of space surveillance and space communications have greatly increased the need for very-high-gain, narrow-beam antennas. Until recently, this need has been fulfilled by increasing the physical aperture of reflectors operating at wavelengths of 3 cm or longer. However, the higher frequencies of the millimeter band can improve gain and beamwidth with relatively small structures, while simultaneously permitting extremely wide bandwidths, operation in a relatively unused portion of the spectrum, small size of waveguide components and reduced interference.

Following this reasoning, Lincoln Laboratory initiated a program of millimeter systems development. In conjunction with this effort, a 28-ft-diameter antenna, operating at wavelengths of 8.5 mm, has been installed and tested. The reflector was formed by a technique known as "spincasting" by the Kennedy Antenna Division of the Electronic Specialty Corporation, with engineering and technical assistance from Lincoln Laboratory.

This report describes the evaluation of the test range and the electrical testing of the antenna at a wavelength of 8.5 mm.

B. TEST OBJECTIVES

The test series described in this report was initiated to determine the electrical characteristics more precisely than had been done in the initial tests performed shortly after installation, and to evaluate the effect of environmental conditions on these characteristics. Gain, pattern, and boresight shift measurements were taken to determine the effects of different ambient temperatures, nonuniform solar heating and wind conditions. On a typical daily run, measurements were taken at one to one-and-one-half hour intervals beginning before dawn and continuing until the late afternoon. Approximately 15 complete daily runs were made during various weather conditions which included winds up to 25-30 mph and ambient temperatures ranging from the mid-30's (°F) to the high 80's.

The properties of a test range capable of measuring an antenna with a diameter of 1000 wavelengths pose special problems.¹ Some effects of terrain and propagation phenomena which are negligible in the measurement of antennas with smaller electrical apertures become serious obstacles with a 1000-wavelength aperture. For the range in question, the directivity of the 28-ft antenna at these frequencies is sufficient to virtually eliminate the influence of ground reflections from the measured patterns. However, these ground reflections can still cause errors in the gain measurement (the method used is comparison with a calibrated standard), and propagation phenomena can cause errors in all the major characteristics of the antenna (gain, patterns and boresight). The propagation phenomena of interest (refraction and signal scintillations), although only vaguely associated with site geometry, are considered as properties of the range.

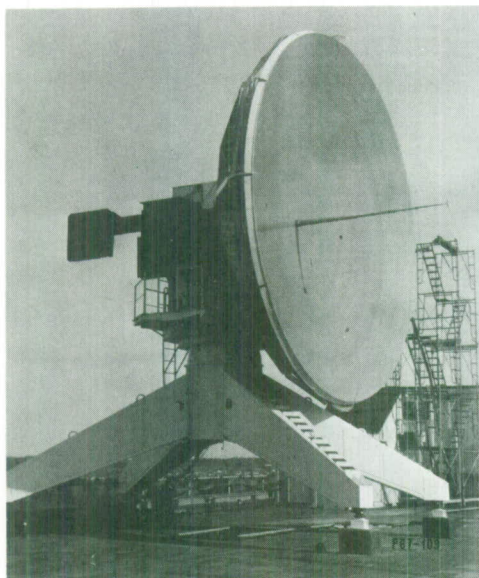


Fig. A-1. 28-ft millimeter antenna
(front view).

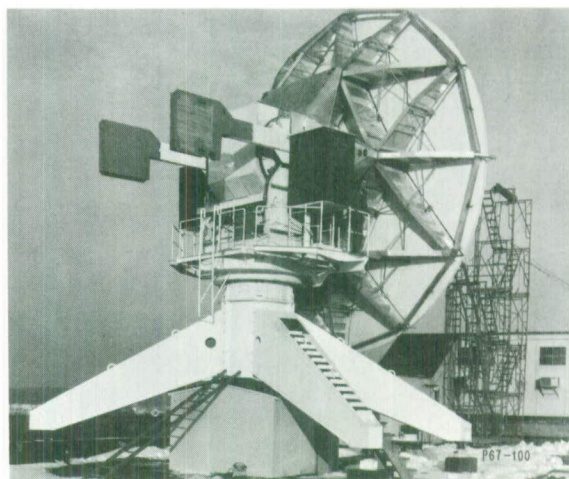


Fig. A-2. 28-ft millimeter antenna
(rear view).

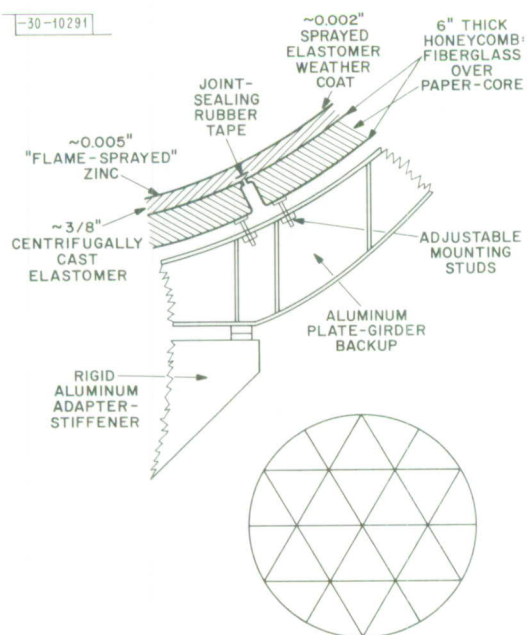


Fig. A-3. Cross section of antenna structure — basic geometry of panels and backup.

An investigation of the range to determine the dependence of terrain and propagation effects on wind, sun, temperature, etc., was undertaken with a view toward separating these "range errors" from actual changes in antenna performance caused by the same changing environment.

C. MECHANICAL DESCRIPTION

Photographs of the antenna mounted on the roof of one of the Lincoln Laboratory buildings are shown in Fig. A-1 and Fig. A-2.

The reflector is supported by an aluminum plate-girder-tangential-beam structure which is shown in Fig. A-2. Also shown in Fig. A-2 is the cab between the counterweights which houses all the microwave equipment. This backup structure is attached to the mount adapter-stiffener at 6 hexagonally distributed points. The reflecting surface is supported by a total of 24 panels individually attached to the backup structure. Each panel is 6 in. thick and constructed of fiber-glass over paper-core honeycomb. The precise spuncast paraboloid is formed over these panels. The actual reflecting surface is a thin flame-sprayed coating of zinc which is then weather protected by a thin coating of plastic. Figure A-3 shows a cross section of the reflector construction.

The feed employed is a "rear feed" type supported by an aluminum column attached to the vertex and guyed at the feed end. The feed, which is described more fully later, consists of an open-ended circular waveguide operating in the TE_{11} mode and a circular splash plate housed in a hemispherical radome. The radome, feed support column and guy wires are shown in Fig. A-1. The cylindrical object seen attached to the feed support is an auxiliary receiver which was removed after initial testing of the dish.

To permit focusing of the antenna without the use of flexible waveguide or movable joints, all the microwave components of the radar and pattern receiver are mounted on a single large plate in the equipment housing. Adjustment is accomplished by movement of the entire plate and feed.

The mount is a manually controlled elevation-over-azimuth type. Both the azimuth and elevation control points are provided with telescopes mounted on the elevation axis and directed through small apertures in the reflecting surface. One telescope is a 4-inch Cassegrainian type used for fine control. Rotation of the mount is limited to 345° in azimuth and from -2° to $+95^\circ$ in elevation. A two-speed synchro system provides information for remote readout and for the pattern recorder.

A more detailed mechanical description and an account of the "spincasting" technique has been given by Lynn, *et al.*² and Dawson.³

D. PATTERN RANGE

Figure A-4 shows a vertical cross section of the test range used in the evaluation program. The transmitting antenna (Billerica) is a 4-ft paraboloid mounted on top of a 130-ft water tower located approximately 31,500 feet from the antenna under test. The power source is a reflex klystron (Varian VA-97) with 20- to 25-mw CW output, remotely controlled with telephone-line relay circuits. The polarization of the transmitting antenna was horizontal throughout the test program.

The intensity with which the transmitter illuminates the terrain is as indicated in Fig. A-4. The 100- to 150-ft valley between the two sites minimizes the interference pattern observed at the receiving site. This interference pattern is of consequence only to the relatively low-gain

Appendix A

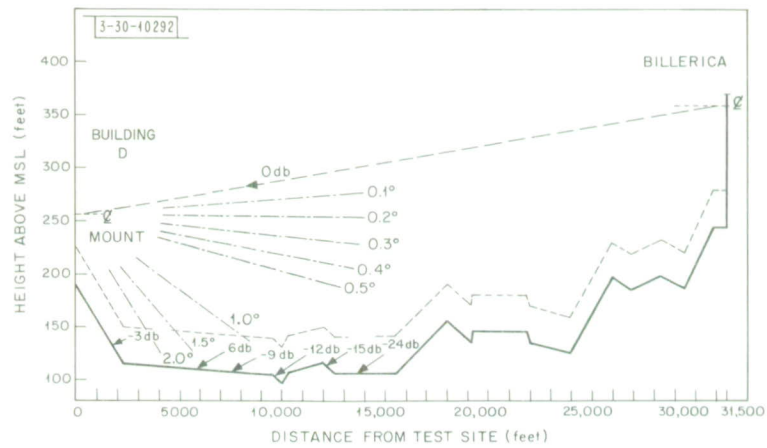


Fig. A-4. Height profile of pattern range.

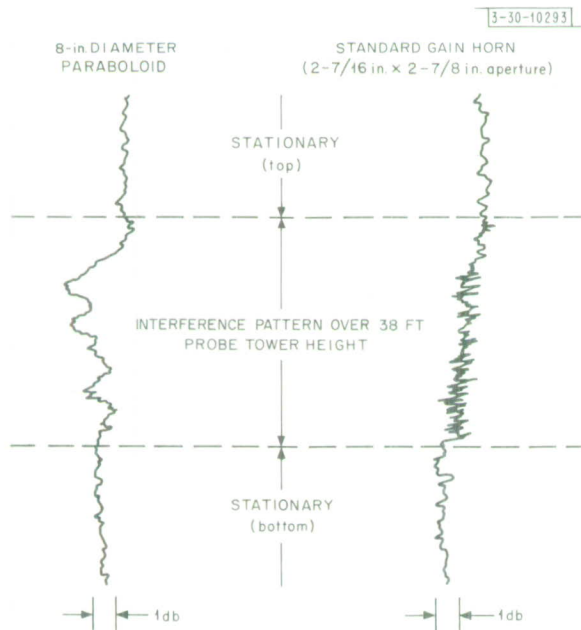


Fig. A-5. Comparison of interference patterns.

standard horn used in the gain measurements. The angular discrimination of the main antenna (3-db beamwidth $\approx 0.06^\circ$) is such as to almost completely discriminate against ground reflections. This is borne out experimentally by the excellent symmetry observed in vertical plane patterns even when the angle of declination is as great as 1° .

The distance separating the two sites is equivalent to $1.15 D^2/\lambda$, and consequently a slight amount of axial defocusing ($\approx 0.2\lambda$) is required in the main dish to simulate the far-field patterns.⁴

Early in the program the interference pattern at the receiving site was investigated with a probe tower 38-ft high and a standard-gain horn (nominally 25 db) traversing the length of this tower. Numerous runs were taken for incremental changes in the elevation angle of the transmitting antenna, and the envelope of the interference pattern was adjusted to illuminate properly the 28-ft main antenna. The final angular position of the transmitting antenna was such that the illumination of the 28-ft main antenna was slightly greater toward the top (the receiving aperture is located on the lower side of the transmitted beam). The amplitude taper is approximately 1/2 db, which has a negligible effect on the pattern measurements. The gain standard is positioned at the midpoint of the vertical aperture so that the taper will not result in an error in the gain measurement.

Since one of our main objectives is to evaluate the effect of changing environmental conditions on the antenna characteristics, the measurement errors caused by an imperfect range take on added importance. The effects of changing propagation conditions over the test site with changing environment must be separated from actual changes in antenna performance. For purposes of analysis, the properties of the range can be separated into three categories which can be related to specific errors in the antenna measurements. These are:

- (1) The interference pattern resulting from ground reflections.
- (2) Refractive effects (angle-of-arrival variations) caused by the changing refractive index with height relationship.
- (3) Signal scintillations associated with atmospheric turbulence, etc.

E. THE INTERFERENCE PATTERN

The measurement of gain by comparing the signal received from the antenna under test with that of a calibrated standard is based on the assumption that both antennas are placed in the same uniform field. Because of its high angular resolution, the main antenna receives only direct radiation from the transmitter (the free-space field). The signal received by the standard of comparison, however, because of ground reflections, depends on its directivity and its vertical position.

A comparison of the interference patterns seen by the standard horn and an 8-in.-diameter paraboloid is shown in Fig. A-5. The half-power beamwidth of the standard horn is approximately 8° as compared to a 3° half-power beamwidth obtained with the 8-in. dish. It is seen that the interference pattern of the 8-in. dish shows substantially larger angular separations between peaks and nulls and also much larger intensity variations.

It is well known that microwave propagation over rough terrain is characterized by poor specular reflection and results in a signal intensity near the free-space level.⁵ The integrated effect of a large number of reflected signals with a random phase relationship will alternately

Appendix A

reinforce and oppose the direct (free-space) field as the height is varied. It follows that the free-space level in relation to the interference pattern seen by the standard horn is the average of the loci of maxima and minima of the interference pattern. The free-space level in relation to the interference pattern seen by the 8-in. dish is doubtful, and, even if it were known, the error in gain measurement would be 2 db or more depending on the vertical position of the antenna. The point of the discussion here is that it does not necessarily follow that the error in the gain measurement due to ground reflections is decreased by increasing the directivity of the standard. In fact, unless the gain standard can be made directive enough to completely exclude ground reflections, the best approach is to employ a very broad-beamed standard. This would include a large area of diffuse reflections and, hence, approach the desired free space condition. The 25-db standard horn was used in all the gain measurements: The error in the gain measurements as a result of interference may be as much as ± 0.5 db, although it is probably only a fraction of this.

The interference pattern is surprisingly constant. Probe measurements taken intermittently over a period of three months in a variety of environmental conditions showed but negligible changes in the interference pattern.

F. REFRACTION

Although we were unable to measure changes in the angle of arrival of the incident signal or at least unable to separate this effect from the beam scan and boresight errors of the system, published accounts of angle-of-arrival measurements suggest that it may give rise to a significant error in the boresight measurements.

Sharpless⁶ describes angle-of-arrival measurements taken at a wavelength of 1.25 cm. The test range is a 12.6-mile overland path with an average height of 155 ft above ground level. The results indicate that the angle-of-arrival changes in the horizontal plane are slight, the maximum observed being 1.8 angular minutes. In the vertical plane, however, the variation is from -2.4 to $+6.6$ minutes relative to the line of sight.

The present test range is about half as long (≈ 6 miles) but otherwise similar to the one described. Using the reported results as a rough guide, we are led to conclude that anomalous propagation conditions might cause a number of minutes' variation in the RF angle of arrival. The reported 9-minute variation represents the maximum observed over a 2-month period. Also, the range used was on the New Jersey coast, much closer to the ocean than the present test site, which may result in quite different propagation conditions.

In any event, the beamwidth of the antenna under test is only 4.2 minutes; hence, 1 to 2 minutes of boresight error is serious. The possibility of errors this large or larger, as a result of refraction, cannot be overlooked.

Optical refraction affecting the boresight optics used in the evaluation program is the cause of still more uncertainty in the boresight measurements. Under "normal" conditions, optical and electrical refraction on passage through the atmosphere are approximately the same at these frequencies.⁷ Over a short horizontal transmission path, the relationship between the variation of optical and electrical refraction is unknown.

G. SIGNAL SCINTILLATION

Probe tower measurements taken with the 8-in. dish on a typical daily run are shown in Fig. A-6. The central section of these traces (marked descending) corresponds to the field variation over the height of the tower which is the superposition of the interference pattern and the signal scintillation. The regions marked top and bottom show the signal scintillation with the probe antenna held fixed at these positions. The amplitude of these scintillations varies from a negligible amount (before dawn) to approximately ± 0.6 db (early afternoon) with rates on the order of 1 Hz. Signal fluctuations of approximately the same rate and amplitude are observed on both the 28-ft main antenna and the broader-beamed standard-gain horn. This indicates that the scintillations are independent of ground reflections.

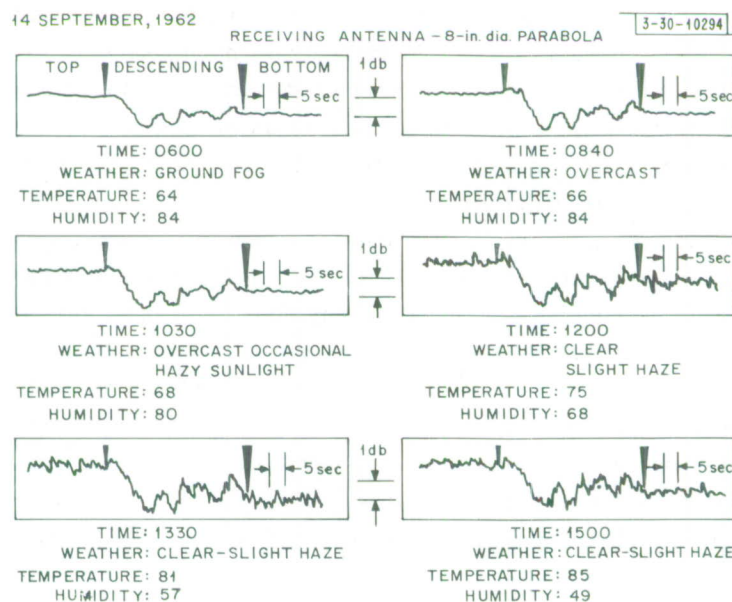


Fig. A-6. Probe tower measurements.

This effect has been reported elsewhere⁸ and is generally attributed to scattering due to atmospheric turbulence. Numerous runs of this type were taken, and it is apparent that the scintillations are negligible when fog is present and that they are generally much more severe in the daylight hours (especially early afternoon) than in the predawn hours.

The period of these fluctuations is comparable to the time required to manually swing the 28-ft antenna through the beam when taking a pattern. As a result, a slight lack of repeatability is noticed when patterns are taken at times of large signal scintillation. Measured side lobes can be in error by as much as 1 db and beamwidths by some 0.2 minute of arc.

These scintillations have a negligible effect on the gain measurement as the signal is effectively "averaged" out by rapid switching.

The errors in the antenna measurements which may be attributed to the range are summarized as follows:

Appendix A

1. Interference Pattern:— Because of the extreme angular discrimination of the antenna under test, pattern and boresight measurements are unaffected by ground reflections. The interference pattern seen by the relatively broad-beamed standard-gain horn can cause errors only in the gain measurement. The error will not exceed ± 0.5 db and is probably less.

2. Refraction:— Changes in the angle of arrival are of consequence only in the boresight measurements. The amount of error here is not known, although during periods of anomalous propagation conditions it may be large.

3. Signal Scintillations:— These intensity fluctuations affect only the pattern characteristics. At times of high scintillation (usually early afternoon) the measured beamwidths and side lobes may be in error by 0.2 minute and 1 db, respectively.

It may seem like an oversimplification to associate the interference pattern exclusively with the gain measurement, refraction exclusively with boresight measurements, and scintillations exclusively with pattern information, but the extreme directivity of the antenna and, to a lesser extent, measurement techniques indicate that this breakdown is quite accurate. In fact, this analysis of measurement errors caused by the test site appears to be generally applicable to the measurement of electrically large apertures.

These discrepancies in the range are not independent of each other; for example, conditions which might cause large refractive effects are certainly related to scintillation. However, the interdependence is of little significance when identifying each of the three propagation phenomena with a specific antenna characteristic.

Sharpless⁶ and Crawford and Jakes⁹ have reported multiple-path transmission caused by refraction rather than reflection. Two, three, and sometimes more signal components were found to arrive at differing angles in the vertical plane. If such an effect were present on our test site, it would cause serious errors in pattern, gain, and boresight measurements. Fortunately, no evidence of multiple-path transmission has ever been observed.

H. GAIN

The gain measurement is accomplished by the method of direct comparison with a calibrated gain standard. The standard used is a nominal 25-db Microwave Associates pyramidal horn.

The standard horn is mounted on one side of the main reflector and at the mid-point of the vertical aperture. The feed line to the standard is a long waveguide run (~26 ft) which is connected to one port of a waveguide switch mounted in the equipment cab just inside the vertex of the antenna. The main feed line consists of a waveguide run of approximately 15 ft and two calibrated attenuators. This line is attached to the second port of the waveguide switch. The function of the attenuators is to reduce the signal in the main line to the level of the signal in the standard horn. The common port of the switch is connected to the receiver and a level meter.

This arrangement enables rapid switching from the main antenna to the standard. Measurement errors as a result of the aforementioned scintillations are effectively averaged out.

I. LINE LOSSES

A most important part of the gain measurement is the accurate determination of the losses in the main and standard horn feed lines. It was attempted initially to use a reflex klystron as

a source for this measurement. However, a millimeter tube is subject to output power variations with physical handling, ambient temperatures, wind, etc. (The measurement must ultimately be performed outdoors.) This approach was found to be incapable of sufficient accuracy. A "Tucor" gas-discharge noise source was used as the signal generator. The noise source proved to be unaffected by the above disturbances.

The experimental setup for the loss measurement consists of the noise source and an isolator connected to the extreme end of the line to be measured (i.e., substituted for the standard horn or the main feed, as the case may be). The rear end of the line in question is attached to the receiver. The receiver output is directed through a precise IF attenuator to a level meter.

With the noise source on, the IF attenuator is adjusted to equate this level to that which is obtained with the noise source off. The expression is:

$$T_o + T_m = [T_s(1 - L) + T_o L + T_m] A \quad (A-1)$$

where

L = Fractional loss of the line length in question.

A = Fractional transmission of IF difference attenuation which is required to equate levels.

T_o = Ambient temperature of line being measured.

T_m = Effective receiver noise temperature.

T_s = Effective source noise temperature.

Solving for L ,

$$L = 1 - \left(\frac{1 - A}{A} \right) \frac{\left(\frac{T_m}{T_o} + 1 \right)}{\left(\frac{T_s}{T_o} - 1 \right)} \quad (A-2)$$

This can be shown to be

$$L = 1 - \left(\frac{1 - A}{A} \right) \left(\frac{1}{\frac{N_{on}}{N_{off}} - 1} \right) \quad (A-3)$$

The quantity N_{on}/N_{off} is determined by connecting the source directly to the receiver input terminals. It is then the ratio of the noise power output with the source on and off and can be read directly from the precision IF attenuator.

The result of these measurements shows the standard horn line loss to be 4.7 db and the main line loss to be 2.9 db. The main line loss includes insertion loss of the two calibrated RF attenuators and the waveguide of the pattern receiver. Repeated measurements check to within 0.1 db.

An alternate method was used to measure the relative attenuation of the two lines. Again, the noise source was connected successively in place of the standard horn and the feed. The

Appendix A

calibrated attenuator in the main feed line was adjusted to give equal levels of output from the receiver. The results of this method checked with those of the former to within ± 0.1 db.

The standard horn, as per the manufacturer's curves, has a gain of 25.05 db at 8.5 mm. The calculated value is 24.61, which should be accurate to ± 0.2 db (Ref. 10). Using the more conservative figure of 24.6 db for the standard horn, the measured gain of the main antenna is 67.3 db. This represents an efficiency of ≈ 53 percent.

Considering all the possible causes of error, namely, the interference pattern seen by the horn, line losses, calibration of the RF attenuators, beam alignment, etc., the error could be 1 db or more. It is believed, however, that the above figure is accurate to within ± 0.5 db.

The gain figure of 67.3 db does not include the losses of the main feed line. This figure is the gain from the feed and is quoted as being an indication of the quality of the reflecting surface. Operationally, the main line losses can be reduced to 1.4 db (measured); hence, the true or operational gain of the antenna is 65.9 db.

Gain measurements were taken during the daily runs to evaluate environmental effects. The previously described extremes of wind, temperature, etc., were encountered. The variation in measured gain was within ± 0.25 db for 90 percent of all the readings taken. There was no recognizable trend in this variation which could be identified with time of day, solar heating, wind conditions, etc.

J. FEED

The feed developed for this antenna¹¹ is a "rear feed" type consisting of an open-ended circular waveguide operating in its dominant mode (TE_{11}) with a circular reflecting disk positioned approximately $3\frac{1}{2}$ wavelengths in front of the open guide. A small hemispherical radome serves to hold the reflecting disk in position and also provides weather protection. Figure A-7 shows the feed in a 4-ft paraboloid. This feed has proven highly satisfactory in that it

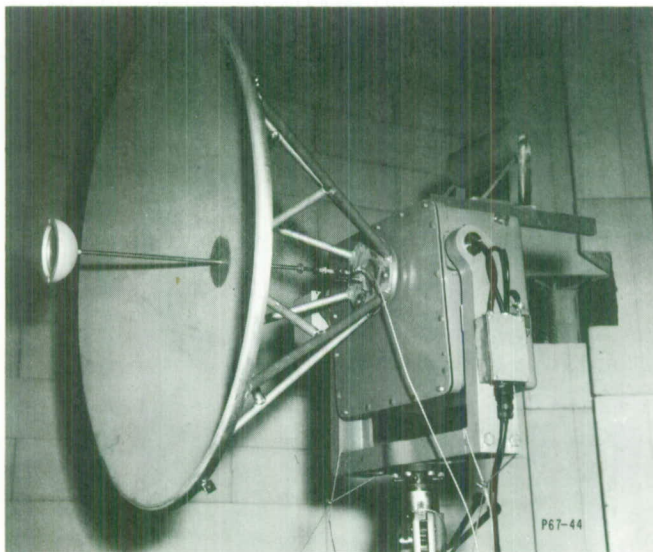


Fig. A-7. Modified Cassegrainian feed in 4-ft paraboloid.

provides dual polarization capability, wide bandwidths, and nearly equal beamwidths in the principal planes. However, it does have the small disadvantage of not offering a point center of phase and consequently there is a slight difference between the effective phase centers in the two principal planes.

A similar type of feed with the splash plate in close proximity to the open-ended guide is described in the literature.^{9,12} This feed behaves more like a ring source than a point source, and consequently it is considered not suitable for use with a reflector having a point focus.

The present feed differs from this "ring focus" feed in that the reflecting disk is well into the far field of the open-ended waveguide. The result is a configuration which is Cassegrainian in behavior, with the hyperboloid subreflector having degenerated into a flat plane. The image of the open-ended guide is placed at the focal point of the paraboloid.

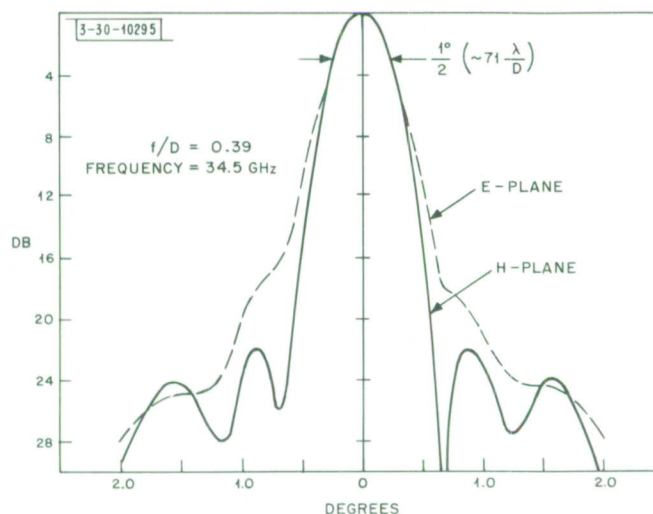


Fig. A-8. Patterns of modified Cassegrainian feed in 4-ft paraboloid, H-plane focused.

The phase error with this arrangement is reduced to within tolerable limits. Figure A-8 indicates the principal plane patterns taken in a 4-ft paraboloid with the axial setting of the feed such as to optimize the H-plane patterns. The difference between the effective phase centers in the two principal planes is approximately 0.3 wavelength. The compromise feed setting results in similar principal plane patterns with the side lobes clearly distinguishable from the main beam (i.e., the side lobes are not integrated into the main beam as in the E-plane pattern of Fig. A-8). This slight defocusing has no appreciable effect on gain or beamwidths.

A more detailed description of the feed can be found in Ref. 11.

K. PATTERNS

Typical azimuth and elevation plane patterns of the 28-ft antenna with the feed positioned to focus the elevation plane patterns are shown in Fig. A-9. There is a close similarity between these patterns and those taken in the proven 4-ft paraboloid. The amount of defocusing in the E-plane patterns of both sets is comparable. With the exception of the side-lobe structure in

Appendix A

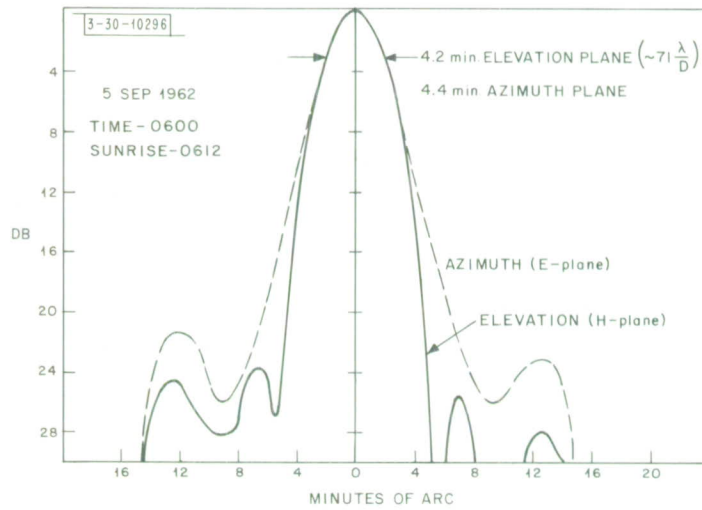


Fig. A-9. Typical azimuth and elevation patterns, elevation plane focused.

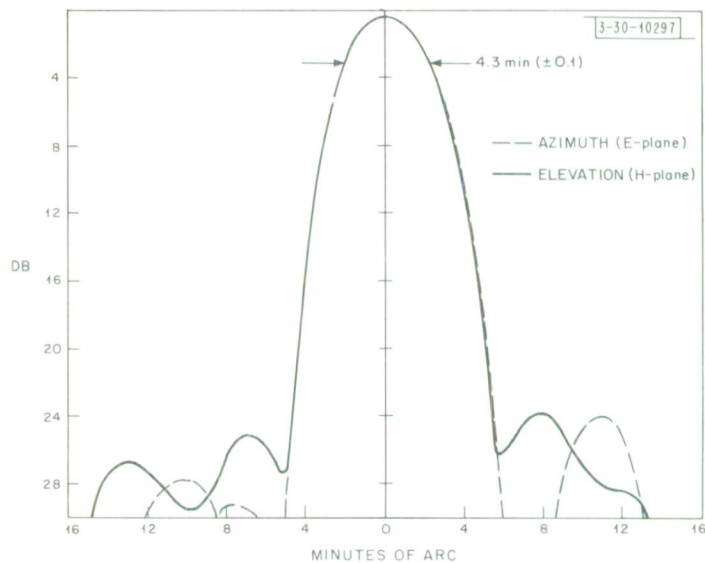


Fig. A-10. Azimuth and elevation plane patterns for 28-ft paraboloid with feed in compromise position.

the E-plane, the beamwidths and side lobes for both antennas check exceptionally well when expressed in terms of λ/D . This is a good indication of the excellent performance of the 28-ft antenna as well as the quality of the test site. In both cases, the difference in axial setting corresponding to the different focal points in the principal planes is approximately 0.3λ .

It is apparent that the inability to obtain perfectly focused patterns in both planes for a single axial setting of the feed is a characteristic of the feed itself and not the result of a distorted reflecting surface.

Figure A-10 shows azimuth and elevation plane patterns with the feed in the compromise position. The main beams of these patterns are almost identical; the only difference in the two is in the side-lobe structure. Patterns showing the far-out side-lobe structure are shown in Fig. A-11.

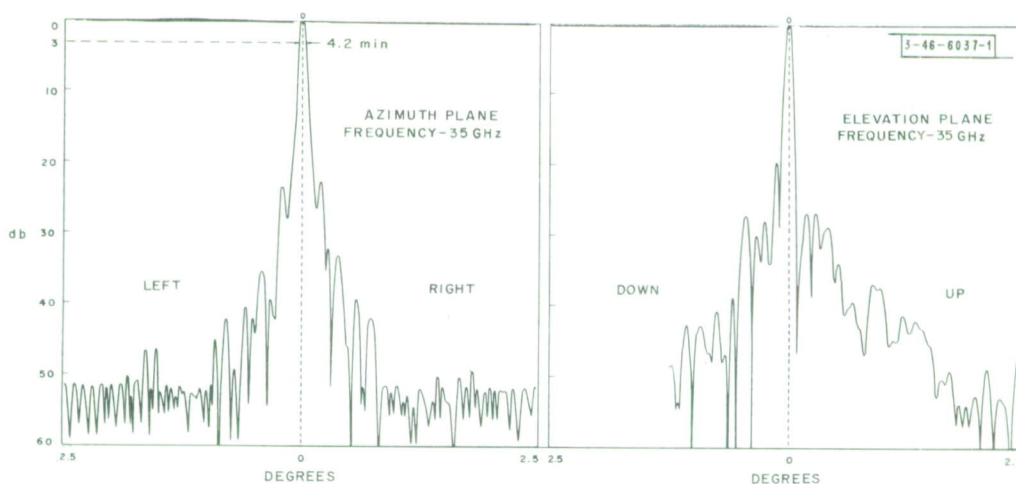


Fig. A-11. Azimuth and elevation plane patterns for 28-ft paraboloid showing far-out side lobes.

In the pattern measurements described below, which are primarily to determine the effects of solar heating, the axial position of the feed was set at the elevation plane focal point. This was done because the effects of solar heating are more pronounced in the elevation plane (the vertical temperature gradients are larger than the horizontal) and, hence, will be more easily distinguishable if the elevation plane is focused.

Thermocouples were attached to the aluminum backup structure to measure temperature gradients. The results indicate a maximum vertical temperature gradient (in the early afternoon) of approximately 30°F . The horizontal gradient is about half this figure. The antenna is directed almost due north to receive a signal from the transmitter and, consequently, the late summer sun swings across the back of the reflector.

Figure A-12 shows the effect of solar heating on the elevation plane pattern. The high asymmetrical side lobe varies from a level of $17\frac{1}{2}$ db to a condition of symmetry with both side lobes at 24 db. The $17\frac{1}{2}$ -db side lobe is the maximum experienced in all the patterns taken to evaluate the solar heating effect. On the particular day in question, the sun became obscured in the early afternoon and, as seen in the figure, the pattern reverted back to the predawn condition. A close correlation between asymmetry and solar heating was consistently observed.

Appendix A

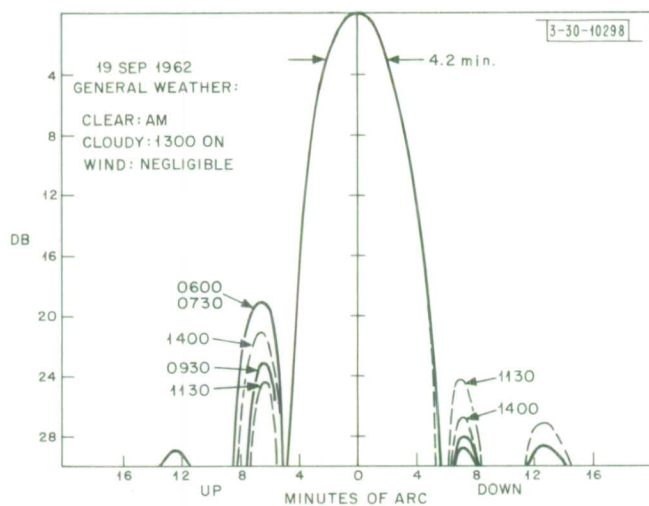
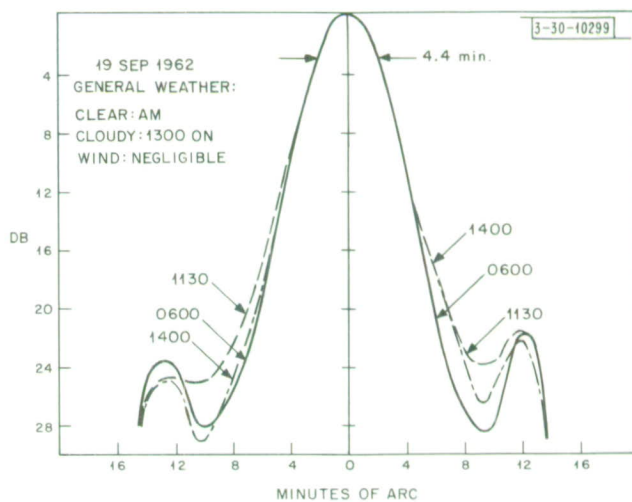


Fig. A-12. Elevation pattern (H-plane) for the 28-ft paraboloid showing effect of solar heating.

Fig. A-13. Azimuth pattern (E-plane) showing effect of solar heating.



The guy wires which support the feed column are attached to the ends of the aluminum girder panels. One result of the higher temperatures on the top of the backup structure is believed to be a relaxing of tension in the top guy wire. This causes a downward motion of the feed column and an upward scan of the beam. The high asymmetrical side lobe appears on the proper side of the scanned beam to be identified as the "coma" lobe associated with beam scan. As the beam is scanned off-axis, due to a lateral motion of the feed, the "coma" lobe appears on the axial side of the main beam. The side-lobe variation in Fig. A-12 shows the asymmetrical side lobe high in the predawn pattern and decreasing with solar heating. This "reversed scan" is the result of positioning the feed for best elevation plane focus at a time of maximum thermal gradients (afternoon). The up-and-down designations in the figure refer to the position of the transmitter relative to the peak of the elevation plane pattern.

A relaxing of tension in the top guy wire must certainly be accompanied by some thermal distortion of the upper portion of the reflecting surface which would also result in asymmetry. The obvious approach to determine how much pattern asymmetry is the result of motion of the feed column and how much is the result of reflector distortion would be to measure the beam shift. The pattern asymmetry which would result from reflector distortions would be accompanied by a negligible amount of beam scan. Unfortunately, the accuracy of the boresight shift measurements (described below) is not sufficient for the amount of beam scan involved. Pattern measurements, however, do indicate that the asymmetry due to distortion of the reflecting surface is negligible in comparison to the "coma" lobe.

Consider the case (Fig. A-12) where the predawn position of the beam is presumed to be downward and is scanned upward by the effects of solar heating to a condition of symmetry. In view of the excellent patterns obtained with the maximum temperature gradient (symmetrical; well-focused, etc.) associating the change in side-lobe structure with thermal distortion of the reflecting surface leads to the highly unlikely situation of the surface becoming more paraboloidal as the temperature gradient increases. Further, patterns were taken with the feed position adjusted such that the predawn position of the beam is on axis and is scanned upward with solar heating to an asymmetrical condition. Comparison of the predawn asymmetrical pattern (negligible temperature gradient) of the former with the early afternoon asymmetrical pattern (maximum temperature gradient) of the latter shows them to be mirror images. This is the case with patterns representing equal amounts of scan in opposite directions and can be true only if the asymmetry caused by thermal distortion of the reflector is negligible.

During the initial focusing period, it was found that a lateral displacement of the feed amounting to approximately $1/16$ in. changed the pattern from a condition of symmetry to a typical off-axis pattern with the "coma" lobe at the 17- to 18-db level. The $1/16$ -in. motion of the feed, which has about the same effect as the maximum temperature gradient, corresponds to a beam scan of approximately 1.4 angular minutes.

Figure A-13 shows the effect of solar heating on the azimuth patterns. It is seen that the asymmetry is slight. Presumably this is due to:

- (1) The thermal gradient from left to right ($15^\circ - 20^\circ\text{F}$) is on the order of half the top-to-bottom gradient.
- (2) The slight defocusing in the azimuth plane serves to mask asymmetrical effects caused by temperature gradients.

Appendix A

The only consequence, then, of nonuniform solar heating on the radiation patterns appears to be the beam scan in the vertical plane amounting to approximately 1.4 angular minutes. This amount of scan corresponds to the maximum asymmetry observed during the test period although on clear days the "coma" lobe consistently reaches the 17- to 18-db level. Thermal distortion of the reflecting surface seems to have a negligible effect on pattern asymmetry relative to the effects of beam scan.

L. AMBIENT TEMPERATURES

Measurements were taken in ambient temperatures which ranged from the mid 30's (°F) to the high 80's. No noticeable changes of the electrical characteristics were observed.

It might be mentioned here that the antenna was left unprotected on the roof of one of the Lincoln Laboratory buildings for the winter prior to the present series. Pattern and gain measurements taken before the winter are in close agreement with the present results.

M. WIND

Measurements were taken during periods when the wind velocity reached 25 mph with gusts of approximately 30 mph. The wind direction varied from the front to the back of the dish. No first-order effects were observed in gain or pattern measurements. The only noticeable effect of the wind was a slight oscillation in the level of the received signal, indicating some vibration in the antenna or more probably in the feed column. This amounted to not more than 0.2 to 0.3 db superimposed on the "wind-free" pattern.

N. BORESIGHT MEASUREMENTS

The variation in the alignment of the boresight optics and the position of the RF beam as a function of solar heating and wind conditions proved to be most difficult to evaluate. The most significant contribution to this difficulty is believed to be refractive effects, with both electrical and optical angle-of-arrival being effected relative to each other in an unknown manner.

Seven consecutive daily runs were taken, during which time no adjustments were made on either the feed position or the synchros. The boresight measurements taken over this period, although not as accurate as might be desired, give some indication of the magnitude of both the electrical and optical refraction encountered.

A total of about 50 measurements were made during these seven daily runs. Each measurement consisted of optical line-of-sight and RF beam position on both azimuth and elevation synchro readouts. The range of variation of these quantities experienced during this measurement period is as follows:

Azimuth:

Optical	1/2 to 1 minute
Electrical	1 to 1-1/2 minute

Elevation:

Optical	3 to 3-1/2 minutes
Electrical	3 to 3-1/2 minutes

There is no clear relationship between the relative optical and electrical variations in either plane. Initially, the optical and electrical boresights were aligned parallel and at times during the measurement period they are separated by $\approx 1\text{-}1/2$ minutes in the azimuth plane and more than 2 minutes in the elevation plane. Possible errors in these measurements are: the synchro readout (as much as $1/2$ minute), human errors in optical alignment, and errors in aligning the RF beam. Hence, the azimuth-optical variation of $1/2$ to 1 minute is about as small an angle as the system is capable of measuring.

Clearly, there is more variation of both the optical and electrical boresights in the elevation plane. There is no reason to suspect that any of the above sources of error would be more pronounced in the elevation plane over the azimuth plane. The variation of the elevation plane quantities may simply be positional shifts of the entire mount because of flexible mount supports or lack of rigidity of the base. A second possibility is the presence of both optical and RF refraction. References 6 and 12 indicate that angle-of-arrival variations of a number of minutes might be expected. If we assume that the basic accuracy of the mount is adequate, the amount of optical refraction for the period in question would appear to be in the vicinity of 2 to 3 minutes. The RF refraction is at least the same, probably more. It is thought that an appreciable part of the variation in the elevation plane can be attributed to refraction, if it is not the prominent cause.

Another important characteristic to be evaluated is the effect of elevation angle on boresight and patterns. Changes in gravitational loading could give rise to beam scan and pattern distortion. Although actual measurements have not been made, there are indications that boresight and patterns are preserved with elevation angle. The reflector is fabricated while pointing at zenith, and hence, the horizontal position probably represents the "worst case" of gravitational loading. In that the recorded patterns were taken in the horizontal position and show no evidence of pattern distortion, it can be assumed that pattern distortion at the higher elevation angles is slight. The beam can be held to the optical reference to at least a beamwidth, probably better.

O. CONCLUSIONS

It is clear that the antenna performs quite satisfactorily at a wavelength of 8.5 mm. The exceptional aperture efficiency (≈ 53 percent) and patterns obtained indicate that the reflecting surface is paraboloidal to a high degree of accuracy and retains its shape in the environmental conditions encountered.

The only measured change in electrical characteristics resulting from the wind, nonuniform solar heating and ambient temperatures experienced is a lateral motion of the feed column with nonuniform heating, causing the beam to scan. The amount of scan is less than 1.5 angular minutes. There is no evidence of any significant distortions of the reflecting surface as a result of these environmental conditions.

It was shown that with proper precautions, the test range does not introduce appreciable errors into the gain and pattern measurements. The influence of refraction, however, is believed to appreciably affect the boresight measurements, although the amount which might be expected during various weather conditions is not clear.

While there is still some uncertainty in regard to performance at high angles, in addition to the uncertainty in the boresight characteristics, recent radiometric experiments involving optical tracking of celestial sources indicate that the optical control of the beam is quite satisfactory.

ACKNOWLEDGMENTS

We take this opportunity to express our appreciation to Mr. J. Freedman and Dr. J. W. Meyer who were not only instrumental in the initial conception of the project, but also gave continued interest and support to make this work possible.

REFERENCES

1. W. A. Cumming, "Radiation Measurements at Radio Frequencies: A Survey of Current Techniques," IRE Proc. 47, 705-735 (May 1959).
2. V. L. Lynn, E. A. Crocker, J. W. Meyer, "Performance Evaluation Techniques for a Large Aperture Millimeter System," Proceedings of the Symposium on Electromagnetic Windows, Ohio State University (June 1962).
3. J. W. Dawson, "28-Foot Liquid-Spun Radio Reflector for Millimeter Wavelengths," IRE Proc. Correspondence 50, 1541 (June 1962).
4. D. K. Cheng and S. T. Moseley, "On Axis Defocus Characteristics of the Paraboloidal Reflector," IRE Trans. PGAP, AP-3, 214 (Oct. 1955).
5. D. E. Kerr, Propagation of Short Radio Waves, Vol. 13, M.I.T. Radiation Laboratory Series (McGraw-Hill, New York, 1951).
6. W. M. Sharpless, "Measurement of the Angle of Arrival of Microwaves," IRE Proc. 34, 837-845 (November 1946).
7. G. R. Marner, R. M. Ringoen, "Atmospheric Refraction of 8.7-mm Radiation," IRE Convention Record 4, Part 1, 14-18 (March 1956).
8. W. L. Flock, R. C. Mackey and W. D. Hershberger, "Propagation at 36,000 mc in the Los Angeles Basin," IRE Trans. PGAP AP-8, 235-242 (May 1960).
9. A. B. Crawford and W. C. Jakes, "Selective Fading of Microwaves," Bell System Tech. J. 31, 68-90 (January 1952).
10. H. Jasik, Ed., Antenna Engineering Handbook (McGraw-Hill, New York, 1961).
11. K. J. Keeping, "A Wide Band Antenna, Having Axially Symmetrical Patterns, High-Gain and Low Sidelobes for all Polarizations," Report 46G-0008, Lincoln Laboratory, M.I.T. (November 1960).
12. S. Silver, Ed., Microwave Antenna Theory and Design, Vol. 12, M.I.T. Radiation Laboratory Series (McGraw-Hill, New York, 1951).

Note: A description of the mm-wave antenna was given at the 1962 NEREM and appears on pages 66-67 of the NEREM Proceedings.

APPENDIX B

EXTENSION OF BOUNDARY PERTURBATION THEORY

The classical application of boundary perturbation theory to the solution of electromagnetic scattering problems is limited to boundaries which are close to those few boundary shapes for which exact solutions are known. By continuing the general approach to boundary perturbation theory introduced by Mitzner,* it has been possible to write the first-order perturbation contribution to the scattered field in a particularly simple form [Eq. (B-1)] which is easily applied to any unperturbed boundary shape for which the surface field quantities can be computed. Thus it becomes possible to deal with problems which are amenable neither to physical optics methods alone nor to perturbation theory alone, by first using physical optics to obtain the field quantities at the surface of the large "bumps," and then regarding the small "bumps" as perturbations of the larger "bumps," completing the solution using perturbation theory.

The first-order contribution $\delta^1 \bar{E}$ to the field scattered by an arbitrary boundary between two arbitrary isotropic linear media has been derived as

$$\delta^1 \bar{E} \cdot \bar{p}' = \int \{ \Delta \bar{E} \cdot \bar{D}' - \Delta \bar{D} \cdot \bar{E}' - \Delta \bar{H} \cdot \bar{B}' + \Delta \bar{B} \cdot \bar{H}' \} h dS \quad . \quad (B-1)$$

Here $\Delta \bar{A}$ is the discontinuity in the unperturbed field \bar{A} across the unperturbed boundary, \bar{A}' is the field that would exist at the unperturbed boundary were an electric dipole source \bar{p}' to be placed at the point where $\delta^1 \bar{E}$ is to be evaluated, h is the height function of the perturbations and the integration is carried out over the unperturbed surface. The sign convention is that $\Delta \bar{A} = \bar{A}_a - \bar{A}_b$ where \bar{A}_a [\bar{A}_b] is the field in the region toward which perturbations are reckoned as positive [negative]. No ambiguity arises in the value to be taken by the primed fields, because, for example, $\Delta \bar{E}$ is a vector normal to the surface and the normal component of \bar{D}' is continuous at the surface. Thus only the continuous components of the primed fields are involved.

The precise conditions to be imposed on the form of the unperturbed surface and on h are unknown. One supposes that the unperturbed surface can be perturbed only in regions free of field singularities and that both h/λ and ∇h should be small compared to unity, where λ is the smaller electromagnetic wavelength of the two regions.

The Lincoln Calibration Sphere (LCS) program† provided an opportunity to apply Eq. (B-1) to compute the far-field backscattered by a perfectly reflecting body. In this case, since tangential \bar{E}' and normal \bar{B}' are zero at the surface, Eq. (B-1) reduces to

$$\delta^1 \bar{E} \cdot \bar{E}'_o = \frac{k^2 e^{ikz}}{4\pi\epsilon_o z} \int (\epsilon_o \bar{E} \cdot \bar{E}' + \mu_o \bar{H} \cdot \bar{H}') h dS \quad , \quad (B-2)$$

where the superfluous jump operators have been omitted and the dipole \bar{p}' has replaced by the equivalent plane wave \bar{E}'_o incident on the sphere. Thus \bar{E} , \bar{H} and \bar{E}' , \bar{H}' are the total fields at

* K. M. Mitzner, "Effect of Small Irregularities on Electromagnetic Scattering from an Interface of Arbitrary Shape," J. Math. Phys. 5, 1776-1786 (1964).

† R. T. Prosser, "The Lincoln Calibration Sphere," IEEE Proc. (Correspondence) 53, 1672 (1965).

Appendix B

the surface of the perfect sphere when it is illuminated by the plane waves $\bar{E}_0 \exp\{-ikz\}$ and $\bar{E}'_0 \exp\{-ikz\}$, respectively.

The LCS is a hollow aluminum sphere nominally 1 m^2 in cross-sectional area. Since it was machined on a vertical boring mill after assembly, its shape is essentially that of a body of revolution. Thus the height function h of the surface perturbations is independent of the azimuthal angle, and can be expanded as

$$h(\Theta) = a \sum_{n=2}^{\infty} h_n P_n(\cos \Theta) \quad , \quad (\text{B-3})$$

where a is the radius of the mean sphere and $P_n(\cos \Theta)$ is the Legendre polynomial of degree n .

No generality is lost by assuming that the natural axis of the "sphere" lies in the plane $y = 0$ and is inclined at an angle Θ to the z -axis. Then, by choosing \bar{E}_0 and \bar{E}'_0 each to be either in the \hat{x} or \hat{y} direction, the following dyadic form for the total backscattered field \bar{E} (to first order) can be derived

$$\bar{E} \approx \delta^0 \bar{E} + \delta^1 \bar{E} = (\hat{x} \alpha_{xx} \hat{x} + \hat{y} \alpha_{yy} \hat{y}) \cdot \delta^0 \bar{E} \quad , \quad (\text{B-4})$$

where

$$\left. \begin{matrix} \alpha_{xx} \\ \alpha_{yy} \end{matrix} \right\} = 1 - i2ka \sum_{n=2}^{\infty} h_n \{b_n P_n(\cos \Theta) \pm p_n \frac{(n-2)!}{(n+2)!} P_n^2(\cos \Theta)\} \quad , \quad (\text{B-5})$$

and $\delta^0 \bar{E}$ is the zeroth-order backscattered field. The coefficients b_n and p_n are given by certain integrals of combinations of field components over the surface of the sphere. The field components can be computed exactly using their Mie series solutions or can be approximated over the lit region of the sphere by using physical optics. The former method is then a direct application of boundary perturbation theory; the latter is an application of the dual approach in which the small "bumps" are regarded as perturbations of the larger "bump" which is the sphere itself.

A comparison of the two methods, for $ka = 30$, is illustrated in Fig. B-1, which is a plot of $|b_n|^2$ and $(n-2)!|p_n|^2/(n+2)!$. It can be seen that there is very good agreement for all $n \lesssim 1.5ka$, and the same is true when a phase comparison is made. That the agreement is destroyed at $n \approx 2ka$ is to be expected, because the phase variation of the field products in the integrand in Eq. (B-2) matches that of the spherical harmonic of degree $2ka$ only in the vicinity of the shadow boundary. Thus the maximum contribution to b_n and p_n , for n close to $2ka$, comes from a region of the sphere where physical optics is no longer valid, and a more detailed analysis based on the methods of Fock should be used.

The expressions for the b_n and p_n , valid for large ka and $n/2ka < 1 - \delta$, computed using physical optics to specify the zeroth-order fields and used for the dashed curves in Fig. B-1 are

$$b_n \approx i^{-n+1} h_n^{(2)}(2ka) / h_1^{(2)}(2ka) \quad , \quad n = 0, 1, 2, \dots$$

$$p_n \approx \frac{(n-1)(n+1)(n+2)}{(2n-1)(2n+1)(2n+3)} \{ (2n+3)b_{n-2} - 2(2n+1)b_n + (2n-1)b_{n+2} \} \quad ,$$

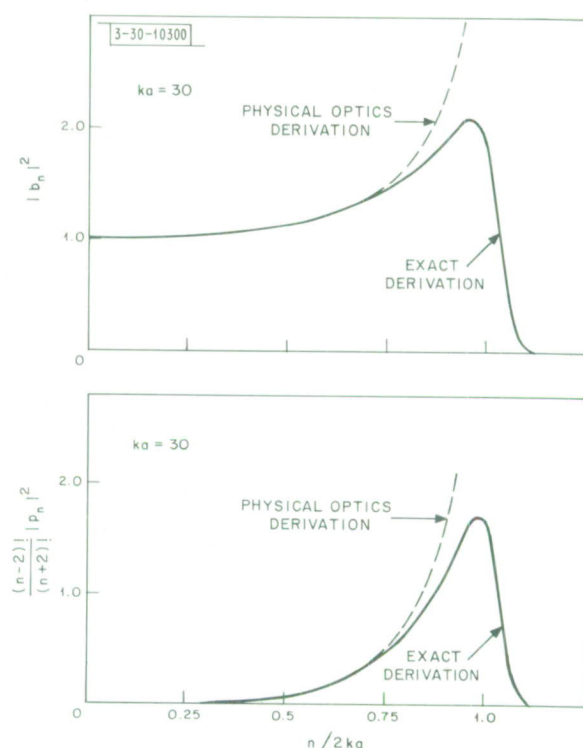


Fig. B-1. The b_n and p_n coefficients as a function of $n/2ka$.

where $h_n^{(2)}(y)$ is the spherical Hankel function of the second kind of order n . Simpler expressions, which also lose accuracy for very low values of n , are

$$b_n \approx (\cos \Theta_0)^{-1/2} \exp[i2ka(1 - \cos \Theta_0) - i(n + 1/2) \Theta_0]$$

$$p_n \approx -n^2 \sin^2 \Theta_0 b_n$$

where $\Theta_0 = \arcsin[(n + 1/2)/2ka]$.

The shape of the b_n and p_n curves shown in Fig. B-1 is roughly the same for all large ka except that the height of the maximum increases with increasing ka . A rough analysis indicates that the height of the peak is proportional to $(ka)^{1/3}$.

Careful profile measurements of one of the spheres produced during the LCS program were made and from them the h_n coefficients for the expansion in Eq. (B-3) were computed. Then, using Eqs. (B-4) and (B-5) the variation in the backscattering cross section was computed for the frequency of 9.4 GHz ($ka = 111$), at which a measurement of the sphere on a radar range was made. The results are shown in Fig. B-2, where the range measurement is compared with the cross section computed from both the exact and the approximate forms for the b_n and p_n . The 0-db level for the range measurement is set arbitrarily, because the sphere was better than any calibration target available. (The RMS surface deviation of this sphere was 3.2×10^{-3} in.)

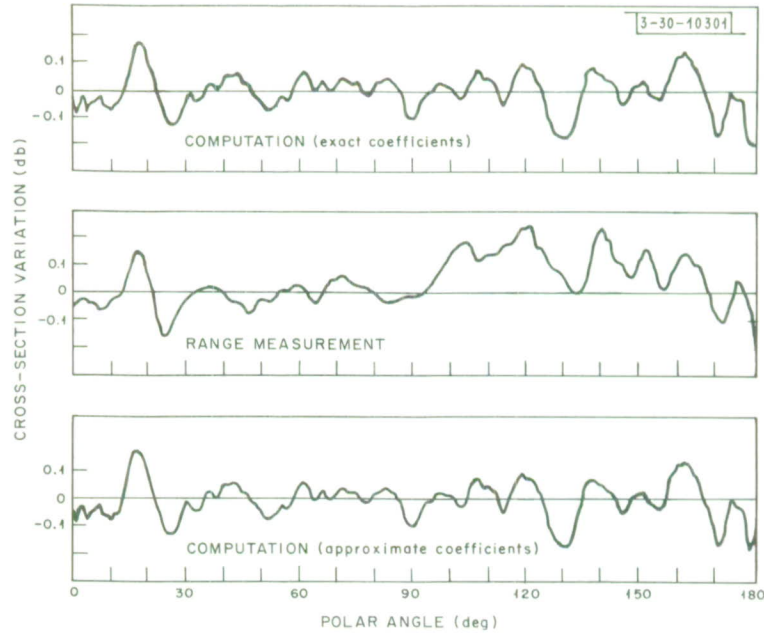


Fig. B-2. Comparison of measured cross-section variation with that computed using both approximate and exact b_n and p_n coefficients.

Fair agreement appears to exist between the measured and computed cross-section variation. The background level of the range varied between -30 to -40 dbm and so could account for discrepancies as large as ± 0.15 db. The two computed curves are practically indistinguishable from one another, owing to the fact that all the surface variation of the sphere was attributable to spherical harmonics of relatively low degree, for which the approximate b_n and p_n coefficients have good accuracy.

A further theoretical result of interest connects the variance of a particular vector component $\delta^1 E$ of $\delta^1 \bar{E}$ to the power spectral components w_n of statistically isotropic surface perturbations on a perfectly conducting sphere. Thus if

$$\langle h(\Theta, \varphi) h(\Theta', \varphi') \rangle = a^2 \sum_{n=2}^{\infty} w_n P_n(\cos \gamma) \quad ,$$

where $\langle \rangle$ denotes the expected value and $\cos \gamma = \cos \Theta \cos \Theta' + \sin \Theta \sin \Theta' \cos(\varphi - \varphi')$, then

$$\langle |\delta^1 E|^2 \rangle = |\delta^0 \bar{E}|^2 4k^2 a^2 \sum_{n=2}^{\infty} w_n g_n \quad ,$$

where g_n is $|b_n|^2 + (n-2)! |p_n|^2 / [2(n+2)!]$ and $(n-2)! |p_n|^2 / [2(n+2)!]$ for the like polarized and orthogonally polarized components, respectively, when the incident plane wave is linearly polarized. The corresponding values for g_n when the incident wave is circularly polarized are, respectively, $(n-2)! |p_n|^2 / (n-2)!$ and $|b_n|^2$. This explains the choice of the quantities plotted in Fig. B-1.

A related formula for the variance $\langle (\delta\sigma)^2 \rangle$ of the backscattering cross section is

$$\langle (\delta\sigma)^2 \rangle = \sigma_o^2 16k^2 a^2 \sum_n w_n f_n ,$$

where σ_o is the nominal (unperturbed) backscattering cross section and f_n is $|\text{Im}\{b_n\}|^2 + (n-2)! |\text{Im}\{p_n\}|^2 / [2(n+2)!]$ or $|\text{Im}\{b_n\}|^2$ depending on whether the measurement is made with linear or circular polarization, respectively.

M. L. Burrows

DOCUMENT CONTROL DATA - R&D		
(Security classification of title, body of abstract and indexing annotation must be entered when the overall report is classified)		
1. ORIGINATING ACTIVITY (Corporate author) Lincoln Laboratory, M.I.T.		2a. REPORT SECURITY CLASSIFICATION Unclassified
		2b. GROUP None
3. REPORT TITLE Radio Physics and Astronomy		
4. DESCRIPTIVE NOTES (Type of report and inclusive dates) Semiannual Technical Summary - 1 December 1965 through 31 May 1966		
5. AUTHOR(S) (Last name, first name, initial) Meeks, Marion L. and Pineo, Victor C. (Editors)		
6. REPORT DATE 15 October 1966	7a. TOTAL NO. OF PAGES 116	7b. NO. OF REFS 76
8a. CONTRACT OR GRANT NO. AF 19(628)-5167	9a. ORIGINATOR'S REPORT NUMBER(S) Radio Physics & Astronomy 1966:1	
b. PROJECT NO. 649L	9b. OTHER REPORT NO(S) (Any other numbers that may be assigned this report) ESD-TR-66-446	
c.		
d.		
10. AVAILABILITY/LIMITATION NOTICES Distribution of this document is unlimited.		
11. SUPPLEMENTARY NOTES None	12. SPONSORING MILITARY ACTIVITY Air Force Systems Command, USAF	
13. ABSTRACT This report covers research in the fields of radio physics and astronomy at Lincoln Laboratory for the period from 1 December 1965 through 31 May 1966. In a few cases, material from earlier work is introduced to clarify the discussion of a current program, e.g., "Experimental Evaluation of a 1000-Wavelength Antenna." Twenty-three papers presenting work by the Radio Physics, Communications, Solid State and Radar Divisions of Lincoln Laboratory and by the M.I.T. Research Laboratory of Electronics with the cooperation of Lincoln Laboratory are included. Twenty of the papers discuss work involving the Millstone Hill Field Station which is the Laboratory's primary facility for experimental research in radio physics and astronomy. Two papers describe the 28-ft millimeter research facility (1000 wavelength) at Lincoln Laboratory in Lexington and one is a theoretical paper on scattering from objects with irregular surfaces.		
14. KEY WORDS radio physics radar astronomy space surveillance techniques atmospheric research Millstone radar Haystack Hill ionospheric studies auroral observations		